Department of Applied Mechanics

Shear fatigue of adhesively bonded frictional interfaces in high-strength steel

---

Susanna Hurme

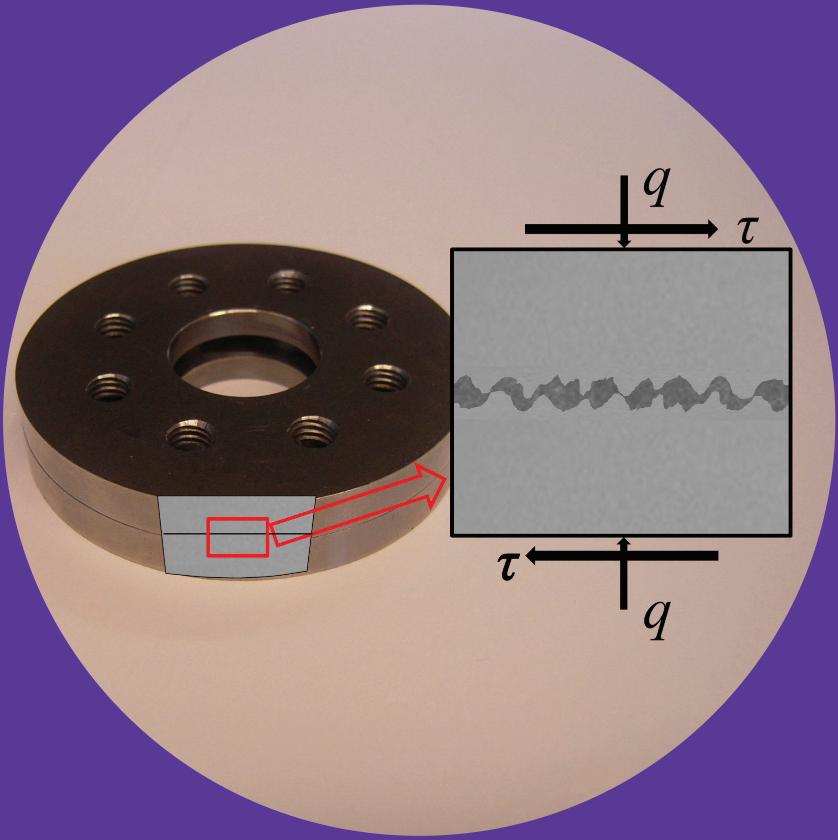

Aalto University

DOCTORAL
DISSERTATIONS

Aalto University publication series
DOCTORAL DISSERTATIONS 136/2014

Shear fatigue of adhesively bonded frictional interfaces in high-strength steel

Susanna Hurme

A doctoral dissertation completed for the degree of Doctor of Science (Technology) to be defended, with the permission of the Aalto University School of Engineering, at a public examination held at the lecture hall 216 of the school on 28 November 2014 at 12.

Aalto University
School of Engineering
Department of Applied Mechanics
Mechanics of Materials

Supervising professor
Prof. Gary Marquis

Preliminary examiners
Prof. Yukitaka Murakami, Kyushu University, Japan
Prof. Michael Vormwald, Technische Universität Darmstadt, Germany

Opponents
Prof. Yukitaka Murakami, Kyushu University, Japan
Prof. Alessandro Pirondi, University of Parma, Italy

Aalto University publication series
DOCTORAL DISSERTATIONS 136/2014

ISBN 978-952-60-5850-4
ISBN 978-952-60-5851-1 (pdf)
ISSN-L 1799-4934
ISSN 1799-4934 (printed)
ISSN 1799-4942 (pdf)
http://urn.fi/URN:ISBN:978-952-60-5851-1

Unigrafia Oy
Helsinki 2014

Finland

441 697
Printed matter

Author
Susanna Hurme

Name of the doctoral dissertation
Shear fatigue of adhesively bonded frictional interfaces in high-strength steel

Publisher School of Engineering

Unit Department of Applied Mechanics

Series Aalto University publication series DOCTORAL DISSERTATIONS 136/2014

Field of research Mechanics of Materials

Manuscript submitted 9 May 2014 **Date of the defence** 28 November 2014

Permission to publish granted (date) 7 August 2014 **Language** English

☒ **Monograph** ☐ **Article dissertation (summary + original articles)**

Abstract

This thesis presents new experimental data, physical observations and a new analytical model relevant for the design of bonded/bolted hybrid joints in high-strength steel plates subjected to cyclic shear loading. Hybrid joints can have improved fatigue endurance as compared to welded connections of similar geometries but, thus far, adequate research data has not been available. A procedure, linking the interface characterisation and the stress analysis of the full-scale joint, is presented in this thesis. The procedure can be readily adopted for product development involving the bonded/bolted hybrid joint. Further understanding of the physical processes of failure in the bonded and clamped interface is obtained by a scanning electron microscopy study of the adhesive layer at different stages of fatigue life.

Failure of the bonded/bolted joint occurs at the bonded interface where the total strength is a combination of cohesive and frictional forces. In this thesis, a new experimental method is introduced for characterising the idealised bonded and clamped interface under shear fatigue loading. The experimental method is based on the modified napkin ring specimen, which involves a bonded annular contact interface subjected to a well-defined and uniform stress state of constant normal stress and alternating shear stress. Experiments are used to identify the fatigue failure processes in the bonded and clamped interface under different clamping stresses, as well as the fatigue strength using a statistical method. Fatigue strength of the interface is then utilised to estimate the fatigue strength of a full-scale bonded/bolted double lap joint. The interface stress state in the full-scale joint is estimated using the finite element method using the cohesive zone model defined as contact definition at the interface. Parameters for the cohesive law are obtained from quasi-static fracture experiments on the modified napkin ring specimen.

The damage state in the adhesive is shown to consist of several microstructurally small cracks of different lengths and orientations. An exponential distribution which evolves with the number of fatigue cycles is suggested for describing the true damage state in the material. However, the evolution of damage, i.e., the growth, interaction and coalescence of the short cracks is a complicated phenomenon with insufficient theoretical understanding in the field of fracture mechanics. Therefore, a phenomenological fatigue damage evolution model is developed where damage is measured directly from the change in the compliance of the modified napkin ring specimen. The cohesive zone law is re-formulated to include fatigue damage. The model is necessary for a more accurate fatigue assessment of the hybrid bonded/bolted joint.

Keywords Adhesive bonding, Hybrid joining, Interface fracture, Fatigue testing, Cohesive zone modelling, Damage mechanics

ISBN (printed) 978-952-60-5850-4 **ISBN (pdf)** 978-952-60-5851-1

ISSN-L 1799-4934 **ISSN (printed)** 1799-4934 **ISSN (pdf)** 1799-4942

Location of publisher Helsinki **Location of printing** Helsinki **Year** 2014

Pages 129 **urn** http://urn.fi/URN:ISBN:978-952-60-5851-1

A! **Aalto-yliopisto**

Aalto-yliopisto, PL 11000, 00076 Aalto www.aalto.fi

Tiivistelmä

Tekijä Susanna Hurme	
Väitöskirjan nimi Leikkausväsyminen erikoislujien terästen liimatuissa kitkaliitoksissa	
Julkaisija Insinööritieteiden korkeakoulu	
Yksikkö Sovelletun mekaniikan laitos	
Sarja Aalto University publication series DOCTORAL DISSERTATIONS 136/2014	
Tutkimusala Lujuusoppi	
Käsikirjoituksen pvm 09.05.2014	**Väitöspäivä** 28.11.2014
Julkaisuluvan myöntämispäivä 07.08.2014	**Kieli** Englanti
☒ **Monografia**	☐ **Yhdistelmäväitöskirja (yhteenveto-osa + erillisartikkelit)**

Tiivistelmä

Väitöskirjatyö sisältää uutta tutkimustietoa erikoislujien terästen liimattujen ja pultattujen hybridiliitosten käyttäytymisestä syklisen leikkauskuormituksen alaisena. Liimatuilla ja pultatuilla liitoksilla voidaan mahdollisesti saavuttaa huomattavasti parempi väsymisenkesto, kuin hitsatuilla liitoksilla, mutta toistaiseksi niistä ei ole ollut saatavilla riittävästi tutkimustietoa. Tässä työssä esitellään menetelmä, jolla voidaan yhdistää idealisoidun rajapinnan kokeellisesti määritetyt mekaaniset ominaisuudet ja realistisen liitoksen jännitysanalyysi. Menetelmää voidaan suoraan hyödyntää hybridiliitosten tuotekehityksessä ja suunnittelussa. Lisäksi liimatun ja puristetun rajapinnan murtumista tarkastellaan kuvaamalla liimakerrosta elektronimikroskoopilla vaurion eri vaiheissa.

Liitoksen murtuminen tapahtuu liimatulla rajapinnalla, jonka lujuus määräytyy liiman koheesiovoimien ja pulttien aiheuttaman kitkavoiman yhteisvaikutuksesta. Työssä esitellään uusi koemenetelmä idealisoidun liimatun ja puristetun rajapinnan tutkimiseen väsytyskuormituksen alaisena. Koejärjestelyä käyttäen tunnistetaan liimatussa kitkarajapinnassa vallitsevat vauriomekanismit sekä määritellään tilastollisen menetelmän avulla kokeellisesti rajapintojen väsymislujuudet, joita käytetään liimalla ja pultilla liitetyn kaksoislimiliitoksen väsymislujuuden arvioinnissa. Liitoksen rajapinnan jännitysjakauma ratkaistaan elementtimenetelmällä. Rajapinnan murtumisen mallintamiseen käytetään koheesiomenetelmää, jonka parametrit määritetään idealisoidun rajapinnan koekappaleilla käyttäen staattista kuormitusta.

Liiman vaurion havaitaan koostuvan useista mikrorakenteellisesti lyhyistä säröistä, joilla on eri pituuksia ja orientaatioita. Säröjen pituuden ehdotetaan noudattavan eksponentiaalista jakaumaa, joka kehittyy väsytyskuormituksen mukana. Vaurion eteneminen on kuitenkin hyvin monimutkainen ilmiö, johon kuuluu lyhyiden säröjen kasvua, säröjen vuorovaikutusta toistensa kanssa sekä säröjen yhdentymistä. Nämä ovat ilmiöitä, joiden teoreettinen käsittely ei ole vielä täysin kehittynyt. Tästä syystä tässä työssä ehdotetaan lisäksi fenomenologista väsymisvauriomallia, jossa väsymisvaurio mitataan suoraan ideaalisen rajapinnan koekappaleen jäykkyyden muutoksesta. Rajapinnan staattisen murtuman mallintamiseen käytetty koheesiomalli muotoillaan uusiksi niin, että se sisältää väsymisvaurioparametrin vaikutuksen. Väsymisvauriomalli on tarpeellinen, kun halutaan arvioida tarkasti hybridiliitoksen väsymisen kestoa.

Avainsanat Liimaliitos, Hybridiliitos, Rajapintamurtuma, Väsymiskokeet, Koheesiomallinnus, Vauriomekaniikka

ISBN (painettu) 978-952-60-5850-4	**ISBN (pdf)** 978-952-60-5851-1	
ISSN-L 1799-4934	**ISSN (painettu)** 1799-4934	**ISSN (pdf)** 1799-4942
Julkaisupaikka Helsinki	**Painopaikka** Helsinki	**Vuosi** 2014
Sivumäärä 129	**urn** http://urn.fi/URN:ISBN:978-952-60-5851-1	

Preface

The research work reported in this dissertation was completed during the period of 2009-2014 at Aalto University under the guidance of Professor Gary Marquis. I am grateful to Professor Gary Marquis for instruction, supervision and his help in developing the scientific aspects of the research.

It has been an honor to have Professor Yukitaka Murakami from Kyushu University and Professor Michael Vormwald from Technische Universität Darmstadt as the preliminary examiners of this thesis. I would also like to express my gratitude to the anonymous reviewers of the international journals for their invaluable comments.

My colleague, Ahti Oinonen, is acknowledged for his help and advice throughout my doctoral studies. Special thanks are due to the staff of our laboratory: Kari Kantola, Seppo Meriläinen, Veijo Laukkanen and Olli Kamunen for their help and patience with the experimental work related to this thesis.

I am thankful to the staff of the Aalto University Department of Applied Mechanics for providing a pleasant and inspiring working environment. Many of you are not only co-workers but also dear friends. I would like to thank Professor Yukitaka Murakami from Kyushu University, the International Institute of Welding community, and Professor Grzegorz Glinka and his group at the University of Waterloo for the interesting discussions and new ideas.

The research work has been funded primarily by the Finnish Graduate School in Engineering Mechanics. Partial support was also provided by Aalto University, Ruukki Metals Oy and the Finnish Metals and Engineering Competence Cluster (FIMECC). Additional support and funding were provided by the Association of Finnish Steel and Metal Producers (Metallinjalostajien rahasto), Finnish Foundation for Technology Promotion (TES) and the Finnish Science Foundation for Economics and Technology (KAUTE). The financial support is gratefully acknowledged. CSC—IT Center for Science Ltd. is recognised for the allocation of computational resources.

I thank my husband Antti for his love and support, and for the numerous discussions we have had about my research. I would also like to thank my father, Mika, for our endless conversations on philosophy and science. My family and friends have all been extremely supportive in my efforts, for which I am grateful.

Espoo, 9 May 2014
Susanna Hurme

Contents

List of Abbreviations and Symbols

Symbols

A_1,A_2,A_3	τ vs. δ / δ^0 hysteresis loop fitting constants
a	Crack length
B	Fitting constant for the damage evolution equation
B_1, B_2	Fitting constants for the small crack growth equation under normal stress and shear stress, respectively
C	Integration constant
C_1, C_2	Constant of the exponential distribution of cracks in the adhesive
d	Tabulated value based on the staircase sequence, underlying distribution and analysis method
D	Scalar damage variable defining the decay of the cohesive zone model
D_o	Initial damage for estimating the fatigue life
D_c	Critical (fatigue) damage at which the applied shear stress equals the critical traction for quasi-static damage initiation
D_f	Fatigue damage parameter under mode II loading
$\hat{D}_f$	Estimated fatigue damage obtained by compressing several measured fatigue damage data points
ΔD_f	Interval of measured fatigue damage data points
$\Delta \hat{D}_f$	Spacing of the estimated data points
D_s	Quasi-static damage parameter under mode II loading
D_{tot}	Total damage including the quasi-static and fatigue damage
E	Modulus of elasticity
F	Load applied during the double lap joint test
$F(a)$	Distribution of cracks describing the fatigue damage

F_a	Load amplitude applied during the double lap joint experiment
$F_{a,f}$	Fatigue strength estimate of the double lap joints corresponding to no failure at $N = 2\text{x}10^6$ cycles, obtained experimentally using the small sample staircase method
G_c	Fracture energy defined as the area under the traction - separation curve
G_{c0}	Fracture energy at the initial state before fatigue damage
k	Fixed interval between successive measurements in the staircase analysis
LD50	Median value estimated by the staircase method
m	Exponent of the applied stress for the damage evolution equation
m_1, m_2	Exponent of the applied stress for the small crack growth equation under normal stress and shear stress, respectively
N	Number of fatigue cycles
ΔN	Number of cycles interval at which data was collected
N_f	Fatigue cycles to failure
n	Number of measured data points
n_x	Number of observations to be compressed into one estimate data point
$P_{\max}$	Maximum load during the double lap joint simulation
$P_{\min}$	Minimum load during the double lap joint simulation, maximum compressive load
q	Clamping stress, static normal pre-stress between the bonded interfaces
R	Load ratio
R_a	Surface roughness defined as average of the vertical deviations from the mean line
S	Measurement precision, defined as the standard deviation
$\hat{S}$	Estimated measurement precision
$S_{\bar{x}}$	Measurement precision improved due to data compression
t_0	Critical interface traction in the shear direction at the initial state before fatigue damage
t_c	Critical interface traction with fatigue damage
t_n, t_s, t_t	Components of interface traction in the normal, shear and transverse shear directions

$\overline{t}_n, \overline{t}_s, \overline{t}_t$	Components of interface traction according to the elastic response without damage
t_n^0, t_s^0, t_t^0	Components of critical interface traction in the normal, shear and transverse shear directions
X_0	Starting level of the staircase sequence
x	Measured data value
$\hat{x}$	Estimated data value obtained by compressing several values of x
α	Non-dimensional parameter defining the exponential damage evolution
γ	Fitting exponent for the damage evolution equation
Δ_{gap}	Displacement measured by the clip-on gauge during the double lap joint test
δ	Relative displacement in the modified napkin ring specimen or mode II separation of the cohesive zone model
$\Delta\delta$	Range of relative displacement between the interfaces
δ_a	Measured relative displacement amplitude in the modified napkin ring specimen
$\delta_{a,t}$	Total relative displacement amplitude
$\delta_{a,e}$	Elastic portion of the relative displacement amplitude
$\delta_{a,i}$	Inelastic portion of the relative displacement amplitude
δ_a^{th}	Threshold relative displacement amplitude at N=2×10^5 cycles below which the fatigue test was always a run-out
δ_m	Effective separation defined from the components of separation
$\delta_m^{\max}$	Maximum relative displacement at the contact point
δ_m^0	Critical effective separation at onset of damage
δ^0	Critical separation in the shear direction only
δ_m^f	Effective separation corresponding to full fracture
δ^f	Shear mode separation corresponding to full fracture
$\delta_n, \delta_s, \delta_t$	The components of separation in the normal, shear and transverse shear directions
ε	Measurement error

κ	Specimen stiffness in the mode II direction only
κ_0	Initial stiffness in the mode II direction
κ_{ij}	Components of the stiffness matrix in the elastic portion of the cohesive zone model
μ	Coefficient of friction
ν	Poisson’s ratio
Ξ	Energy dissipated due to damage
σ_a	Nominal stress amplitude
σ_2	Contact pressure in the local 2-direction calculated by the finite element method
τ	Shear stress
$\Delta\tau$	Range of shear stress
τ_a	Applied shear stress amplitude in the modified napkin ring specimen
τ_f	Shear fatigue strength corresponding to no failure at N = 2x10^6 cycles
τ_1	Contact shear stress in the local 1-direction calculated by the finite element method
τ_{II}^{p}	Measured interface mode II shear strength during quasi-static loading
τ_{II}^{res}	Remaining interface mode II shear strength during quasi-static loading measured after two million fatigue cycles

Abbreviations

CZM	Cohesive zone modelling
DCB	Double cantilever beam specimen
DLJ	Double lap joint
ENF	End-notched flexure specimen
FEM	Finite element method
HSS	High-strength steel
LEFM	Linear elastic fracture mechanics
MMB	Mixed-mode bending specimen

SEM	Scanning electron microscopy

List of Tables and Figures

Original features

This thesis presents new experimental data, physical observations and a new analytical model relevant for the design of bonded/bolted hybrid joints in high-strength steel plates subjected to cyclic shear loading. The research contained in the thesis was performed during the years 2009 – 2014, and most of the results were published in three journal articles and two conference proceedings. Significant aspects of the thesis, namely, the progressive fatigue damage model, the formulation of the cohesive zone model with fatigue damage and the related experiments (Sections 2.1.4 and 4.4) have not yet been published. The author was the main author of all of the afore-mentioned publications and responsible for the planning and oversight of all experimental work, the analysis of the test results, the numerical modelling and the development of the theory presented in the thesis. Professor Gary Marquis stimulated the original research ideas and contributed to the research with valuable comments and suggestions. The following features of the thesis are considered to be original:

1. The modified napkin ring specimen was introduced as a new experimental method to characterise the fatigue behaviour of the idealised bonded and clamped interface.
2. The fatigue failure modes of the bonded and clamped interface were identified as shear decohesion and fretting fatigue. The failure mode was found to depend on the clamping stress, so that shear decohesion occurred under low clamping stress and fretting fatigue under high clamping stress.
3. The non-linear response of the bonded and clamped interfaces due to small-scale slipping under high shear stress amplitudes was observed by using cyclic step tests. The hysteresis response was found to follow a power-law curve.
4. A statistical method was used to estimate the fatigue strength corresponding to no failure at $2x10^6$ cycles for the idealised interfaces under various clamping stresses, surface roughness and bonded or non-bonded conditions. The fatigue strength values can be used for fatigue design of more complicated hybrid joints assuming the interfaces are similar.
5. Experimental data from high-cycle fatigue tests with the double lap joint geometry were presented. The main findings were the analysis

of failure and an estimate of the fatigue strength using a statistical method.

6. The finite element method was used to estimate the stress state at the hybrid interface of the double lap joint. The interface was modelled using a combined cohesive and frictional contact model - a built-in feature of the commercial finite element software used. The parameters of the model were determined from quasi-static tests on the modified napkin ring specimen. The idea for this approach has previously been proposed, but the application in this work is different from that used in prior work.
7. After comparison of the stress state in the double lap joint and the fatigue strength results of idealised interfaces, a conservative estimate of the fatigue strength of the double lap joint could be found.
8. The fatigue strength determined from the double lap joints was compared to the fatigue strength of a welded connection with similar structural geometry, calculated based on International Institute of Welding fatigue testing guidelines. It was found that the bolted/bonded connection had 78.4 % greater fatigue strength than a comparable welded connection.
9. An in-depth understanding of the fatigue processes in the idealised bonded and clamped interface was obtained through scanning electron microscopy of the bondline under different stages of fatigue damage. It was suggested that the physical nature of damage could be described with an exponential distribution of microstructurally small cracks.
10. An equation for fatigue damage evolution was proposed. The distribution in the sizes of cracks was assumed to be exponential but characteristics of the exponential distribution change with the number of loading cycles. The degree of damage was considered to be directly observable from the specimen compliance. Parameters for the equation were fitted from experimental data. The damage model was found to estimate the experimentally-measured fatigue life of the modified napkin ring specimen with good accuracy.
11. The cohesive zone model, previously used to model the quasi-static fracture of the bonded and clamped interface, was re-formulated to include fatigue damage. The re-formulation was supported by interrupted fatigue tests on the modified napkin ring specimens, where the low-cycle fatigue test was halted after attainment of a certain degree of damage, after which the specimen was loaded quasi-statically up to failure.

1. Introduction

Industries are increasingly seeking ways to save raw material, to improve energy efficiency and to reduce CO_2 emissions. The development of light and efficient solutions provides the potential for the achievement of these goals over the service life of industrial equipment and machinery such as cars, trucks, other heavy-duty vehicles and lifting and transport equipment. The use of novel high-performance ultra-high-strength steels enables weight savings and the increased performance of structures. Finnish industries and universities embarked upon an extensive research initiative, the FIMECC Light and Efficient Solutions (LIGHT) programme, which involved studies in several fields related to the optimal application of ultra-high-strength steels. The research presented in this thesis forms part of the FIMECC LIGHT research programme related to the field of innovative design solutions.

The design of structures with the highest potential for weight savings and performance improvements through the use of high-strength steels (HSS) is frequently limited by the risk of fatigue failure. The durability of a high-strength steel structure subjected to predominantly cyclic loading depends greatly on the welded joints. As a general rule, the fatigue strength of a welded connection does not increase proportionally to the steel strength. Hybrid joints, wherein the good properties of adhesives and mechanical fasteners or spot welds are combined, provide potential joining alternatives for improved fatigue resistance in high-strength steel structures. However, an extensive literature review has shown that the available design data for hybrid joints are limited.

Research on hybrid joints, consisting of bolted joints reinforced with adhesive, has been on-going at Aalto University for several years (Oinonen and Marquis, 2011a, 2011b, 2013; Hurme et al., 2011; Hurme and Marquis, 2011, 2012, 2013, 2014). The goal of the research has been to improve the understanding of failure mechanisms in bonded and clamped interfaces under quasi-static and fatigue loading, and to create data relevant for design of bonded/bolted hybrid joints in HSS materials.

With the use of bonded/bolted hybrid joints, the load is carried by both adhesion and friction. The primary loading mode of the joint is cyclic shear stress combined with static normal stress. An in-depth understanding of the behaviour of the clamped and bonded interface during quasi-static as well as fatigue loading is needed, in order to fully exploit the potential of the hybrid joint, where two load-carrying mechanisms are combined to yield a joint stronger than either mechanism alone. In addition, a failure assessment method has been developed, as well as an appropriate test method.

1.1 Background

Hybrid joining can include weld-bonded, rivet-bonded, clinch-bonded or bolted-bonded joints. The combination of bolting and bonding is the least-studied method of hybrid joining with respect to joining metals. Most applications involve the use of adhesives and bolts in the fail-safe mode, where one method takes over when the other fails (Weitzenböck and McGeorge, 2011). The combination of adhesive and bolted joints is also common in repair applications (Hart-Smith, 1985; Chan and Vedhagiri, 2001).

Repair and fail-safe applications do not fully exploit the potential of hybrid joints. When the joint is initially designed as a hybrid joint, both components (bolts and adhesive) will ideally increase the performance of each other while compensating for the potential structural deficiencies of a single joining method. For example, when combining bolts or rivets with an adhesive, the joint can carry multi-axial stresses, while adhesive alone can carry only shear stresses. On the other hand, an adhesive will reduce the stress concentrations of bolt holes and thus improve fatigue resistance. A wide variety of mechanical and bonded joints is used in the automotive and aircraft industries, where light weight and structural integrity are primary design drivers. For thin sheet metal structures in high-strength steel, structural adhesives can effectively increase the maximum service load of friction-based, non-slip bolted connections.

The combination of adhesive joining and mechanical fastening has been studied in the field of aerospace applications (Hart-Smith, 1985; Mann et al., 1985), composite materials (Kelly, 2006; Fu and Mallick, 2001) and metallic joints (Moroni et al., 2010; Imanaka et al., 1995; Yamaguchi and Amano, 1985; Albrecht and Sahli, 1986; Albrecht, 1987). Improvement in the quasi-static strength has been observed (Oinonen and Marquis, 2011a, 2011b; Kelly, 2006; Fu and Mallick, 2001) when adhesive and mechanical fastening are combined, as compared to either mechanism alone. In addition, the fatigue endurance has been found to improve by the use of a combination of the two joining techniques (Imanaka et al., 1995; Kelly, 2006; Fu and Mallick, 2001, Mann et al., 1985; Albrecht and Sahli, 1986; Albrecht, 1987).

1.2 State of the art

There are a limited number of studies assessing the bonded and frictional interface under severe clamping stress, a characteristic condition for bolted/bonded joints. In particular, the case of fatigue loading has not been thoroughly studied. The following chapters provide a review into the assessment of bonded and clamped interfaces using experimental, analytical and numerical methods.

1.2.1 Experimental assessment and modelling of the bonded and clamped interface

Experimental methods for adhesive joints are an intuitive starting point when contemplating the experimental assessment of bonded and bolted joints. The most common specimen geometry for measuring shear properties of adhesives is the thin-lap shear specimen (ASTM D1002, 2010) (Fig. 1 a). However, the specimen is not well-suited for characterizing interfaces because of the stress concentrations and interactions of various stress components in the joint. Shear lag due to elastic deformations of the adherends causes stress concentrations at the ends of the overlap. Eccentricity in the lap joint causes bending, which introduces peel stresses at the ends of the overlap. The peel stresses can be reduced by using different double lap configurations such as the simple double lap joint (ASTM D 3528, 1996 (2008)) (Fig. 1 b) or the double lap strap joint (Fig. 1 c), which have minimal load eccentricity and thus minimal bending. Also, the thick adherend specimen (ASTM D 5656, 2010) (Fig. 1 d) has significantly reduced peel stresses compared to the thin-lap joint specimen. Test methods involving torsional loads, such as butt-bonded hollow cylinders (SFS-EN 14869-1:2011) (Fig. 1 e) or the napkin ring specimen (De Bruyne, 1962) (Fig. 1 f), provide a practically uniform stress state in the adhesive layer. However, the availability of testing equipment to perform torsion tests is not widespread in some laboratories. Fatigue testing is usually conducted using the single lap shear test (ASTM D3166, 1999 (2005); ISO 9664, 1993).

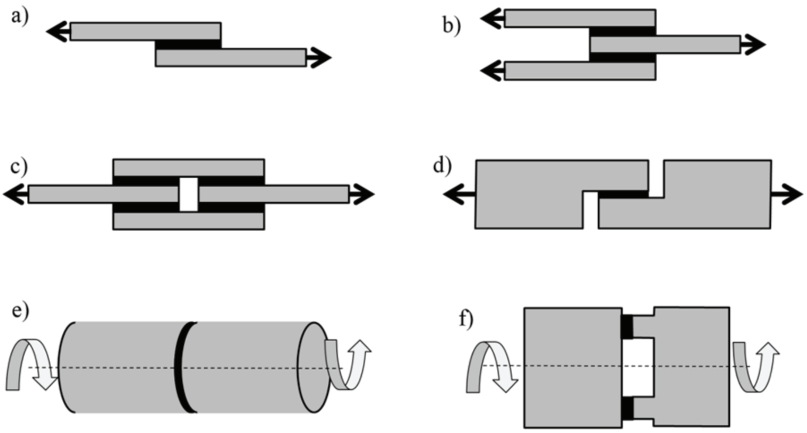

Figure 1. Common specimen geometries for testing of adhesive shear joints. a) The single lap joint, b) the double lap joint, c) the double lap strap joint, d) the thick adherend specimen, e) the butt-bonded hollow cylinder and f) the napkin ring specimen.

Stresses in the thin-lap shear specimen have been studied extensively since the introduction of the shear lag model by Volkersen (1938). A good state of the art review is provided by Kwakernaak et al. (2010). Analytical stress examinations of more complex geometries such as the double lap joint have also been published (De Bruyne, 1944; Tsai et al., 1998; Osnes and McGeorge, 2009). In addition to analytical studies, many researchers have applied the finite element method (FEM) for calculating the stresses in the adhesive joint (Gonçalves et al., 2002). The fundamental issue regarding finite element modelling of adhesive joints is the scale problem; the thickness of adherends is usually in the millimetre range, while the adhesive layer thickness measures only a few micrometres.

Commonly, the analytical and numerical approaches to adhesive joint design rely on the assumption that the adhesive layer has a constant thickness (Kwakernaak et al., 2010; Tong and Luo, 2011; Ashcroft and Mubashar, 2011). Similarly, most of the common adhesive test methods are designed so that a definite thickness of the adhesive is ensured (Kwakernaak et al., 2010). The established method for assembling a bonded/bolted hybrid joint is to first apply the adhesive to the adherend surface and then to clamp the adherends by tightening the bolts. The pressure applied by the bolts forces the uncured adhesive out of the interface, so that in practice, only a small quantity of the adhesive remains to fill the micro-volumes of the surface topography. Metal-to-metal contact can occur adjacent to these micro-volumes. Consequently, an adhesive layer with constant thickness is not a reasonable assumption for hybrid joints in steel with significant normal clamping stress. A schematic representation of the formation of the cohesive and frictional interface is shown in Fig. 2.

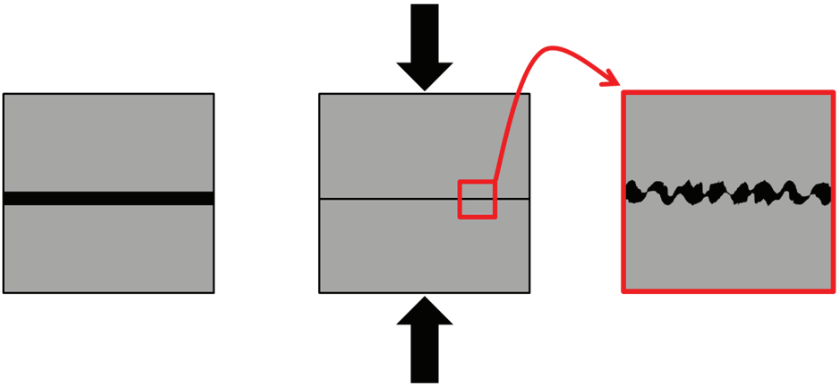

Figure 2. Schematic representation of the formation of the cohesive and frictional interface. Clamping is applied while the adhesive is in the uncured state. Most of the adhesive is squeezed out from the interface and as a result, some of the asperities of the metal surface are brought into contact, while the adhesive fills the micro-voids between the asperities.

In existing literature, the clamped and bonded interface has been assessed mainly with the use of anaerobic adhesives in cylindrical interference fit joints (Kawamura et al., 2003; Sawa et al., 2001; Yoneno et al., 1997, 1998) and threadlocking applications (Dragoni, 1999; Sekercioglu and Kovan, 2008). The static strength of the idealised bonded and clamped interface has been studied by using annular butt joints subjected to normal pressure and torsion (Dragoni & Mauri, 2000, 2002; Castagnetti and Dragoni, 2013) and by using the modified napkin ring specimen (Oinonen and Marquis, 2011a, 2011b).

The studies related to fatigue phenomena in the bonded and clamped interfaces are limited. Dragoni (2003) presented fatigue tests of bonded steel taper press fit joints. The results imply a fatigue limit of 50% of the static strength. In addition, fatigue tests on joints with the bonded and clamped interface have been reported by Croccolo et al. (2010) and Sekercioglu et al. (2005). Simple guidelines for estimating the strength and fatigue strength of clamped and bonded interfaces have been published (Dragoni and Mauri, 2011). However, the static analysis method is limited to average joint shear stress evaluation, with comparison to the strength of the hybrid interface. The fatigue strength, on the other hand, is simply evaluated by multiplying the adhesive shear strength by 0.5. Hurme et al. (2011) and Hurme and Marquis (2012, 2013) have published experimental studies using the modified napkin ring specimen revealing the failure modes of the clamped and bonded interface. The fatigue strength of the bonded and clamped interface was estimated using a statistical method. Recently, Hurme and Marquis (2014) reported experimental results on fatigue tests of a full-scale hybrid bonded/bolted joint, and applied the fatigue strength of the clamped and bonded interface in order to estimate the fatigue strength of the full-scale joint. It was concluded that a more accurate estimation of the fatigue life requires a progressive damage model for the adhesive. Such a model is suggested in this thesis.

Traditionally, the behaviour of the clamped and bonded interface has been understood through the superposition principle, involving the simple addition of the shear strength of the adhesive and the friction of the metal-metal contact. The superposition principle has been found to be valid for a strong adhesive under uniform stress conditions (Dragoni and Mauri, 2000; Oinonen and Marquis, 2011a, 2011b). However, Dragoni and Mauri (2002) observed that for flexible adhesives and non-uniform stress conditions, the superposition cannot be applied. As a result, it can be concluded that the superposition principle has no general application. A micromechanical model for the hybrid interface was developed by Dragoni and Mauri (2002), applied numerically (Castagnetti and Dragoni, 2012) and verified experimentally (Castagnetti and Dragoni, 2013). The model is based on the assumption that a thin layer of adhesive remains between the peaks of the asperities, in addition to the adhesive that fills the voids between the asperities, so that no metal-metal contact is actually present. Thus, the deviations from the superposition principle can be explained via this model.

Progressive failure in adhesively-bonded joints is often assessed by fracture mechanics or damage mechanics. The fracture mechanics approach relates the delamination growth, or de-bonding growth, to a fracture mechanics property such as the stress intensity factor. In most cases involving adhesive joints and composites delamination, the strain energy release rate approach introduced by Griffith (1921) is applied instead of using the stress intensity factor. Recently, the FEM-based cohesive zone modelling (CZM) technique has become widely used in failure modelling of adhesive joints (Castagnetti et al., 2011; De Moura et al., 2008). In the CZM approach, the interface between two layers is modelled using cohesive elements or contact definition, defined by the traction-separation relation. A damage parameter is employed to progressively reduce the stiffness of the cohesive element, thus simulating the growth of damage. The CZM has the advantage of being able to account for both the initiation and propagation of de-bonding, thus combining the advantages of strength-based and fracture mechanics-based approaches to failure analysis. The CZM has been combined with a friction model (Oinonen and Marquis, 2011a, 2011b) to assess the clamped and bonded interface. One advantage of the CZM is that the model parameters can be directly determined for the interface, eliminating the need to define a bond-layer thickness. Similar CZM-based modelling techniques for the bonded and frictional interface have been studied in the field of masonry (Alfano and Sacco, 2006) and damage models for adhesive and frictional interfaces have also been developed (Del Piero and Raous, 2010; Sacco and Lebon, 2012). The cohesive zone modelling technique is also adopted in this thesis and, consequently, is discussed in more detail in the following section.

1.2.2 Cohesive zone modelling

The cohesive zone modelling (CZM) technique is based on the pioneering work of Dugdale (1960) and Barenblatt (1962). Dugdale (1960) proposed a model assuming that there is a plastic zone ahead of the crack tip with stress equal to the material yield stress. Barenblatt (1962) proposed a similar model, but the stress was assumed to vary with deformation. The CZM was first applied in the finite element method by Hillerborg et al. (1976) to model crack growth in a concrete beam. Hillerborg et al. (1976) assumed that the crack propagates when stress at the crack tip reaches the yield stress, but when the crack opens, the stress does not fall to zero at once but decreases with increasing separation. During the crack opening, the material is in the micro-cracked state with ligaments still able to transfer stresses. Opening of the crack requires overcoming stress and, therefore, energy is absorbed during crack extension. The amount of energy can be obtained from the area under the opening curve. During the last decades, the CZM has been developed by numerous researchers and it has become a widely accepted tool for material fracture analysis (Tvergaard and Hutchinson, 1992; Chandra et al., 2002; Cornec et al., 2003).

Cohesive zones can be used to model fracture along a narrow strip zone by defining the material behaviour through a traction-separation law. With the requirement of a known fracture path, the delamination of composites and debonding of adhesive joints are natural applications of the CZM. Indeed, the CZM has become one of the most frequently used methods for modelling fracture of adhesive bonds (Castagnetti et al., 2011; De Moura et al., 2008) and delamination in composites (Turon at al., 2006). Several different constitutive models have been presented for the cohesive zone modelling of ductile and brittle fracture. The bi-linear model (Geubelle and Baylor, 1998) and trapezoidal model (Tvergaard and Hutchinson, 1992) are the most commonly used. In addition, some non-linear laws have been developed (Needleman, 1987; Allix et al., 1995; Xu and Needleman, 1993; Oinonen and Marquis, 2011a). Generally, the traction-separation law consists of a linear elastic region characterised by a cohesive stiffness, and a damage evolution region, triggered by attainment of the critical cohesive stress, following a linear or non-linear softening curve.

The initial region can also be non-linear, as in the model proposed by Cornec et al. (2003).

The cohesive zone model requires the definition of several parameters, the experimental evaluation of which is not always trivial. Cornec et al. (2003) have presented a well-defined procedure for determining the cohesive stress and energy for their cohesive law based on the J-integral. However, such procedures for metallic materials are not directly applicable to adhesive joints. Recently, Pascoe et al. (2013) raised the issue of the lack of fundamental understanding of the physics related to the definition of the cohesive zone model in composites delamination and adhesives de-bonding analyses. Cohesive stiffness is usually chosen based on numerical reasons. Critical traction is difficult to determine experimentally and, therefore, an assumed value is used (Khoramishad et al. 2010). Fracture energy can be determined experimentally; however, Khoramishad et al. (2010) chose to refine the value of the fracture energy obtained from experiments in an iterative manner so as to match the response of experiments on bonded joints. Another problem raised by Pascoe et al. (2013) was related to the definition of fracture energy. If it is assumed that the area under the traction-separation curve is equal to the fracture energy, this would imply that the work applied to the cohesive element is consumed entirely upon the formation of new fracture surfaces. However, in reality, at least some of the energy is dissipated by plastic deformation. The damage evolution model is described using numerous parameters, the physical nature of which are not completely understood.

The progressive failure of adhesive joints and composites is often studied experimentally by the double cantilever beam (DCB) specimen in mode I and the end-notched flexure specimen (ENF) in mode II (Dessureault and Spelt, 1997). For mixed-mode loading, the mixed-mode bending (MMB) specimen is commonly applied (Naghipour et al., 2011; Kenane and Benzeggagh, 1997). In many studies, the cohesive zone elements have been applied to model the damage process zone ahead of the crack tip, thus combining the fracture mechanics and damage mechanics approaches. The parameters of the cohesive zone model are determined by iterative methods, so that the model results correspond with the experimental results. The problem encountered with this method of determining the parameters is that the physical significance of the CZM parameters is not clear.

Published studies provide some experimental insights into the physical nature of damage in the material ahead of the crack tip. Chai (1993b) found that the mode II crack in the adhesive material in the ENF specimen propagates due to micro-cracks that form ahead of the crack tip. On the other hand, it has been found that the failure of the napkin ring specimen is a result of similar micro-cracking (Chai, 1993a). The stress state in the napkin ring specimen is nominally pure mode II (the stress intensity factors of the micro-cracks can be mixed-mode). Similar stress state occurs ahead of the crack tip in the ENF specimen. Thus, the damage process in the entire napkin ring specimen is equivalent to the damage process ahead of the mode II crack in the ENF specimen. Indeed, the napkin ring specimen provides an interesting opportunity to directly determine the constitutive equation for the cohesive zone model under mode II loading.

Oinonen and Marquis (2011a, 2011b) introduced the modified napkin ring specimen as an experimental method to directly determine properties of the cohesive zone model for clamped and bonded interfaces, thus providing an alternative to the numerical fitting of the various parameters. The work presented in this thesis provides further solutions to some of the shortcomings faced when defining cohesive zone models with fatigue: the parameters are defined using the modified napkin ring specimen, the physical nature of the fatigue damage is observed using the scanning electron microscope and a description of the physical nature of the damage, based on the exponential distribution of small cracks, is suggested.

Several studies have been published wherein cohesive zone models have been used to assess the fatigue crack growth. Some of the studies include a cycle-by-cycle assessment, which is mainly applicable to low-cycle fatigue (de-Andrés et al., 1999; Yang et al., 2001; Bouvard et al., 2009; Ural et al., 2009; Xu and Yuan, 2009; Cao and Vormwald, 2013; Roe and Siegmund, 2003;) while most of the studies related to composite delamination or adhesives debonding have adopted the cycle jump strategy proposed by Robinson et al. (2005), which is also capable of modelling high-cycle fatigue (Moroni and Pirondi, 2011; Khoramishad et al., 2010; Pirondi and Moroni, 2010; Turon et al., 2007; Harper and Hallett, 2010; Landry and LaPlante, 2012; Naghipour et al., 2011; May and Hallett, 2010, 2011; Muñoz et al., 2006). In many of the studies, a fatigue damage parameter is introduced into the CZM, and the strength or stiffness of the cohesive law is degraded as the damage parameter evolves with cyclic loading. An issue raised by Pascoe et al. (2013) is that one of the main advantages of the CZM, namely, the ability to model the crack initiation phase, is rarely used in published studies, as the CZM is mostly used to model fatigue crack growth. The onset of fatigue damage in the previous studies (Moroni and Pirondi, 2011; Turon et al., 2007; Harper and Hallett, 2010; Landry and LaPlante, 2012; Naghipour et al., 2011) usually requires the stress in the cohesive element to exceed the critical traction for static damage. This can occur at the crack tip but rarely in the un-cracked geometry. Consequently, in order to model fatigue crack initiation, the fatigue damage evolution and the resulting degradation of the cohesive stiffness and strength should occur with stresses lower than the critical traction. May and Hallett (2010, 2011) derived a fatigue law for cohesive elements, where the damage evolution is divided into static, fatigue initiation and fatigue propagation damage with different calibration procedures for the different stages of damage evolution. In this work, the fatigue damage evolution is observed from the experiments on the modified napkin ring specimens, which can directly provide the parameters of the cohesive law, thus clarifying the physical meaning of the several parameters. The initiation of a fatigue crack as a consequence of fatigue damage could potentially be modelled using the proposed approach.

1.2.3 Fretting fatigue in bolted joints

In addition to assessing the static and fatigue properties of the bonded and clamped interface, full-scale fatigue phenomena in the bonded/bolted joints should be discussed. The main limitation in the fatigue design of bolted joints, where the load is carried by interface friction, is fretting fatigue. Fretting damage occurs at interfaces which are in contact and which are subjected to clamping and cyclic tangential micro-slipping. High local stresses appear at the transition line where the clamping stress due to the bolt reduces to zero. The critical area experiences both sticking and slipping conditions during the loading and unloading. The condition of alternating slipping and sticking is called partial slip. The area under partial slip is susceptible to damage and crack initiation at the surface. Initially, the crack propagates through the volume affected by contact stresses and later, the propagation is driven by stresses in the bulk material. The crack propagation is governed by multi-axial stresses, variable R-ratio and non-proportional stresses, due to the non-linear nature of the frictional stress.

An extensive number of studies has been published about the fretting fatigue phenomenon, including experimental, analytical and numerical studies, some reviews of which are found, for example, in (Nowell et al., 2006; Ciavarella and Demelio, 2001; Nesládek et al., 2012). The fatigue in bolted joints has been studied by Benahmena et al. (2010), Chakherlou et al. (2013) and Wagle and Kato (2009), and it has been shown that the failure mechanism is determined by the clamping load. With low clamping, cracks initiate at the edge of a bolt hole, while intermediate clamping results in fretting wear. With high clamping, the failure type is fretting fatigue with crack initiation at the edge of the clamped contact area. Fatigue strength improves with increased clamping until fretting fatigue starts to dominate. Thereafter, no improvement in fatigue strength is obtained by increasing the clamping.

1.3 Applicability, requirements and limitations

The experimental and analysis results presented in this paper can be used as guidelines for product development, where the use of bonded/bolted hybrid joints in fatigue-critical applications is of interest. The results also increase the understanding of the behaviour of the clamped and bonded interface under fatigue loading. Improvements in understanding the physics related to cohesive zone modelling are provided through the novel experimental method, the modified napkin ring specimen applied here for fatigue assessment, and through scanning electron microscopy (SEM) observations of interface damage during fatigue loading. Experiments on the bonded/bolted double lap joint (DLJ) show that the hybrid joint indeed provides considerable potential for fatigue strength improvement, as compared to welded or simple bolted connections. The fatigue behaviour of bonded/bolted hybrid joints in high-strength steel has not previously been studied thoroughly and, as a result, not all necessary aspects of reliable design could be assessed in this work. The following limitations should be taken into account when contemplating the development of products which use bonded/bolted hybrid joints.

Adhesive materials are known to have load rate-dependent behaviour. However, all the quasi-static tests were performed using similar loading rates. The modified napkin ring fatigue tests were performed under two very different frequencies and, in both cases, the loading rate was different from the quasi-static tests. While the results showed no noticeable difference in the response due to the loading rate, the issue was not thoroughly examined.

Adhesives are sensitive to high temperatures, and one possible source of heat is the frictional motion in the interface during cyclic loading. There are frequency limitations related to the testing of adhesive joints, for example, the ASTM standard for adhesive fatigue testing recommends the frequency of 30 Hz (ASTM D 3166, 1999 (2005)). However, no such standardised recommendation is available for hybrid joints. The maximum loading rate was applied in the double lap joint tests which were conducted at 15 Hz. No noticeable heat generation was observed and it was considered that the effect of heat generation was negligible in the presented studies. However, the issue should be considered if higher loading rates need to be applied.

Another important factor in the use of adhesive materials is the effect of the environment. High temperature, humidity, ultra-violet radiation and exposure to certain chemicals can cause ageing in polymers, producing changes in colour, cracking, loss of mechanical properties and chemical disintegration. The testing of environmental effects is expensive, due to long exposure durations. However, the assessment of environmental effects is crucial, especially if the hybrid joint is intended for use in outdoor applications. In this study, fundamental aspects of the failure mechanism were studied and, thus, environmental effects were not assessed. The rate dependency, thermal properties and ageing of adhesives, along with many other critical aspects, have been reported in previous studies, and the reader is referred to any comprehensive handbook in the field, for example, that of da Silva et al. (2011).

All of the studies presented in this thesis have been performed on the same adhesive, which is a two-component structural epoxy DP 760 by 3M. The adhesive was originally selected because of its excellent temperature tolerance and high shear strength. Similar experimental investigations were performed on a different adhesive, as detailed in the Master's thesis by Sehra (Sehra, 2013). The adhesive in question was a toughened two-component epoxy adhesive DP 490 by 3M. Toughened adhesives should generally have improved fatigue endurance, as compared to brittle adhesives. However, the static and fatigue behaviour of the DP 760 was found to be better than that of the DP 490. It should be noted that a similar experimental approach to that presented in this thesis can be adopted, if the use of a different type of adhesive is of interest.

In addition to different aspects characteristic to adhesive materials, there are considerations related to the fatigue phenomena that are essential for comprehensive fatigue assessments. First of all, the effect of mean stress during cyclic loading is known to have a detrimental effect on the fatigue endurance of materials. In the case of adhesives, the effect is possibly even more pronounced due to the sensitivity of polymer materials to creep. All of the fatigue experiments in this study were performed under fully-reversed loading, i.e., no mean stress was present during the loading of the specimens. Therefore, a study of the mean stress effects should be among the first to follow the assessment presented.

Where fatigue is a design-limiting factor, many industrial applications are subjected to variable loading histories during their service time. Consequently, the fatigue analysis should be based on variable amplitude loading instead of constant amplitude loading. However, the variable amplitude loading was beyond the scope of this thesis and, all experiments were performed under constant amplitude loading. The proposed fatigue damage model can potentially be applied in variable amplitude loading assessments with suitable numerical implementation. However, the results should be confirmed by experiments.

The basis of the assessment presented is the assumption that loads are carried primarily by cyclic shear stress in the bonded and clamped interface. However, the lap joint geometries have some degree of cyclic tensile normal stress due to the shear lag effect. The modified napkin ring specimen, which provides the foundation for the assessments in this thesis, carries only cyclic shear mode loading superimposed with a well-defined static normal stress. Owing to the lack of information about the other loading modes, the analysis of the double lap joint was performed under the assumption that interfaces under tensile normal stress do not contribute to fatigue strength, which is clearly conservative. Therefore, the fatigue behaviour under different loading modes and mixed modes should be further studied. However, an initial assessment can be made by assuming that the entire load is transferred by shear stress, since shear stress is the dominant mode in the lap joint geometries.

A fatigue damage evolution model is presented in the paper. The model is well-justified by the SEM observations, and it is shown that the model can capture the low-cycle fatigue behaviour of the modified napkin ring specimen with good accuracy. However, due to time limitations, the model is not applied to the finite element method and to analysis of the double lap joint. Established methods for implementing fatigue damage in the finite element method can be found in the relevant literature (Robinson et al., 2005). For example, the implementation into Abaqus can be readily achieved through user-defined subroutines.

In summary, this thesis proposes methods for the fatigue assessment of hybrid bonded/bolted joints in high-strength steel materials which can be useful in the weight reduction and strength improvment of structures subjected to predominantly cyclic loads. Two approaches presented in this thesis can be adopted in product development and in the design of joints: the more simple method (based on interface shear stress and fatigue strength), is suitable for a failure/no-failure type of assessment in high-cycle fatigue, while the progressive damage method (based on cohesive zone modelling with fatigue damage evolution) is applicable under low-cycle fatigue. The method based on interface shear stress and fatigue strength requires the following:

1. The method can be applied to full-scale hybrid bonded/bolted joints where the primary load-carrying mechanism is cyclic shear stress combined with static normal stress from the bolts. The assessment provides a conservative estimate of the fatigue strength of the full-scale joints.
2. An experimental programme, using the modified napkin ring specimens manufactured from the adherend material and bonded with the desired adhesive, should be carried out, in order to determine an estimate for the fatigue strength characteristic of the interface. The fatigue strength should be estimated under different clamping stress conditions. A statistical approach, such as the small sample staircase method or the full staircase method, should be applied.
3. Parameters for mode II fracture of the cohesive zone model should be determined from quasi-static tests on the modified napkin ring specimen. The parameters should be calibrated from tests with different clamping stresses to ascertain that the model for the adhesive can provide the true response under the full range of clamping stresses present at the joint. In defining the model, friction should be added to the shear tractions in proportion to damage. The surface roughness should be the same as in the final joint in order to accurately describe the interface.
4. The finite element model of the full-scale joint should be constructed with a cohesive contact property defined between the adherends. Friction should be implemented in the cohesive contact region. Alternatively, cohesive elements could be used instead of contact definition. The critical traction under mode I loading should be assigned a small value, due to the assumption that joint areas under tensile normal stress do not contribute to fatigue strength.
5. The interface shear stresses should be solved from the finite element model and the stress state in the most critical location should be lower than the fatigue strength of the modified napkin ring specimen under similar clamping stress. The loading producing such a stress state is the conservative estimate of the fatigue strength.

The low-cycle fatigue method, based on progressive fatigue damage modelling, involves the following requirements.

1. Parameters of the cohesive zone model for mode II fracture should be determined from quasi-static tests on the modified napkin ring specimen, with different clamping stresses of the final joint, in order to accurately describe the interface.
2. Low-cycle fatigue tests should be performed using modified napkin ring specimens under low clamping stress. Fatigue damage evolution in the specimens would then be observed by a gradual increase in the specimen compliance. The damage evolution equation, relating the damage growth to shear stress and damage, should be determined by fitting to the data from the low-cycle fatigue tests.

3. Thereafter, damage evolution should be implemented in the finite element code by using methods established in existing literature (Robinson et al., 2005). The parameters of the cohesive zone model should be degraded with the fatigue damage according to the equations presented in the thesis.
4. The fatigue damage and quasi-static damage are described by two separate variables. Friction should be implemented in the cohesive zone model, following the principle that frictional traction increases in proportion to quasi-static damage. While quasi-static damage has not yet initiated, the friction model is not active during fatigue damage evolution.

2. Experimental methods

Firstly, the aim of the experimental study was to identify the failure mechanisms of the bonded and clamped interface and, secondly, to apply the obtained understanding to the analysis of a joint of engineering interest. The modified napkin ring specimen was developed from the napkin ring specimen first introduced by De Bruyne (1962) by adding a static clamping stress. The napkin ring specimen is well-suited for interface characterisation since the boundary conditions at the interface are well-defined and the loading stresses are uniform in the entire interface. The double lap joint geometry was chosen for the joint of engineering interest because it has only limited peel stress due to bending, and the loading can be considered to be mostly carried by shear stresses.

2.1 The modified napkin ring experiments

2.1.1 The specimen

Test specimens were machined from HSS sheets (Ruukki Optim 960QC, nominal yield strength 960 MPa) with a thickness of 6 mm. The main dimensions of the specimens are shown in Fig. 3. The eight smaller holes visible in Fig. 3 were used for fixing the specimens in the testing machine.

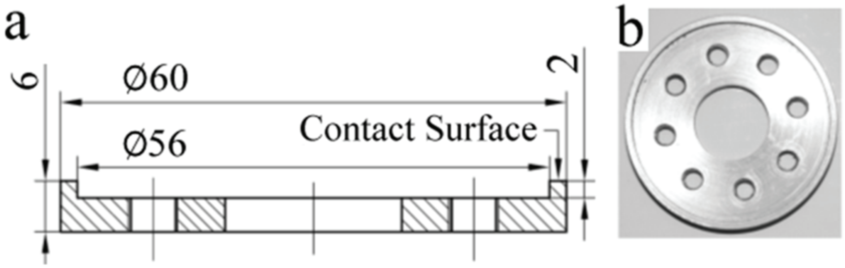

Figure 3. a) Test specimen with the main dimensions [mm]. Specimens were tested in pairs with only the 2 mm wide areas in contact. Structural adhesive was applied exclusively to the contact area. b) Photograph of the specimen.

The 2 mm-wide contact surface had one of the following surface finishes: grit-blasted with medium grit aluminium silicate (Ra = 3.1 µm), fine-ground (Ra = 0.4 µm) or coarse ground (Ra = 1.3 µm). During the course of the research, several batches of specimens were manufactured. The surface roughness was measured from 2-8 select samples from each batch and from four locations in one sample, with the measurement length of 0.8 mm. The direction of measurement was circumferential, i.e., along the direction of loading. The Taylor-Hobson Surtronic 3+ surface texture measuring device was used for the surface roughness measurements.

Before applying the adhesive, the specimens were cleansed of machining oils in an ultrasonic cleaner and wiped with a solvent. The machined surfaces inside of the $\phi = 56$ mm contact surface were protected using an O-ring seal, to prevent adhesion inside the contact areas and to eliminate the build-up of an inner spew fillet. A two-component structural epoxy adhesive, DP760, produced by 3M, was used for bonding the interfaces (3M United Kingdom PLC, 2009). Curing was performed at 65±3 °C for two hours. The gradual pre-heating time from 20 °C to 65 °C was 2½ hours.

Two specimen halves were glued together, with the circular contact surface of one specimen opposing the contact surface of an identical specimen. During the assembly process, adhesive was applied to the contact surfaces of the specimens and clamping to static pre-stress was immediately applied. The normal pre-stress was constant during the curing process and was not released until fatigue testing was complete. Four levels of static normal pre-stress, q, were applied in the experiments, $q \in \{4, 50, 100, 150\}$ MPa.

2.1.2 Laboratory test set-up

Experiments were performed using a servo-hydraulic test machine which applied cyclic torsion across the circular, glued interfaces. A schematic of the test device is shown in Fig. 4, with the key components indicated.

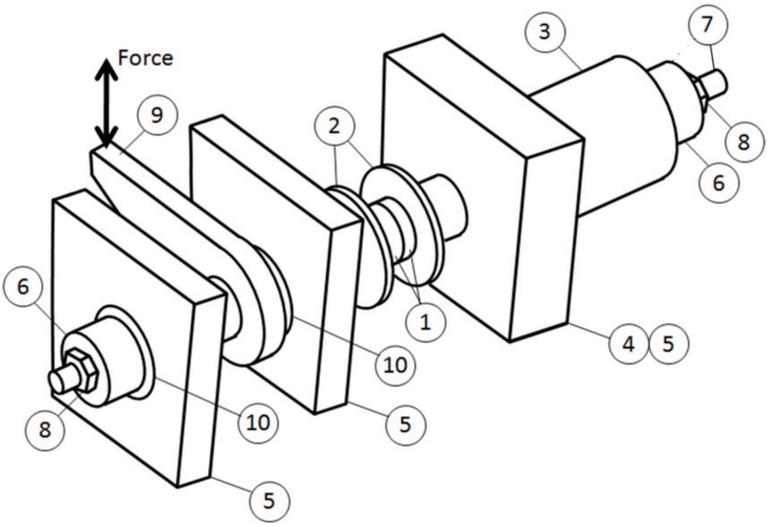

Figure 4. Schematic of the testing device. Key components are: 1-Specimen pair, 2-Specimen holder, 3-Axial load cell, 4-Torque reaction, 5-Support, 6-Thrust bearing, 7- Threaded rod, 8-Nut, 9-Torque arm and 10-Rotation bearing.

With respect to the napkin ring specimen, the applied static normal pre-stress, q, and alternating shear stress, τ_a, are illustrated in Fig. 5, along with a close-up schematic drawing of the bonded interface.

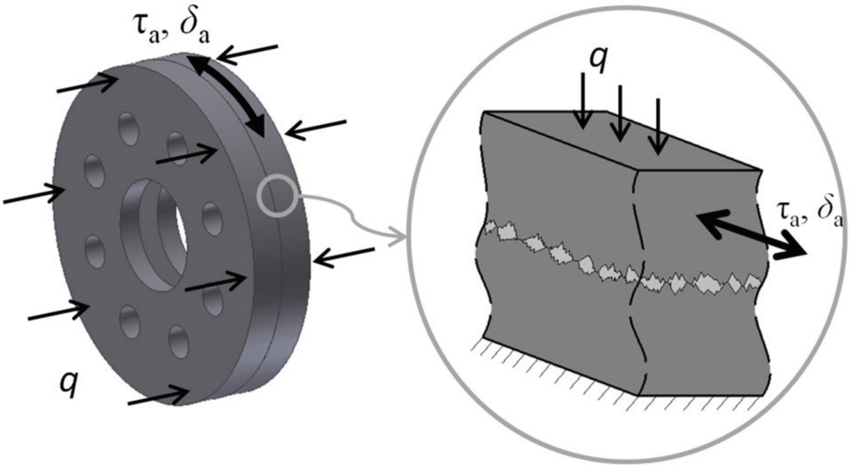

Figure 5. Loading of the napkin ring specimen during the constant amplitude fatigue test. The static normal pre-stress is denoted by q, δ_a is the relative displacement amplitude and the alternating shear stress amplitude is τ_a.

Normal stress on the interfaces was maintained via a fine-threaded rod equipped with an axial load cell. The normal stress was also continuously measured during testing, in order to verify that it varied by no more than 1 % from the initially-applied value. The threaded rod was equipped with low-friction axial ball bearings at each end. The influence of bearing friction due to pre-load on the measured torque was less than 1.5 %. As a result, the measured torque was assumed to be exclusively transmitted across the hybrid interface. Relative displacement (slippage) between the contact surfaces was measured by a high-precision eddy current extensometer (Kaman Precision Products Model KD-2306) fixed to each side of the specimen pairs.

At least one static failure test was conducted for each specimen condition in order to verify that the results were in line with those of Oinonen and Marquis (2011a and 2011b). The static tests were performed following the procedure described by Oinonen and Marquis (2011a and 2011b).

2.1.3 High-cycle fatigue experiments

Constant amplitude fatigue testing was performed using load (torque) control with a fully-reversed (R=-1) sinusoidal type signal at the frequency of 13.5 Hz. Normal pre-stress levels were 4 MPa, 50 MPa, 100 MPa and 150 MPa. The 4 MPa pre-stress was as close to zero as possible with the current test set-up. Tests continued until fatigue failure occurred, or until 2×10^6 load cycles had been attained. Failure was defined as large (δ_a > 500 μm) relative displacement (slipping) of the specimen pairs measured by the eddy current extensometer. During one constant amplitude fatigue test the stress amplitude could vary between τ_a ± 2 MPa due to limitations of the test system and control electronics. However, it was ascertained that there were no load peaks higher than 10% of the average load amplitude. For some of the specimens that did not fail within N = 2x10^6 cycles (run-out specimens), the constant amplitude fatigue test was followed by a static failure test. Complete tables of the high-cycle fatigue tests are provided in Appendix A.

2.1.4 Low-cycle fatigue experiments

The low-cycle fatigue tests were performed under constant amplitude, completely-reversed loading, with two clamping stress conditions (q = 4 and 50 MPa). The aim of the low-cycle fatigue tests was to obtain a better understanding of the fatigue damage process in the adhesive by improved control and more densely measured data points than in the high-cycle fatigue experiments. In order to improve the control of the test and to reliably measure the response cycle by cycle, the frequency had to be significantly reduced from the 13.5 Hz of the high-cycle fatigue tests. Consequently, the loading frequency was 1 Hz in the low-cycle fatigue experiments. However, two tests, one for each clamping stress condition, had the loading frequency of 0.2 Hz. No difference in the specimen response was observed between the 0.2 Hz and 1 Hz tests and, therefore, the 0.2 Hz tests could be included in the analysis.

Two types of tests were performed. Some of the tests continued until fatigue failure occurred. In addition, so-called interrupted fatigue tests were performed for both clamping stress conditions. The interrupted fatigue tests consisted of a cyclic loading part followed by a quasi-static fracture test. The fatigue test part was halted after a predefined relative displacement amplitude was measured by the eddy current sensor. Thereafter, the specimen was loaded until failure, following the quasi-static test procedure as explained in detail in Oinonen and Marquis (2011a and 2011b). The low-cycle fatigue experiments are summarised in Table 1 and the interrupted fatigue tests are shown in Table 2.

Table 1. Low-cycle fatigue tests up to full failure

Test ID	Clamping stress, q [MPa]	Shear stress amplitude, τ_a [MPa]	Frequency [Hz]
F1	4	28.7	0.2
F2	4	26.5	1.0
F3	4	27.2	1.0
F4	4	24.9	1.0
F5	50	24.6	0.2
F6	50	26.6	1.0

Table 2. Interrupted fatigue tests

Test ID	Clamping stress, q [MPa]	Shear stress amplitude, τ_a [MPa]	Relative displacement amplitude δ_a at interruption [μm]
I1	4	24.7	20.2
I2	4	25.3	27.5
I3*	4	25.5	30.3
I4**	4	25.0	20.9
I5**	4	25.0	25.3
I6	50	28.1	20.3
I7	50	25.1	18.5
I8	50	25.0	25.3

* Static fracture test was not in line with the other results and was excluded from the analysis
**Specimens were analysed with SEM instead of static fracture test

Scanning electron microscopy analysis of the damage

Scanning electron micrographs were taken from specimens I4 and I5 of Table 2. In addition, one specimen in the initial state (without cyclic loading) was studied by SEM. Micrographs of the bondline were taken from two locations in each specimen in the radial and tangential directions.

2.1.5 Cyclic step tests

Cyclic step tests were performed in order to quantify the irreversible small-scale slip between the interfaces for cycles with different shear stress amplitudes, and to further observe the interface behaviour under cyclic loading. Three fine-ground specimens were tested, one for each pre-stress level q = 50, 100 and 150 MPa. During the cyclic stress tests, several fully-reversed (R = -1) low-frequency cycles were applied to the interfaces, and about 500 load vs. relative displacement data points per cycle were collected. Initially, torque amplitude was approximately half of that used during the fatigue tests and the frequency was 0.67 Hz throughout the test. After four cycles, the torque amplitude was increased step-wise and the procedure was repeated until the specimen fractured.

2.2 Double lap joint tests

The experiments on the double lap joint consisted of a small sample staircase series for obtaining an estimate of the fatigue strength (Dixon and Mood, 1948; Dixon, 1965; Little, 1974). In addition, fatigue tests at short lives and quasi-static tests for both the bonded/bolted and plain bolted conditions were performed. In addition, three tests were performed with slightly modified test set-ups in order to clarify the failure mechanism (Hurme and Marquis, 2014).

2.2.1 The specimen

The specimen bore the double lap geometry as shown in Fig. 6. All parts of the specimen were cut from an 8-mm thick, high-strength steel plate (Ruukki Optim 960 QC, nominal yield strength 960 MPa). The assembly consisted of two main plates, and two cover plates attached with one high-strength M12 bolt and one M20 bolt and bonded with the two-component epoxy adhesive DP760 by 3M. The oversized M20 bolt was used to ensure a non-slip connection on one side of the specimen through higer clamping stress and larger clamped area. Failure was intended to occur as slipping of the interface under the smaller M12 bolt. The diameter of the hole for the M12 bolt measured 14.5 mm, which resulted in a clearance radius of 1.25 mm. The clearance ensured that the slipping of the hybrid interface did not lead to the load being carried by the bearing mode.

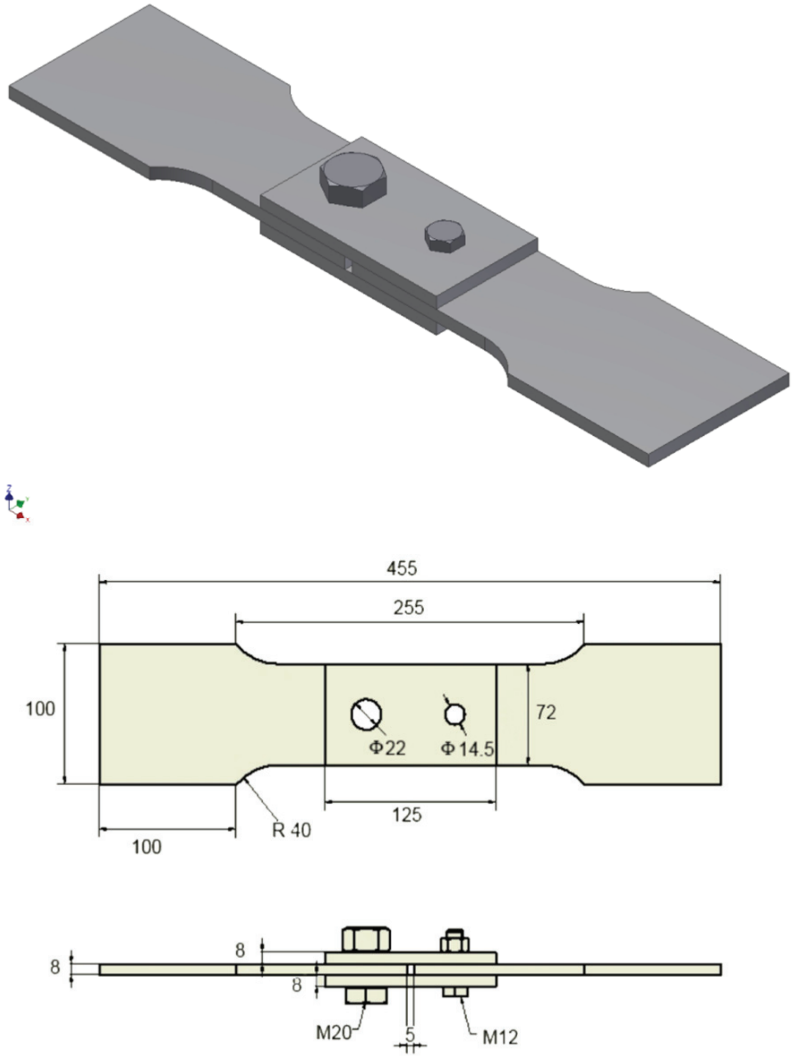

Figure 6. Geometry and dimensions in [mm] of the double lap joint. Bonding was applied to the interfaces between the cover plates and main plates. An oversized M20 bolt was used to ensure a non-slip connection on one side of the specimen thus restricting failure into the interface under the small bolt.

The contact surfaces of the plates were grit-blasted with aluminium oxide to an average surface roughness of R_a = 2.7 μm. Prior to bonding, the plates were cleansed in an ultrasonic bath and then rinsed with ethanol to ensure optimal bonding. The adhesive was applied to the grit blasted surfaces of the cover plates which were then immediately bolted to the main plates. As a result, the specimen had in total four separate bonded interfaces: two of them under the clamping from the small M12 bolt and two under the clamping from the oversized M 20 bolt. After assembly, the adhesive was cured in an oven at 65 °C for 2 hours. The specimen was allowed to cool down to room temperature before testing.

The M12 bolt was tightened to 130 Nm, which corresponds to an axial load of 43 +- 4.5 kN. The axial load was determined by measurements using a shim load cell. Eight bolts were selected for the calibration. The bolts were tightened using a torque wrench, and the axial load corresponding to each tightening torque was measured. The ratio of the applied tightening torque to the measured axial load is shown in Fig. 7, with a solid line at the mean and dashed lines at two standard deviations from the mean. The scatter in the resulting axial load was due to the method used for tightening the bolts. The accuracy of the axial load is affected by the torque wrench, geometric defects on the thread and bearing surfaces, and lubrication of the bearing surfaces. However, the accuracy of the bolt tightening using the torque wrench was considered to be adequate. Another possibility would have been to instrument each bolt with a strain gauge, but this was not deemed cost-effective, since the bolts underwent permanent distortion at specimen failure and could not be re-used. The large M20 bolt was tightened to 200 Nm.

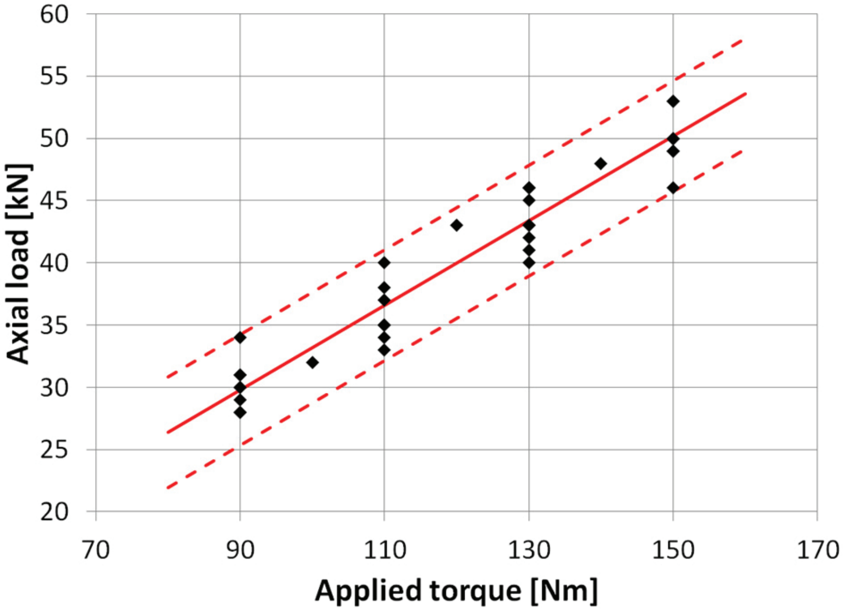

Figure 7. The ratio of the applied torque to the measured axial load for eight M12 bolts. The mean line and the lines at two standard deviations are shown for the data set.

2.2.2 Laboratory test procedure

The fatigue tests were conducted using an MTS Landmark 370.25 servohydraulic test system. The loading was applied in force control at load ratio R = -1 and at the frequency of 15 Hz. The constant amplitude fatigue test continued until $N = 2\text{x}10^6$ cycles had been attained, or until failure occurred at the bonded interfaces between the cover plates and the main plates. The failure was identified as a displacement of 1 mm measured by the built-in actuator displacement sensor and physically, it was the consequence of overall de-bonding of at least two of the bonded interfaces. Due to high loads and elastic strains in the main body of the specimen, the displacement amplitudes, measured during the test at the ends of the specimen, were as high as 0.5 mm. However, the gradual increase in the displacement due to progressive interface slipping was much smaller. In order to capture the slipping, the width of the 5-mm gap between the main plates was monitored by an MTS Model 632.02 clip-on gauge from one side of the specimen. A photograph of the test set-up is shown in Fig. 8.

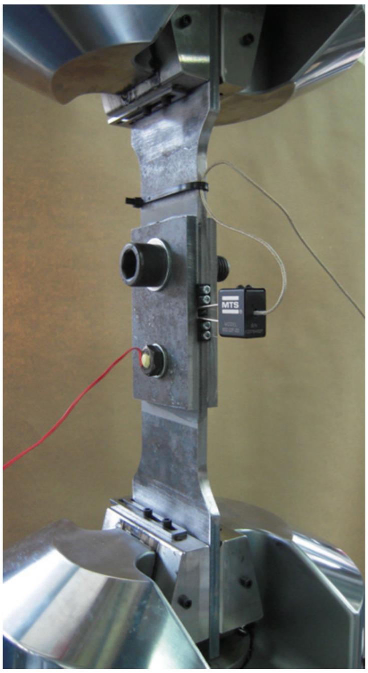

Figure 8. Photograph of the experimental setup for constant amplitude fatigue tests on the double lap joint.

First, quasi-static tests were conducted in order to estimate an initial loading level for the fatigue tests. Only one fatigue test on the plain bolted joint was performed. The comparison of the bonded/bolted and plain bolted joints was not considered to be meaningful because of the high difference in joint strength. The fatigue tests on bonded/bolted joints consisted of six tests for determining the fatigue strength at $2\text{x}10^6$ cycles, and a further three tests at high loading amplitudes to observe the mechanism of failure. The fatigue tests are shown in Table 3, containing the tests conducted for the small sample staircase series and additional fatigue tests with high load amplitude.

Modified double lap joint fatigue tests were also performed in order to obtain further understanding of the failure mechanism. In the modified tests, the washers under the large bolt were replaced by spherical thrust bearings measuring 20 mm in thickness and 55 mm in diameter. The bearings encompassed almost the entire contact surface affected by the large bolt, thus reducing stress concentrations due to clamping stress variation. In addition, the effect of different tightening loads for the small bolt was examined with the modified tests. The modified tests are listed in Table 4.

Table 3. Double lap joint fatigue tests.

Specimen ID	Load amplitude, F_a, [kN]	Failure (X) / Run-out (O)	Number of cycles to failure, N_f
NB 1 (non-bonded)	25	O	$>2x10^6$
Staircase series			
B 1	75	O	$>2x10^6$
B 2	80	O	$>2x10^6$
B 3	85	X	554440
B 4	80	X	808813
B 5	75	X	955340
B 6	70	O	$>2x10^6$
Additional fatigue tests			
B 7	90	X	26643
B 8	90	X	47361
B 9	95	X	34817

Table 4. Modified double lap joint fatigue tests.

Specimen ID	Load amplitude, [kN]	Bolt preload	Number of cycles to failure, N_f
M 1	90	43 kN	277730
M 2	75	10 kN	96532
M 3	90	55 kN	153323

3. Analysis methods

Fatigue experiments were analysed with different methods in order to obtain an in-depth understanding of the fracture behaviour of the hybrid joint, and to develop appropriate tools for design. Using the small sample staircase method developed by Dixon (1965) and applied to fatigue analysis by Little (1974), the fatigue strength corresponding to no failure at $N = 2\text{x}10^6$ cycles was estimated experimentally for the modified napkin ring specimens and the double lap joint specimens. The double lap joint was analysed by FEM, with a cohesive and frictional contact property defined at the contact interface. The parameters for the contact were determined from the quasi-static tests on the modified napkin ring specimen, some of which have been reported in Oinonen and Marquis (2011a and 2011b). The finite element method provided the stress state at the hybrid interface, which could be used for a simple failure/no failure assessment of the joint.

3.1 The small sample staircase method

The staircase method, also known as the “up-and-down method,” was originally developed by Dixon and Mood (1948) for estimating the sensitivity of explosives. The explosives were tested by dropping a weight onto them from different heights. It was assumed that there was a height, characteristic to the sample but not directly measureable, at which no explosion would result if the height was decreased and at which explosion would be produced if the height was increased. An estimation of the height could be obtained by a test series, whereby the height was either increased or decreased by a pre-defined interval, based on the response of the previous test. For example, if the previous test was conducted at a normalised height of 1.0 and the result was positive (i.e., an explosion occurred), the next test would be carried out at the normalised height of 0.8, assuming that the height interval was $k = 0.2$. If the test at the height of 0.8 did not result in an explosion, the height of the subsequent test would be increased by the interval $k = 0.2$, in this case, to the height of 1.0. The results can be plotted as in Table 5 for a fictitious test series. The interval k should be chosen to be close to the standard deviation, S, of the responses.

Table 5. Example of an up-and-down test series. The symbol X indicates an exploded specimen and the symbol O indicates a non-explosion.

Normalised height	Specimen number							
	1	2	3	4	5	6	7	8
1.2				X				X
1.0			O		X		O	
0.8		O				O		
0.6	O							

The up-and-down method has become the most popular method for determining mean fatigue strength corresponding to a specific number of cycles and is recommended, for example, by the current ISO standard for fatigue testing of metallic materials (BS ISO 12107:2003). Accoring to Collins (1993:384), the minimum number of specimens tested in the sequence should be 15. Hück (1983) provides useful hints for the practical use of the staircase method saying that the sample size of two already provides a rough estimate of the mean, but 5 to 9 samples would be better; with a sample size of 17, a meaningful standard deviation is obtained, and 25 samples provide very good results. For preliminary testing purposes, it is desirable to reduce the number of tests as a result of cost and time limitations. Indeed, it has been shown by Brownlee et al. (1953) that the up-and-down method of Dixon and Mood (1948) provides accurate estimates with as few as 5 to 10 tests. They also showed that the estimate is robust in terms of the interval, which could lie in the range of $2S/3 \le k \le 3S/2$. The method of Dixon and Mood (1948) was later modified by Dixon (1965), reducing the required number of tests down to a sequence with a nominal length of 2 to 6 specimens. The nominal length of the sequence is defined by excluding all but the last of the like responses in the beginning, for example, using this method, specimens 1 and 2 in Table 5 would be excluded. Little (1974) applied the small sample up-and-down method to the estimation of the median fatigue strength assuming extreme value response distributions. The estimate of the median dropping height, or fatigue strength, denoted by LD50, can be obtained from Eq. (1)

$$LD50 = X_0 + kd \tag{1}$$

where X_0 is the initial level of dropping height/loading and *d* is the tabulated value, based on the test sequence and the chosen analysis and underlying distribution. Dixon (1965) published tables of *d* for the sequences with nominal lengths of 2 to 6, based on numerical maximum likelihood analyses, $k / S = 1$ and underlying normal response distribution. Little (1974) published tables based on maximum likelihood and minimum chi square analyses and underlying extreme value (smallest) and extreme value (largest) response distributions.

Application of the staircase method requires initial knowledge of the standard deviation and shape of the distribution of the reponse. However, the data are rarely available, and it is generally accepted that the practicing researcher can make sufficiently accurate estimates (Brownlee at al. 1953). According to

Little (1974), in most cases, the approximations provided by different underlying distributions are identical for practical purposes. Thus, it is considered that the small sample staircase method provides an estimate of the mean fatigue strength that is accurate enough for preliminary tests and for the comparison of different specimen conditions, i.e., the purpose of this work. However, the staircase test with a small sample size provides no information on the standard deviation. Furthermore, the standard deviation provided by the full staircase method has been found to be incorrect (Hück, 1983). The staircase method has been modified by Hück (1983) in order to provide the correct standard deviation and optimum confidence limits. For design purposes, the statistical information including the standard deviation and confidence limits is essential and, therefore, the full staircase analysis recommended by standards or the modified method by Hück (1983) should be used.

3.1.1 The artificial staircase

Because some preliminary tests in the modified napkin ring test programme were not originally planned to be used with a staircase analysis, the artificial staircase method introduced by Nicholas (2006:105-106) was used where needed. In the artificial staircase method, a set of data obtained with equal stress intervals is pooled together and data points are drawn from the pool in a random fashion. This is commonly referred to as the bootstrap method. All data points must be used and no data point may be used more than once for creating an artificial staircase sequence. Additional data may be required. The mathematics for constructing an artificial staircase has not been fully developed, and there are no analyses proving that the results obtained by the artificial staircase are similar to those from a conventional staircase. However, Nicholas (2006) reported that the mean fatigue limit of a titanium alloy was found to be reproducible within 1 MPa, by constructing several artificial staircases from a pool of 20 data points. The consistency of the values implies that the artificial staircase constructed with the bootstrap method is a reliable alternative for a real staircase test.

The data points are treated in one of the following manners:

1. If a specimen failed at a given stress level at a given number of cycles, then that specimen is a failure at a higher number of cycles for the same stress level.
2. If a specimen failed at a given stress level, then that specimen is a failure at any higher stress level used in the staircase sequence.
3. If a specimen survived at a given stress level, then that specimen is a survivor at any lower stress level.

Similar procedures have been suggested by Hück (1983) to be used in the case where the chosen stress interval was initially too small or too large.

The modified napkin ring fatigue tests were conducted with approximately the interval of 5 MPa. However, the adjustment of the stress level in the house-built test set-up was not as accurate as desired and, occasionally, the average shear stress amplitude level of the test was lower or higher than intended. In such a case, the data are treated according to the afore-mentioned points 2 and 3. An example of the artificial staircase procedure is shown in Table 6 for the bonded, grit-blasted modified napkin ring specimen with the clamping stress *q* = 4 MPa.

Table 6. Example of the construction of an artificial staircase sequence for a grit-blasted, bonded modified napkin ring specimen with the clamping stress of 4 MPa.

Original data		Data treated according to points 2 and 3 (Nicholas, 2006)			Staircase sequence	
Shear stress amplitude, τ_a [MPa]	Number of cycles to failure, N_f	Shear stress amplitude, τ_a [MPa]	Failures, X	Run-outs, O	Shear stress amplitude, τ_a [MPa]	Response
27	1,000	30	1		30	X
24	70,000	25	2		25	X X
23	250,000				20	O
21	> $2\text{x}10^6$	20		1	Series	XOX
					d (Little, 1974)	First loading level, X_0
					-0.87	25 (MPa)
					LD50	20.65 (MPa)

In Table 6, the specimens with the shear stress amplitudes of 27, 24 and 23 MPa are failures and are thus considered equivalent to failures at 30, 25 and 25 MPa, respectively. On the other hand, the specimen with the shear stress amplitude of 21 was a run-out. If the specimen was a run-out at 21 MPa, it is assumed that it would also have been a run-out had the test been performed at 20 MPa. The data are rounded to the stress levels of 20, 25 and 30, and the interval of 5 MPa, because most of the napkin ring data was recorded with similar stress amplitudes and the same interval. The staircase sequence on the right side of Table 6 is the only sequence that can be constructed from the available data, since all of the data must be used. The nominal length of the sequence is 3. If several artificial staircase sequences were constructed, the *LD50* values of all sequences would be averaged so as to obtain the final estimation of the mean fatigue strength.

The small sample staircase method was used to estimate the mean fatigue strength at $N = 2\text{x}10^6$ cycles for the modified napkin ring specimens with four different clamping stresses, three different surface treatments and the bonded and non-bonded conditions, as well as for the double lap joint. The artificial staircases were constructed where needed.

3.2 Finite element analysis with cohesive and frictional contact definition

The double lap joint specimen (Chapter 2.2) was analysed using the finite element method. The commercial software, Abaqus, was used in this study. The adherends, bolt and washer were modelled as linear-elastic with the mechanical properties corresponding to steel (E = 210 GPa, ν = 0.3). The 8-node linear brick elements C3D8R with reduced integration were used for all parts (Abaqus User Manual, 2012). Only one quarter of the bonded slip area of the lap joint was modelled in order to reduce the calculation time. The geometry of the model is shown in Fig. 9. All translations are restrained at the back end of the top plate (area B in Fig. 9) and the cutting planes possess the symmetry boundary condition.

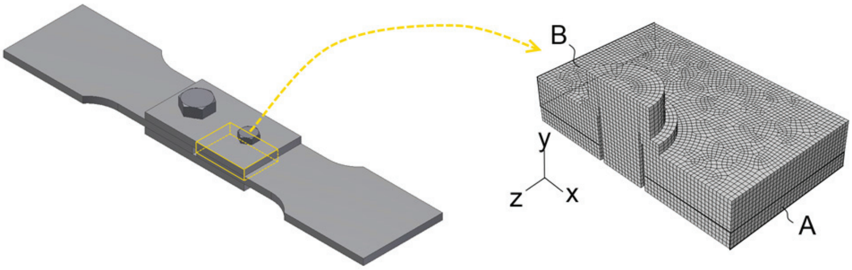

Figure 9. Finite element model of one quarter of the bonded slip area of the double lap joint.

The contact interaction at the interface between the two plates was defined as having combined cohesive and frictional behaviour. Other contacts in the model (between bolt, washer and adherend) were defined using the penalty friction model and the hard normal contact which allows for no penetration. The coefficient of friction outside of the bonded contact area was chosen to be $\mu = 0.2$, a typical coefficient for untreated steel-on-steel contact.

The analysis was performed in two steps. In the first step, the bolt load of 21500 N was applied at the bolt cross-sectional area. In the next step, the uniform pressure load of P_{max} was applied to face A in Fig. 9 following a smooth-step amplitude, while the bolt load remained constant. The unloading and loading to the maximum longitudinal compression of P_{min} was subsequently applied, following the smooth-step amplitude. The tractions at the cohesive interface were reported in the CSTRESS surface output variables.

3.2.1 Cohesive zone formulation for the bonded and frictional interface

The bonded interface was modelled with a traction-separation cohesive law combined with Coulomb friction. The idea of combining the cohesive law and Coulomb friction was already discussed by Oinonen and Marquis, (2011a, 2011b). They used cohesive elements with a damage evolution law especially formulated for the napkin ring specimen. However, the incorporation of friction requires that the cohesive stiffness in the positive normal direction be defined as zero. A small amount of positive normal stress is unavoidable in the double lap joint, thus the assumption of zero normal stiffness will lead to inaccuracy.

In this work, the cohesive contact property was used instead of cohesive elements, and the exponential damage evolution law built into the Abaqus software (Abaqus User Manual, 2012) was employed. The use of cohesive contact allows for the incorporation of friction automatically. The use of the software's built-in features was found to describe the interface response of the modified napkin ring specimen with good accuracy.

In the following, the traction-separation law for the quasi-static fracture is formulated as defined in the finite element software, Abaqus (Abaqus User Manual, 2012). Initially, linear elastic behaviour is assumed. The tractions are related to the separations through a stiffness matrix

$$\mathbf{t} = \begin{Bmatrix} t_n \\ t_s \\ t_t \end{Bmatrix} = \begin{bmatrix} \kappa_{nn} & \kappa_{ns} & \kappa_{nt} \\ \kappa_{ns} & \kappa_{ss} & \kappa_{st} \\ \kappa_{nt} & \kappa_{st} & \kappa_{tt} \end{bmatrix} \begin{Bmatrix} \delta_n \\ \delta_s \\ \delta_t \end{Bmatrix} = \boldsymbol{\kappa\delta} \qquad (2)$$

The components of the traction vector t_n, t_s, t_t, correspond to the normal and the two shear tractions, respectively. The corresponding separations are δ_n, δ_s and δ_t. The stiffness matrix is defined as uncoupled by setting all of the off-diagonal stiffness parameters to zero.

The failure criterion is defined by maximum stresses. Damage is assumed to initiate at a contact point when the ratio of traction and critical traction reaches the value of one

$$\max\left\{ \frac{\langle t_n \rangle}{t_n^0}, \frac{t_s}{t_s^0}, \frac{t_t}{t_t^0} \right\} = 1 \qquad (3)$$

where t_n^0, t_s^0, t_t^0 are the critical tractions in the normal and in the two shear directions, respectively. The Macaulay brackets $\langle\ \rangle$ indicate that purely compressive traction does not initiate damage. Further loading causes the traction to be degraded according to the damage evolution equation, which can be linear, exponential or user-defined. After damage initiation, the tractions are defined as

$$\begin{aligned} t_n &= \begin{cases} (1-D)\bar{t}_n & , \ t_n \geq 0 \\ \bar{t}_n & , \ \text{otherwise} \end{cases} \\ t_s &= (1-D)\bar{t}_s \\ t_t &= (1-D)\bar{t}_t \end{aligned} \qquad (4)$$

where D is a scalar damage variable and $\bar{t}_n, \bar{t}_s, \bar{t}_t$ are the traction components according to the elastic traction-displacement behaviour without damage.

In order to define damage under multi-axial loading conditions, the effective separation is defined:

$$\delta_m = \sqrt{\langle \delta_n \rangle^2 + \delta_s^2 + \delta_t^2} \qquad (5)$$

In this work, the damage evolution is defined as exponential degradation of the traction stress, as shown in Fig. 10. The model is initially linear-elastic until one of the traction components reaches its critical value. The separation corresponding to the critical traction is denoted as $\delta_m{}^0$. After damage initiation, the traction degrades exponentially until the attainment of relative displacement at full separation, δ_m^f. For relative displacement beyond δ_m^f, the cohesive tractions are zero. The energy required to fully separate a unit crack area, the cohesive fracture energy, G_c, is given by the area under the traction-separation law. The softening curve and, consequently, the fracture energy are considered as properties of the material.

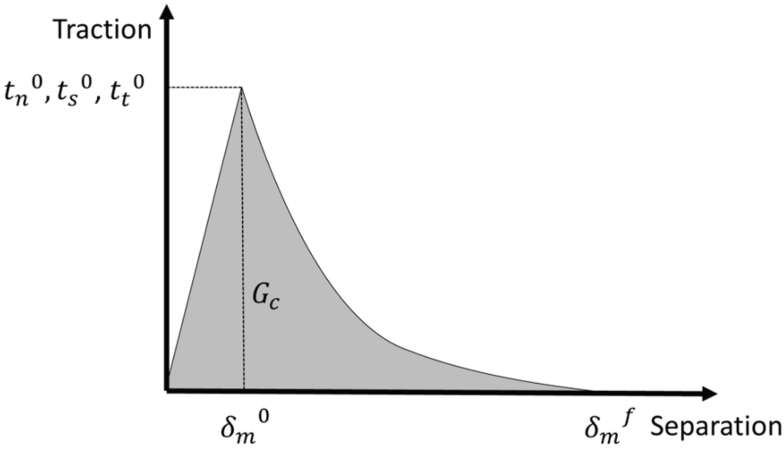

Figure 10. Traction-separation cohesive law with the exponential damage evolution.

The damage variable *D* for the exponential damage evolution is defined as

$$D = 1 - \left\{ \frac{\delta_m^0}{\delta_m^{\max}} \right\} \left\{ 1 - \frac{1 - \exp\left(-\alpha\left(\frac{\delta_m^{\max} - \delta_m^0}{\delta_m^f - \delta_m^0}\right)\right)}{1 - \exp(-\alpha)} \right\} \tag{6}$$

where α is a non-dimensional parameter and $\delta_m^{\max}$ is the maximum relative displacement at the contact point.

The surface-based cohesive behaviour allows for the incorporation of frictional effects into the interface response. If both tangential frictional behaviour and surface-based cohesive behaviour are defined in the interaction property, the frictional model will be activated once damage has initiated. The frictional traction is increased in proportion to the damage and the total traction components at a contact point become

$$\begin{aligned} t_n &= \begin{cases} (1-D)\bar{t}_n \ , & \bar{t}_n \geq 0 \\ \bar{t}_n \ , & \text{otherwise} \end{cases} \\ t_s &= \begin{cases} (1-D)\bar{t}_s \ , & \bar{t}_n \geq 0 \\ (1-D)\bar{t}_s - D\mu\bar{t}_n \ , & \text{otherwise} \end{cases} \\ t_t &= \begin{cases} (1-D)\bar{t}_t \ , & \bar{t}_n \geq 0 \\ (1-D)\bar{t}_t - D\mu\bar{t}_n \ , & \text{otherwise} \end{cases} \end{aligned} \tag{7}$$

3.2.2 Determination of the cohesive zone model parameters from quasi-static tests on the modified napkin ring specimen

The calibration of the parameters was carried out with a simple model of two blocks, as shown in Fig. 11, using the finite element software, Abaqus.

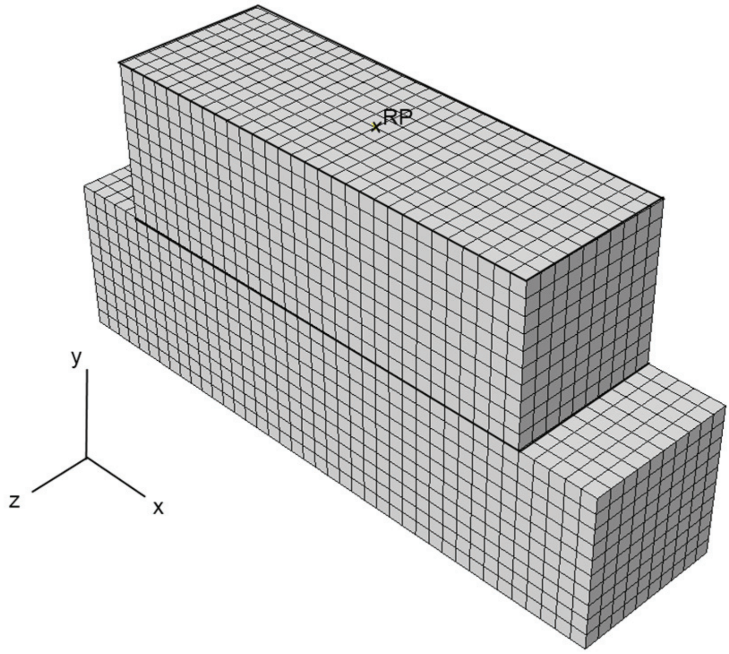

Figure 11. Finite element model to calibrate the parameters for the cohesive interface definition.

Both blocks measured 2 mm in width and the top and bottom blocks measured 6 mm and 8 mm in length, respectively. The blocks were given the material properties of steel (E = 210 GPa, ν = 0.3) and the surface-based cohesive behaviour and tangential penalty friction were defined as contact properties of the interface between the blocks. The loading was applied through boundary conditions to the reference point (RP) on the top surface. All of the nodes on the top surface were constrained to the reference point through the coupling constraint, in order to ensure that all displacements on the top surface were the same. All translations were restrained on the bottom surface. Firstly, the normal clamping stress was applied by imposing a displacement in the negative y-direction on the reference point. The displacement was selected so that the average compressive normal stress at the contact interface was 4 MPa, 50 MPa or 100 MPa. Next, a velocity boundary condition in the x-direction was applied to the reference point while maintaining the compressive displacement. The upper block was allowed to slide by approximately 1 mm.

According to Eq. (7), the resulting peak traction in the shear direction is the sum of the cohesive and frictional tractions, as is the traction during damage evolution. Therefore, the critical traction and damage evolution of the pure cohesion cannot be directly deduced from the napkin ring experimental data with clamping stress. Instead, the cohesive parameters have to be determined through trial and error, until the modelled response corresponds to the experimental response.

The values for the stiffness, the coefficient of friction and the damage exponent were chosen based on earlier investigations (Oinonen and Marquis, 2011b). As explained in more detail in (Oinonen and Marquis, 2011b), the damage is expected to reach the value of $D = 1$ when $\delta_m^f = 1\ \text{mm}$. The value of the critical traction was calibrated for the surface-based cohesive contact model. The values of the contact parameters to be used for the DLJ simulation are shown in Table 7. The shear properties are assumed to be equal in both directions, i.e., $\kappa_{ss} = \kappa_{tt}$ and $t_s^0 = t_t^0$. In the absence of experimental data in the normal direction, the same stiffness and damage evolution properties are assumed as in the shear directions. The peak shear stress in the normal direction, t_n^0, is also unknown. For the sake of prudence, it was supposed that interfaces under tensile normal stress do not contribute to fatigue strength. The t_n^0 was presumed to be very small, which results in early damage in the contact points under positive normal stress. As a result, shear stresses are obtained only at the interface areas under compressive normal stress. This approach is expected to yield somewhat conservative results.

Table 7. Properties calibrated for the surface based-cohesive interaction.

Interface property	Value
κ_{nn}	3000 N/mm
$\kappa_{ss} = \kappa_{tt}$	3000 N/mm
μ	0.44
α	5.33
δ_m^f	1 mm
t_n^0	1 MPa
$t_s^0 = t_t^0$	55 MPa

The simulated and experimental failure responses of the interfaces with clamping stresses q = 4 MPa, q = 50 MPa and q = 100 MPa are shown in Fig. 12. It can be seen in the figure that no data points were recorded right after damage initiation in the case of the q = 4 MPa specimens. The increase in relative displacement caused by sudden failure was so rapid that the measuring equipment was unable to collect any data points for several hundred µm of relative displacement. Consequently, the cohesive zone model parameters are calibrated only from the specimens with the clamping stresses q = 50 MPa and q = 100 MPa. However, it can be seen that the calibrated model describes the response of the q = 4 MPa specimen with good accuracy, assuming that damage evolution occurs according to the exponential scheme.

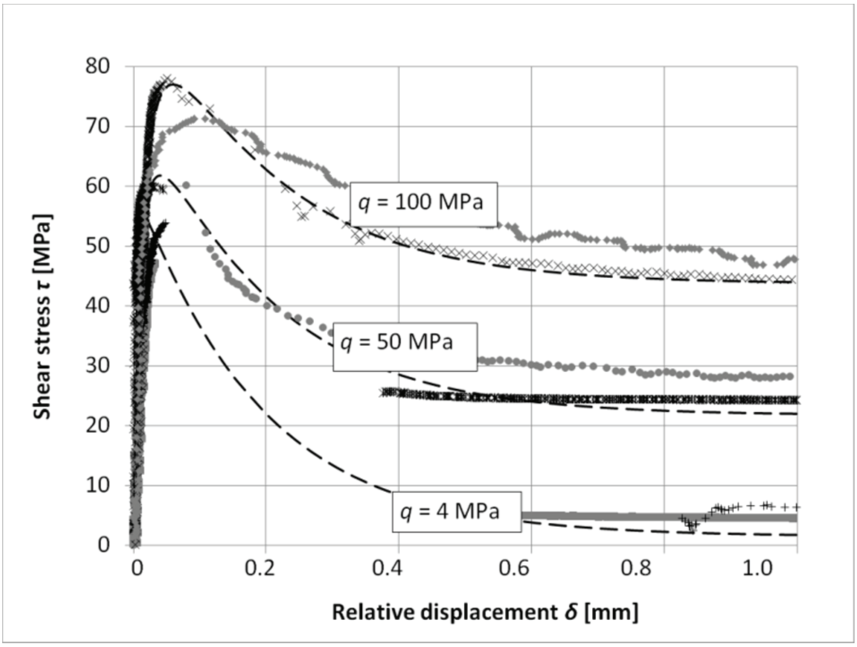

Figure 12. Experimental data (markers) and simulated failure responses (dashed lines) of the clamped and bonded interfaces under q = 4 MPa, q = 50 MPa and q = 100 MPa clamping stresses.

The coefficient of friction was chosen based on the behaviour of the specimens under q = 100 MPa clamping stress.

The properties of the cohesive zone model were not given a statistical distribution. Instead, the parameters were chosen using careful consideration so as to be representative of the entire set of quasi-static experimental data. The parameters should be assigned values with known statistical distribution, in order to the assure reliability of the model. However, this would require extensive experimental campaigns, and there are still many outstanding issues related to understanding the physics of the various parameters used in the cohesive zone model, before it could be cost-effective to launch such experimental programmes for statistical assessment.

3.2.3 Modelling issues

Contact modelling in Abaqus/Standard often leads to convergence issues which are overcome by damping assignments. Consequently, viscous regularisation damping was used in this work. The effect of the regularisation on the solution accuracy was estimated by conducting the same simulation with three different values of the viscosity coefficient, then comparing the results. It was observed that increasing the coefficient from 0.0001 to 0.0002 and 0.001 produced virtually identical results, while the calculation time was reduced to half and to one quarter, respectively. Thus, the viscous coefficient of 0.001 was used in subsequent simulations.

The simulation was performed with different mesh sizes so as to ensure that any error related to mesh size was minimal. The computed shear stresses changed by approximately 2 % as the mesh size was increased from 1 mm to 1.5 mm. Refinement of the mesh beyond 1 mm resulted in convergence problems and very lengthy calculation times. The calculation was deemed converged with the mesh size of 1 mm, due to the relatively small change in the stress results upon increasing the mesh size.

Shear stress results are affected by the values of the contact interaction parameters. In order to evaluate the significance of the effect, the model was run three additional times and for each separate run, a different parameter (cohesive stiffness K_{nn}, K_{ss}, K_{tt}, damage evolution coefficient, α, or coefficient of friction, μ) was increased to three times the initial value. It was found that the increase in the cohesive stiffness had a significant effect on the resulting shear stress values, while the other parameters had less impact. Increasing the stiffness and the damage evolution coefficient made the convergence more difficult as damage behaviour became less smooth.

4. Results and discussion

4.1 Observations on interface failure of the modified napkin ring specimen

The fractured bonded surfaces in the modified napkin ring specimens were inspected in order to understand the failure process. The specimens were photographed with the aid of an optical microscope, in addition to visual inspection. The damage in the bond-line was studied from three modified napkin ring specimens using a scanning electron microscope.

4.1.1 Failure modes

Different failure modes were identified in the test programme for different interface conditions. Shear decohesion, as evidenced by the sudden relative slipping of the interfaces, was the primary fatigue failure mode for bonded interfaces under low clamping stress (q = 4 and 50 MPa). Shear decohesion was characterised by very low measured relative displacement amplitudes, followed by sudden slipping and fracture of the interface. A graph illustrating typical relative displacement, δ_a, vs. number of cycles, N, data for a specimen with shear decohesion failure is shown in Fig. 13 a.

Fretting was observed in most of the specimens with high clamping stress (q = 100 and 150 MPa), as well as in non-bonded specimens with low clamping stress. The failure of the non-bonded interfaces with low clamping stress was found to be fretting wear, where very high relative displacement amplitudes and excessive formation of fretting debris were characteristic. In most cases, the specimens with high clamping stress failed due to fretting fatigue; however, there were cases which resulted in sudden slipping of the bonded specimens. Fretting fatigue was distinguished from fretting wear in that the measured relative displacements were lower and the surfaces revealed signs of spalling, metal transfer between surfaces (Fig. 14) and, for some specimens, visible macro-cracking (Fig. 15). A relative displacement vs. number of cycles curve for fretting fatigue failure is presented in Fig. 13 b. It can be seen from the figure that the measured displacement amplitudes are significantly higher than those for the shear decohesion failure. Photographs of metal transfer and fretting fatigue cracking are provided in Figs. 14 and 15, respectively. All of the napkin ring fatigue tests are tabulated in Appendix A, with the observed failure mode provided for each specimen. Photographs of the fractured interfaces with the different failure modes are presented in Fig. 16.

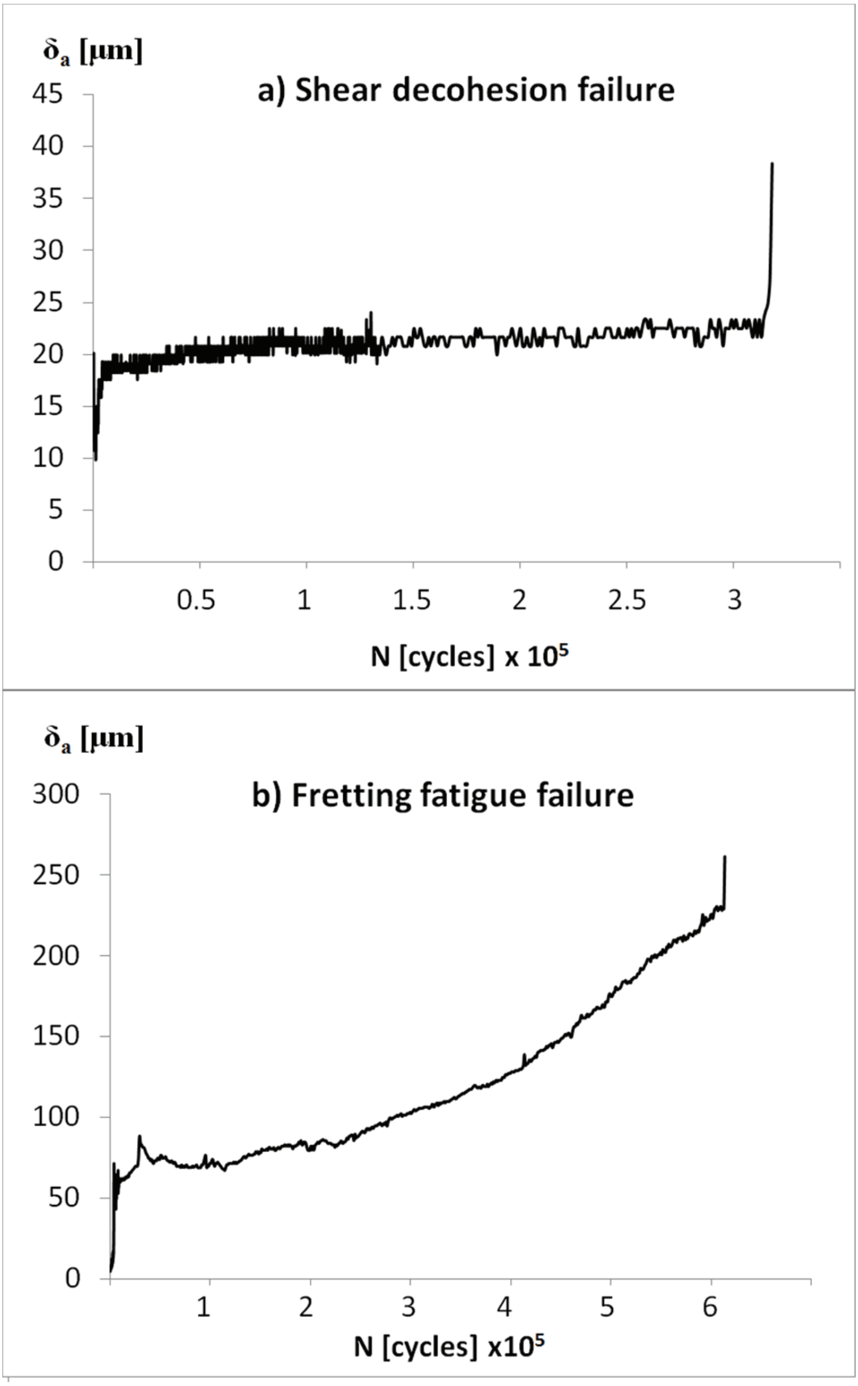

Figure 13. Relative displacement δ_a vs. number of cycles, *N*, measured from specimens with the two different failure modes: a) Shear decohesion and b) Fretting fatigue.

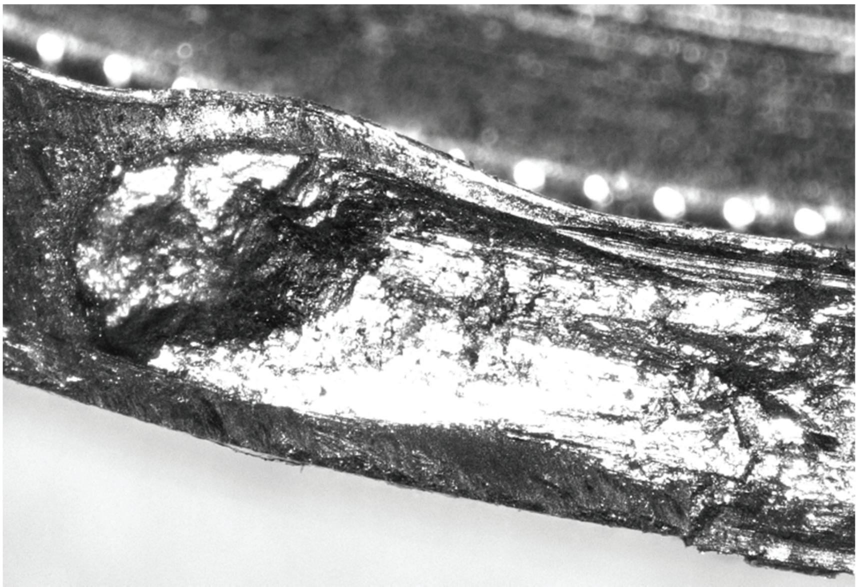

Figure 14. Metal transfer at the specimen surface after fretting fatigue failure.

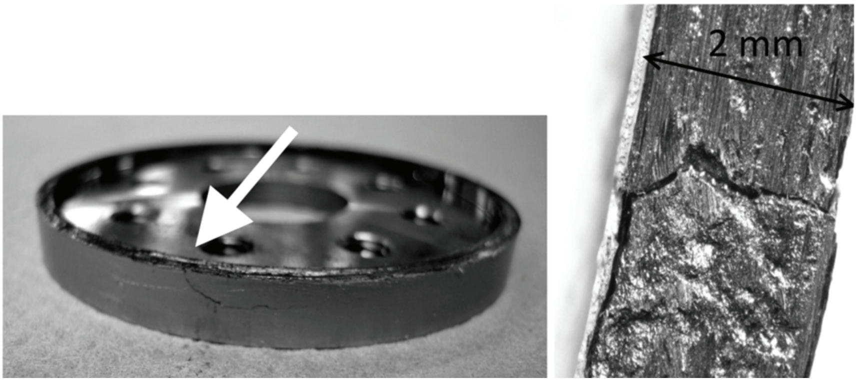

Figure 15. Crack in the HSS specimen after fretting fatigue failure. Photograph of the entire specimen and highly-magnified view of the fretting crack.

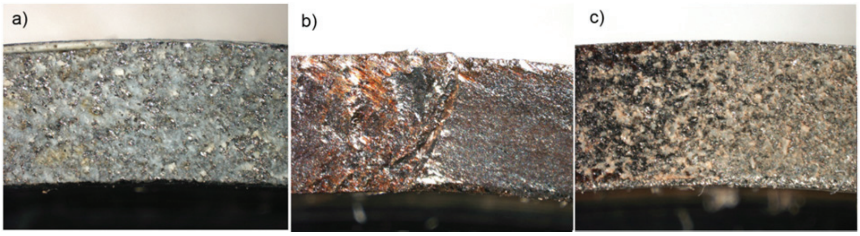

Figure 16. Selected optical microscope photographs of grit blasted interfaces after fatigue testing: a) bonded q = 50 MPa specimen with shear decohesion failure, b) bonded q = 150 MPa specimen with fretting fatigue failure and crack in the HSS substrate and c) bonded q = 50 MPa specimen after a run-out test (followed by static fracture test).

The interface failure due to fretting fatigue occurs at a stress concentration. However, the modified napkin ring specimen was designed to be free of stress concentrations. In reality, it is very difficult to manufacture a perfect interface without any local stress concentrations. In the case of the modified napkin ring specimens, the stress concentration where fretting fatigue initiates is the location with the largest area of metal-to-metal contact, which can occur at any location along the interface. Furthermore, it can be concluded that the fretting fatigue at a clamped and bonded interface is a possible failure mode, even without any structural stress concentration sites. In real joints, however, stress concentrations are almost always present, and the location critical to fretting fatigue can be identified in design.

4.1.2 SEM analysis of damage

Scanning electron micrographs were taken from specimens I4 and I5 of Table 2. In addition, one specimen in the initial state, i.e. following curing but prior to cyclic loading, was studied by SEM. The specimens were cut in the radial and tangential direction in two locations and SEM pictures were taken of the adhesive in the cut sections. Selected pictures from all of the specimens are provided in Appendix B.

It was found that the specimen contained multiple cracks, voids and inclusions already in the initial state. These could have been caused by several different factors: insufficient mixing of the two components of the adhesive; foreign matter such as dust on the bonded surface; poor wetting; residual stresses caused by thermal expansion of the substrate and the adhesive during curing; stresses imposed on the interface during the detachment of the specimen from the test rig or cutting the specimen for SEM. An example of a void can be seen in Fig. 18a.

The bonded interface was found to be thicker on one side of the specimen than on the other side, as can be observed in Figs. 17 a and b. The highest thickness measured from the SEM pictures was 180 µm. The thin section in the 4-MPa-specimens had the average thickness of 30 µm, with some locations where thickness was close to zero when two surface roughness peaks were located opposite to each other. A different damage pattern can be found in the areas with different thicknesses. The thin areas were mostly cracked near the interface between the steel and the adhesive, as shown in Figs. 18a and c, while the thick areas had numerous inclusions that acted as initiation points for cracks. See Figs. 18 b and d.

The control of interface thickness to the micrometer scale is challenging with reasonable machining tolerances in manufacturing the test rig and the specimens. The fact that the thickness varied undoubtedly will cause some scatter in the results. However, in spite of the thickness variation, the failure of the entire interface can be considered to occur when the thin section fails, as the local shear stress in the adhesive in the thin section is higher than that in the thick section.

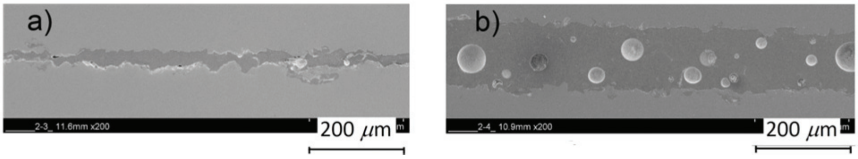

Figure 17. Bonded sections in specimen I4. The sections were taken from two different locations on opposite sides of the specimen.

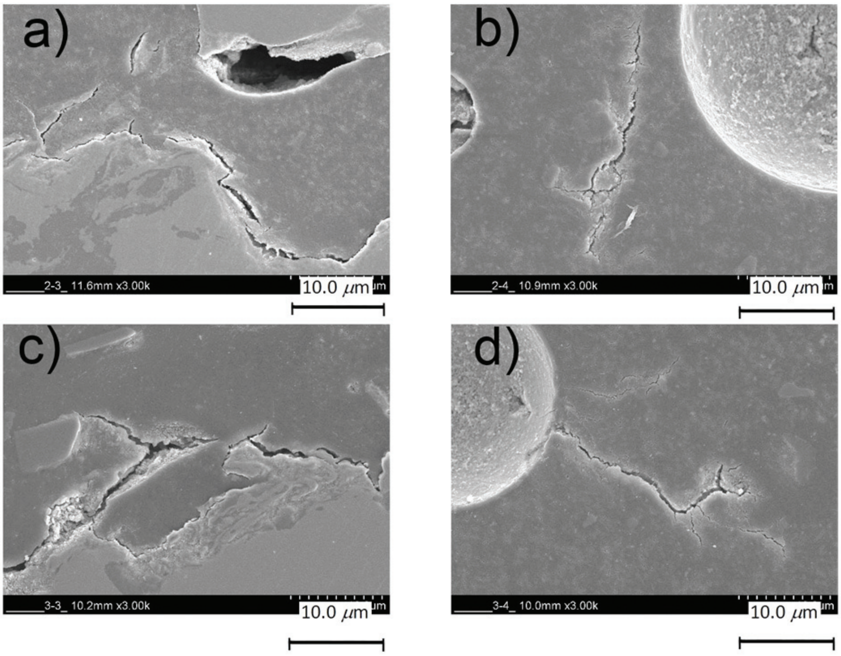

Figure 18. Magnifications of typical cracks in tangential cuts in specimen I4 (a and b) and specimen I5 (c and d).

Cracking at the interface between the substrate and the adhesive is usually related to insufficient adhesion. However, cracks are found to simultaneously initiate and grow in the adhesive material and at the interface. Thus, it is due to stress concentration, not poor adhesion, why the cracks are found at the interface.

An inspection of the cracks reveals that the damaged specimens have cracks with a very different morphology than the undamaged (initial state) specimen. The damaged specimens have cracks visible in the tangential cuts that have a zig-zag shape and that are branched. These cracks initiate from the inclusions, voids and the interface. Branched cracks were not visible in the radial cuts, which indicates that branching is due to crack growth in the direction of cyclic loading. Examples of the fatigue cracks are shown in Fig. 18.

The majority of cracks identified as fatigue cracks were found to propagate at the angle of ±30-50° relative to the plane of the bonded layer. The orientation of the cracks implies that they grew as mode I cracks due to the maximum tensile stress. Mode I cracks under nominally shear loading were also observed by

Chai (1993a) from static fracture tests using the napkin ring specimen. However, the microcracks due to static loading grew straight through the thickness, whereas the fatigue cracks had a zig-zag shape and several branches. A relatively large number of the cracks also demonstrated other orientations, ranging from 4 to 90°.

The lengths of the fatigue-induced cracks were measured from the pictures of specimens I4 and I5, of which I5 had the greater degree of computed damage accumulated before interrupting the fatigue test. The total length of fatigue cracks in specimen I5 seems to be approximately 14 % higher than that of specimen I4. However, the distinction of fatigue cracks from flaws initially present in the bond is not so clear and the number of SEM observations is limited. Accordingly, the damage cannot be fully and reliably quantified based on the SEM analyses performed in this work. It does, however, open up a promising direction for further study.

Discussion

The orientations of the cracks varied greatly which can be attributed to the fact that the local stress fields affecting the cracks were not uniform, due to the contours of the surface roughness and existing voids and inclusions. Especially under the conditions in Figs. 18 a and c, where the interface thickness is very small, the asperities of the surface roughness give rise to a highly-variable, local stress field in the adhesive, causing the cracks to grow in different orientations. Most of the studies on adhesive joints have included the polishing of the bonded surfaces. However, in many industrial applications, grit-blasting is a more realistic surface treatment method. Consequently, it would be interesting to further study the effect of substrate roughness on the bondline stress field.

It is worthwhile to mention that the fatigue cracks were not found to extend through the thickness of the adhesive layer and, for that reason, they did not generally enable contact between the metal asperities. However, the cracks due to static damage (Chai, 1993a) did extend through the thickness and, thus, they can be suspected to enable metal-to-metal contact.

The design of the test setup imposed some limitations on the SEM analysis. The specimens had to be detached from the test set-up and clamping had to be released when they were taken for imaging. For specimens under high clamping stress, the detachment from the test setup will create some tensile stress to the adhesive as the elastic compression in the asperities of the contacting metal surfaces is released. As a result, experience has shown that many of the specimens fracture. In order to perform the SEM analysis for interfaces under high clamping stress, the specimen attachment fixture should be designed so that the specimen can be removed without releasing the clamping. Due to the limitations of the test setup, the SEM study was only conducted on specimens with the q = 4 MPa clamping. In order to obtain a full understanding of the damage processes in the bonded and clamped interface, the SEM study should be performed for interfaces with different clamping stresses. In addition, the static damage could not be assessed with SEM in the current study.

Although it is not a perfect assumption to treat the interface as a uniform entity, the overall behaviour of the napkin ring specimen can be considered as approximately equivalent to the behaviour of the representative interface area, subjected to pure shear stress. The cohesive zone modelling approach is adopted in the analysis of the interface and, thus, there is no need to define the thickness. Instead, the overall response is used to characterise the interface. Moreover, the SEM micrographic analysis shows that the fatigue failure process in the interface is complex, and would be difficult to assess with methods other than damage mechanics.

4.2 Observations on failure of the double lap joint specimen

The fractured bonded surfaces in the double lap joints were inspected visually. All fatigue test results can be plotted to a load vs. number of cycles chart, as illustrated in Fig. 19.

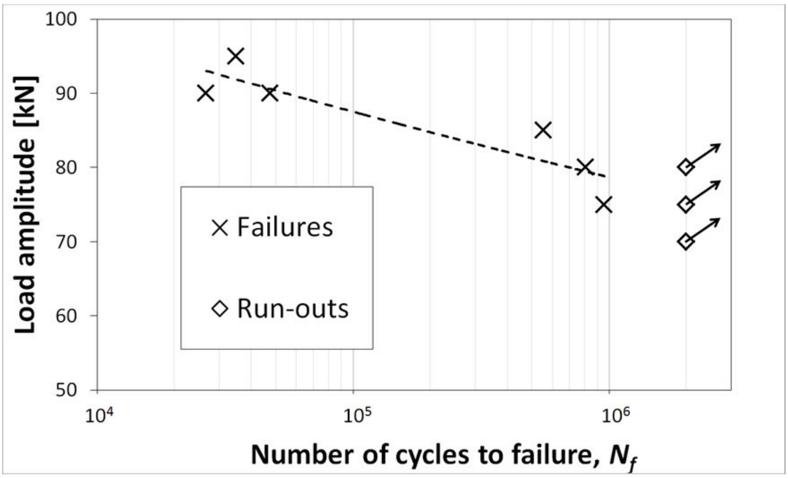

Figure 19. Load vs. fatigue life results of the DLJ specimens.

The data are limited, but some conclusions can be drawn from the fatigue failures. The specimens loaded with amplitudes of F_a = 90 and 95 kN had much shorter fatigue lives than the specimens loaded with lower amplitudes. The difference was due to the failure type which was found to be different depending on the load and the life. The specimens with long lives had severe fretting damage in the contact interfaces, as evidenced mainly by the formation of fretting debris and wear marks, while the specimens with short lives were less damaged by fretting. With high loads, failure is dominated by the progressive failure of the adhesive, and there is not enough time for fretting damage to occur before final failure occurs. Fig. 20 presents the fractured interfaces of specimens B 4 (long life) and B 8 (short life) after fatigue loading and disassembly. Severe fretting damage can be seen in specimen B 4 around both the small and large bolt holes on the loading side. Similar but milder fretting damage can be observed around the small hole in specimen B 8. The fretting damage around the large bolt hole in specimen B 8 is different. In this case, most of the fretting damage is located in the area under normal compression. All specimens that failed at a relatively low number of cycles ($N_f < 10^5$ cycles) sustained this type of damage around near at least one of the bolt holes.

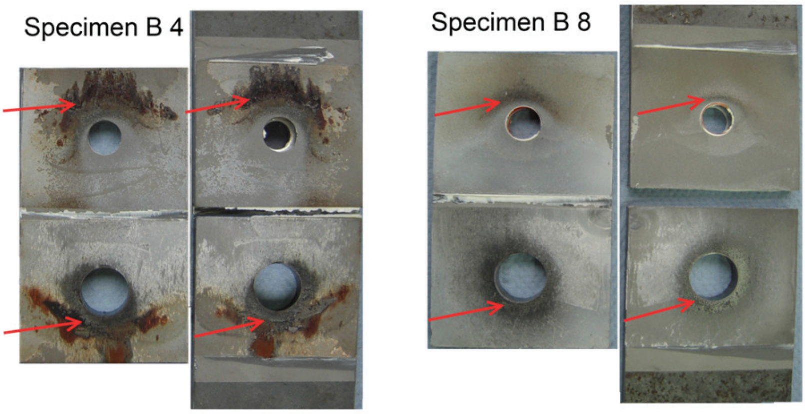

Figure 20. Specimens B 4 and B 8 after fatigue failure and disassembly.

Although fretting damage was found in most of the cyclically-loaded specimens, the final failure was caused by shear decohesion. This is deduced because no cracks were found in the steel specimens. However, when contemplating the design of hybrid bonded/bolted joints, the risk of fretting fatigue should be considered. Fig. 21 shows the interface of the main plate under the small bolt in one specimen with the fretting debris removed. There is a notch which was formed due to fretting and which could act as an initiation point for fatigue cracks. It is worthwhile to point out that the addition of adhesive into the bolted joint dramatically changes the fatigue behaviour of the joint. The same DLJ specimen without adhesive would be in the gross slip state at axial loads much lower than the ones applied here. Since the bonded and clamped interface can withstand higher stress than the plain frictional interface, the bulk stresses in the bonded/bolted joints can be higher than in bolted joints without adhesive, and the risk of fretting fatigue and the resulting crack growth should be assessed.

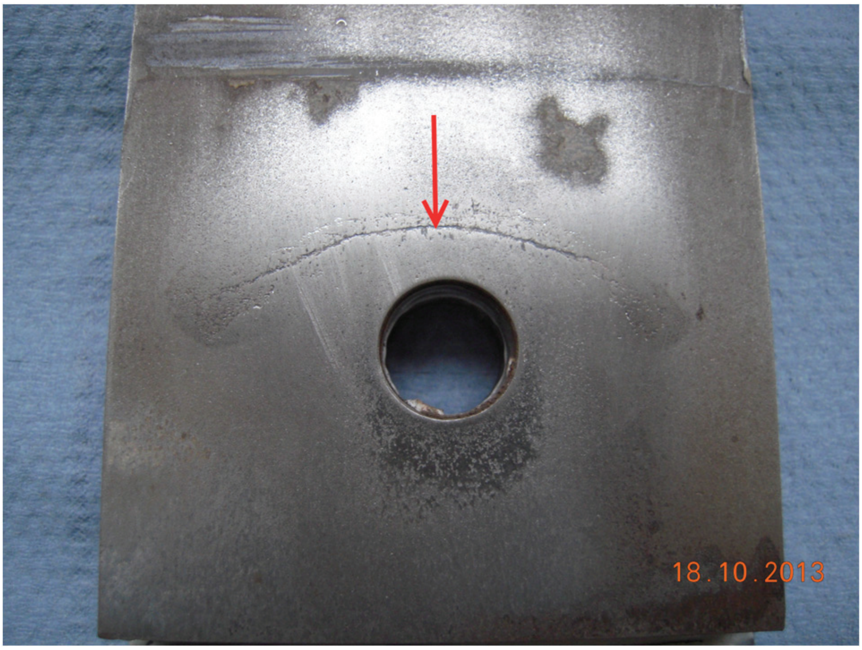

Figure 21. Fracture interface of the main plate under the small bolt after removal of fretting debris. (For details of specimen geometry, see Fig. 6). A notch has been formed at the edge of compressive contact due to fretting.

The displacement response of the DLJ specimens during fatigue loading was measured by the built-in displacement sensor of the fatigue test machine and, for most specimens, a clip-on gauge was attached to one side of the gap between the two main plates. Typically, the specimen response was linear-elastic at the beginning of the fatigue life. Towards the end of the fatigue life, slipping hysteresis was measured by the clip-on gauge. The measured slip amplitude vs. the number of cycles for specimen B 4 (see Table 3) is presented in Fig. 22. The load-displacement (F-Δ_{gap}) loops measured by the clip-on gauge are shown at $5x10^5$, $7x10^5$ and $8x10^5$ cycles.

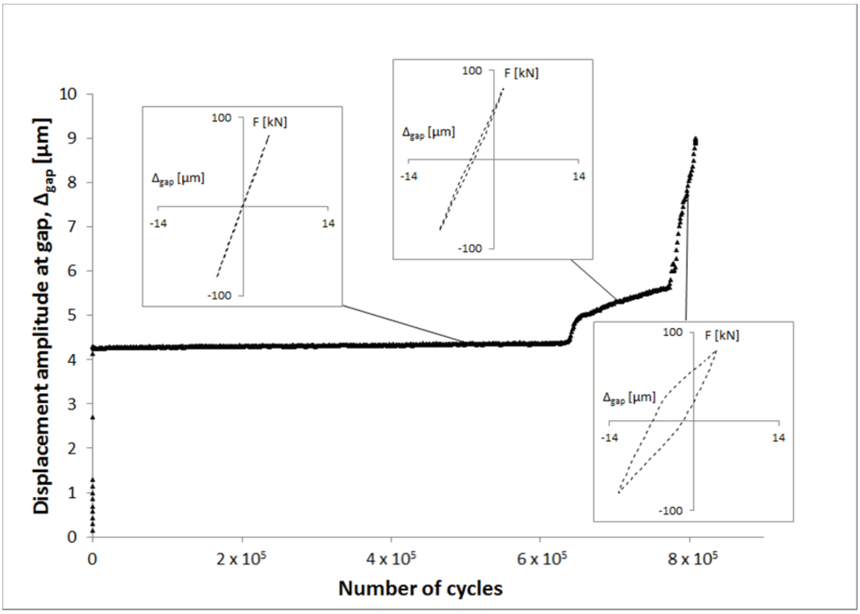

Figure 22. Displacement amplitude measured at the gap between the main plates vs. the number of cycles on specimen B 4. The load – displacement hysteresis is shown at 5x10^5, 7x10^5 and 8x10^5 cycles.

The shape of the displacement amplitude curve in Fig. 22 is typical for all specimens that failed in fatigue. Initially, there is a region of very slow but steady increase in the slippage, characterised by linear-elastic load-displacement response. After a relatively large number of cycles, a sharp increase in slippage occurs and slipping hysteresis is measured during the subsequent loading cycles. With an increase in cycles, the rate in the increase in slippage tends to decrease; however, final failure occurs during a relatively small number of cycles. In the first region, the load is hypothesised to be carried almost exclusively by the adhesive, with slow progressive damage occurring in the adhesive due to the cyclic loading. Damage in the adhesive can be considered to be composed of several micro-cracks, as shown in Section 4.1.2. A more detailed discussion of the damage will be provided later in this thesis. The sharp increase in slippage occurs after the damage in the adhesive has reached a critical level. The slipping hysteresis observed after this is due to frictional sliding. The specimen contains four interfaces where the damage is effectively not identical. Thus, it is possible that one of the bonded interfaces failed before the others, thereby resulting in the first increase in slippage. The interface on the opposite side of the specimen would have then started to carry most of the load, resulting in relatively fast fatigue failure.

4.2.1 Modified double lap joint tests

Based on the fretting damage in the specimens shown in Fig. 20, it is clear that sliding also occurred in the interfaces under the large bolt, whereas it had been originally planned that only the interfaces under the small bolt would slip. This is the case in static fracture, where the whole interface fails virtually at once.

The specimen was modified for three additional fatigue tests to study the fatigue failure. Two spherical thrust bearings were used under the large bolt instead of regular washers, in order to distribute the clamping stress to a wider area which encompassed almost the entire interface area. The diameter of the bearing was 55 mm and its thickness, 20 mm. At the same time, the effect of bolt pre-load was studied. For the first test (test M 1 in Table 4), the small bolt had the same pre-load (43 kN) as applied in all previous fatigue tests. The other two tests were conducted with different pre-loads on the small bolt, specifically, 10 kN (test M 2) and 55 kN (test M 3). The loading amplitude was chosen so that a similar type of failure would be obtained. The modified fatigue tests were summarised in Table 4.

The specimen M 1 had a significantly longer fatigue life than specimens with the initial configuration that were loaded with the same amplitude (see Tables 3 and 4). Ideally, all of the specimens would fail in the same location. However, the factors affecting the total strength of the joint, such as surface roughness and adhesive material properties, have a statistical nature. As a result, the greater the number of possible failure locations, i.e., locations with a high stress concentration, the higher the probability of early failure. With the bearing washer modification, the number of locations with high stress concentrations was reduced and, because of this, it is logical that a longer fatigue life was measured. Fretting fatigue with a notch similar to Fig. 21 was observed around the small bolts in the modified tests M 1 and M 3, while the plates under the bearing washer and large bolt had no such signs of stress concentrations. Nevertheless, the areas under the large bolt were damaged due to fretting and some of them failed during the tests. The interfaces of specimen M 1 are shown in Fig. 23.

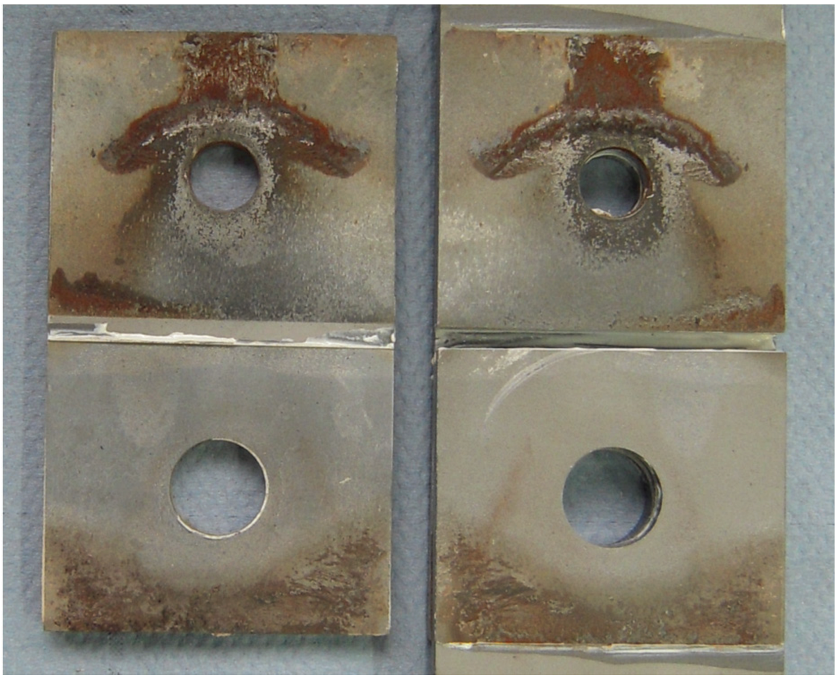

Figure 23. Bonded surfaces of specimen M 1 after fatigue failure and disassembly. Cover plate on the left and main plates on the right.

The modified specimen M 2, which had the lowest bolt pre-stress, failed differently, as compared to the other specimens; specifically, there was no fretting damage. The ability of the joint to sustain loading was lower than for specimens M 1 and M 3, which indicates that the clamping stress improved the joint fatigue strength. The same has been observed for plain bolted joints (Benahmena et al., 2010; Chakherlou et al., 2013; Wagle and Kato, 2009), however, with higher clamping stress, the risk of fretting fatigue is increased. As a result, the bolt pre-stress has been found to increase the fatigue strength up to a point, but after fretting fatigue occurs, further increase in pre-stress does not improve the fatigue strength. Indeed, based on the limited results here, the increase in clamping stress does not seem to increase the fatigue strength of the bonded and clamped joint after the occurrence of fretting, which can be observed by comparing the fatigue life of specimens M 1 and M 3 in Table 4.

Even though the thrust bearing distributed the load to a wide area, the specimen still showed some fretting damage at the interface under the large bolt, although the stress concentration acting as a possible initiation location for fretting cracks was avoided. In real joints, it is very difficult to apply uniform clamping to the entire bonded area. Accordingly, the edge of compressive contact should be considered as the critical location for fatigue damage. Furthermore, the results imply that clamping with bolts does increase the fatigue life, but only up to a point. A thorough study on the effect of bolt pre-load and bolt size on the fatigue strength would provide invaluable data for the optimal design of bonded/bolted hybrid joints.

4.3 Cyclic step tests

Low-frequency cyclic step tests were performed on modified napkin ring specimens with the fine-ground interface, in order to measure the amount of irreversible small-scale slip between the interfaces. The irreversible slipping is attributed to plastic yielding of the adhesive material. In all of the assessments in this thesis, the adhesive is assumed to behave in a linear elastic manner. Nevertheless, it is important to observe whether the plasticity of the adhesive should be accounted for.

Three specimens were tested, one for each q = 50, 100 and 150 MPa. Total relative displacement of the interfaces was assumed to consist of elastic and inelastic portions. Inelastic displacement was modelled with a power law function. The relative displacement was normalised with the critical relative displacement, δ^0, which corresponds to the critical traction of the adhesive at the initiation of damage (see Chapter 3.2.1). The value of δ^0 is $\delta^0 = t_0^s / \kappa_{ss}$ = 55 / 3000 = 0,01833 (mm) (See Table 7). The shape of the hysteresis loop is consequently given by

$$\frac{\Delta\delta}{\delta^0} = \frac{\Delta\tau}{A_1} + \left(\frac{\Delta\tau}{A_2}\right)^{A_3} \tag{8}$$

In this equation, A_1, A_2 and A_3 are constants, $\Delta\delta$ is the change in relative displacement and $\Delta\tau$ is the change in shear stress. The shear stress amplitude, τ_a, the irreversible, elastic and total displacement amplitudes, $\delta_{a,i}$, $\delta_{a,e}$ and $\delta_{a,t}$, respectively, and the fitting constants for all pre-stress cases q = 50, 100 and 150 MPa are provided in Tables 8–10. The relative displacement amplitudes are obtained by multiplying with the critical relative displacement. The method of fitting Eq. (8) in the data is outlined in detail in Appendix C, along with a method to estimate the measurement precision. The precision of the interface relative displacement measurement was determined to be 2.4 µm. This value is relatively large with respect to the total relative displacements being measured. For this reason, the values in Tables 8–10 should be considered as only semi-quantitative. In spite of the limitations of the displacement measuring system, the characteristics of the hysteresis behaviour can be assessed with this method. Hysteresis loops of the relative displacement vs. the applied shear stress obtained by fitting Eq. (8) into the measured data are presented in Figs. 24–26.

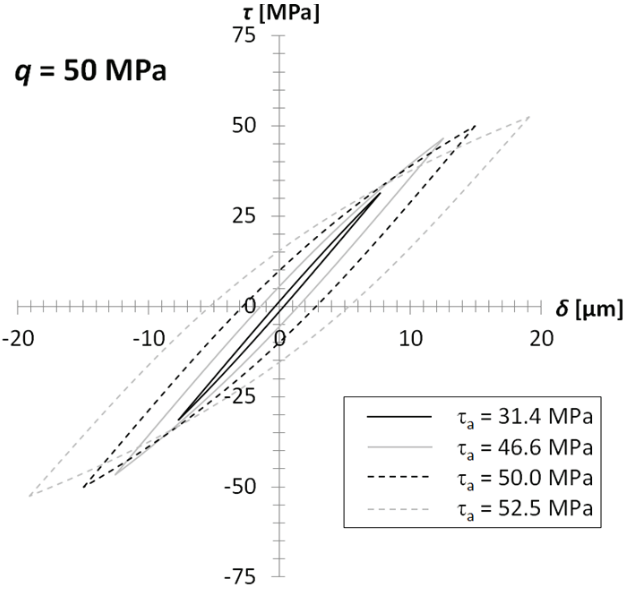

Figure 24. Hysteresis loops of shear stress, *τ*, vs. relative displacement, *δ*, for *q* = 50 MPa.

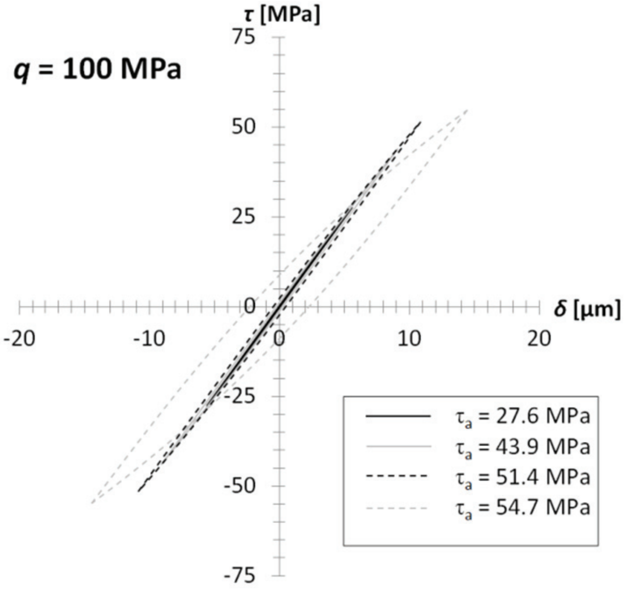

Figure 25. Hysteresis loops of shear stress, *τ*, vs. relative displacement, *δ*, for *q* = 100 MPa.

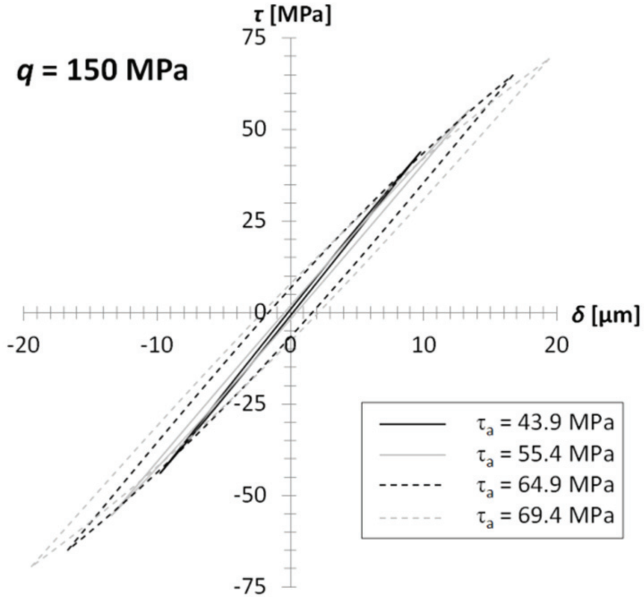

Figure 26. Hysteresis loops of shear stress, *τ*, vs. relative displacement, *δ*, for *q* = 150 MPa.

Table 8. Cyclic step test results for q = 50 MPa. The fitted values of the total relative displacement amplitude, $\delta_{a,t}$, the linear portion, $\delta_{a,e}$, and the inelastic portion, $\delta_{a,i}$, are shown for each shear stress amplitude, τ_a. The parameters of the power law fit, A_1, A_2 and A_3, are also listed.

τ_a [MPa]	$\delta_{a,i}$ [μm]	$\delta_{a,e}$ [μm]	$\delta_{a,t}$ [μm]	A_1 [MPa]	A_2 [MPa]	A_3
11.2	0.01	2.60	2.61	79	147	3.7
31.4	0.39	7.29	7.68	79	147	3.7
46.6	1.70	10.81	12.51	79	147	3.7
48.7	3.06	11.30	14.36	79	131	3.7
50.0	3.38	11.60	14.98	79	131	3.7
52.5	6.34	12.83	19.17	75	116	3.7

Table 9. Cyclic step test results for q = 100 MPa. The fitted values of the total relative displacement amplitude, $\delta_{a,t}$, the linear portion, $\delta_{a,e}$, and the inelastic portion, $\delta_{a,i}$, are shown for each shear stress amplitude, τ_a. The parameters of the power law fit, A_1, A_2 and A_3, are also listed.

τ_a [MPa]	$\delta_{a,i}$ [μm]	$\delta_{a,e}$ [μm]	$\delta_{a,t}$ [μm]	A_1 [MPa]	A_2 [MPa]	A_3
27.6	0.06	5.50	5.56	92	219	3.7
43.9	0.31	8.75	9.06	92	219	3.7
51.4	0.56	10.24	10.80	92	210	3.7
54.7	3.04	11.40	14.44	88	158	3.0

Table 10. Cyclic step test results for q = 150 MPa. The fitted values of the total relative displacement amplitude, $\delta_{a,t}$, the linear portion, $\delta_{a,e}$, and the inelastic portion, $\delta_{a,i}$, are shown for each shear stress amplitude, τ_a. The parameters of the power law fit, A_1, A_2 and A_3, are also listed.

τ_a [MPa]	$\delta_{a,i}$ [μm]	$\delta_{a,e}$ [μm]	$\delta_{a,t}$ [μm]	A_1 [MPa]	A_2 [MPa]	A_3
43.9	0.22	9.58	9.80	84	241	3.7
55.4	0.52	12.86	13.37	79	241	3.7
64.9	1.92	14.69	16.61	81	198	3.7
69.4	2.46	16.96	19.30	75	198	3.7

For each case q = 50, 100 and 150 MPa, the fitting constants in Tables 8-10 are approximately the same for the first cycles and low stress amplitudes, but different for the last and highest loading amplitudes. This is caused by damage which accumulates in the adhesive during the cyclic loading. Also friction has an effect on the response of the interfaces under high clamping stress. The results here show that the load vs. relative displacement response of the bonded and clamped interface is non-linear in reality. However, the non-linear response is pronounced with shear stress amplitudes close to the static shear capacity, and it becomes less meaningful at lower shear stress amplitudes, more likely to occur in structures designed for fatigue. Therefore, the progressive damage model presented later in this thesis will assume linear elastic behaviour during fatigue loading. Nevertheless, the use of the non-linear relationship in future fatigue assessments would be interesting.

4.4 Fatigue strength of the modified napkin ring specimen

Fatigue strength of the modified napkin ring specimens was estimated using the small sample staircase method described in section 3.1. The fatigue strength values, τ_f, corresponding to no failure at $N = 2\text{x}10^6$ cycles, are shown in Table 11 for the bonded and non-bonded modified napkin ring specimens, with the clamping stresses $q \in \{4, 50, 100, 150\}$ MPa and the grit-blasted, fine-ground and coarse-ground surface treatments. Artificial staircase sequences were constructed where needed and the mean fatigue strength was obtained from Eq. (1). The fatigue strength could not be found for some conditions with low clamping stress, because the shear stress amplitudes sustained by the specimens were lower than could be reliably achieved with the test set-up. These cases are marked with *N/A* (not applicable) in Table 11 and, in practice, the fatigue strengths will be lower than $\tau_f = 15$ MPa.

Table 11. The mean fatigue strength, τ_f, corresponding to no failure at $2\text{x}10^6$ cycles obtained by using the small sample staircase method.

q [MPa]	Surface type					
	Grit-blasted, bonded	Grit-blasted, non-bonded	Fine-ground, bonded	Fine-ground, non-bonded	Coarse-ground, bonded	Coarse-ground, non-bonded
4	21 MPa		*N/A*		*N/A*	
50	18 MPa	14 MPa	13 MPa	12 MPa	17 MPa	*N/A*
100	32 MPa	36 MPa	54 MPa	42 MPa	37 MPa	32 MPa
150	67 MPa	65 MPa	53 MPa	67 MPa	61 MPa	60 MPa

For the specimens with high normal clamping pressure (q=100 and q=150 MPa), virtually no increase in the fatigue strength was observed upon the application of the epoxy adhesive. This was a surprising result, given that a nearly two-fold increase in strength was found by adding the adhesive during quasi-static loading (Oinonen and Marquis, 2011b), Table 12. The reason for this behaviour lies in the failure modes. Under cyclic loading the interfaces under high clamping stress fail by fretting fatigue, which is not affected by the adhesive. For the low clamping stresses, on the other hand, the fatigue strength of the bonded interface is higher than that of the non-bonded interfaces, which implies that fatigue is governed by the adhesive.

It should be noted that the results in Table 11 do not support the development of a multiaxial fatigue failure criterion for the adhesive. The fatigue strength of the entire interface increases with clamping stress, but this is due to different failure modes. No increase in the fatigue strength of the bonded interfaces is observed upon increasing the clamping stress from q = 4 MPa to q = 50 MPa. If one wishes to study the effect of normal stress on the fatigue strength of the adhesive, more data points between the clamping stresses q = 4 MPa to q = 50 MPa are needed.

It appears that the only improvement in the fatigue strength of the bonded interface comes from the very low clamping stress, where the shear capacity of the non-bonded interface is inherently zero. The effect of clamping stress seems to be the most pronounced in the fine-ground interfaces. Otherwise, the differences in fatigue strength between the three surface finishes disappear within the precision of the estimation. However, there was an important difference in the failure of the low clamping stress (4 and 50 MPa) cases. The grit-blasted specimen always failed cohesively, i.e., failure in the adhesive, whereas the coarse-ground specimens partially failed cohesively and partially adhesively (failure in the interface between the adhesive and the steel). Adhesive failure should always be avoided in order to exploit the full strength of the adhesive. All specimens were treated identically before applying the adhesive. As a result, it can be suspected that the coarse-ground interface is not suitable for the adhesive joint.

4.4.1 Intermetallic welding

For comparison, the peak shear stress values, τ_{II}^{p}, measured from quasi-static fracture tests for all specimen conditions, are shown in Table 12.

Table 12. The peak shear stress values, τ_{II}^{p}.

q [MPa]	Surface type					
	Grit-blasted, bonded	Grit-blasted, non-bonded	Fine-ground, bonded	Fine-ground, non-bonded	Coarse-ground, bonded	Coarse-ground, non-bonded
4	52 MPa		48 MPa		45 MPa	
50	61 MPa	15 MPa	64 MPa	8 MPa	48 MPa	9 MPa
100	72 MPa	33 MPa	76 MPa	16 MPa	67 MPa	20 MPa
150	98 MPa	49 MPa	81 MPa	25 MPa	75 MPa	28 MPa

It can be seen from Tables 11 and 12 that some of the non-bonded interfaces had higher fatigue strength than static strength. For instance, the fatigue strength of the non-bonded, fine-ground interface was surprisingly high, more than twice the peak static shear strength. This can be explained by intermetallic welding that occurs when the two surfaces rub against each other repeatedly with high pressure. As a result, the interface becomes stiffer. The fatigue tests were started by manually increasing the load amplitude from zero to the target level. This pre-test phase lasted for approximately 2,000 cycles, which was apparently enough for the specimen pairs to become welded. It should be noted, however, that during the design of joints with non-bonded interfaces, it would never be appropriate to assume that the fatigue strength is greater than the static strength.

4.4.2 Residual shear strength

A static fracture test was conducted on some of the run-out specimens after fatigue testing. The measured residual shear strengths, τ_{II}^{res}, for different surface roughnesses are listed in Tables 13-15, along with the ratio of the τ_{II}^{res} to τ_{II}^{p}, with the corresponding surface condition. For the non-bonded interfaces, in most cases, the τ_{II}^{res} was higher than the static shear strength, τ_{II}^{p}, of a specimen which had not previously been subjected to cyclic shear loading. The interface was clearly reinforced by intermetallic welding during cyclic loading. The intermetallic welding was pronounced in the fine- and coarse-ground interfaces. For the bonded run-out specimens, however, the residual shear strength was in most cases lower than that for a comparable interface without cyclic loading. This indicates that there was progressive fatigue damage in the adhesive. Assuming that the metal asperities are in contact, at least in the interfaces with high clamping load, intermetallic welding can also occur in the bonded interfaces. In the bonded specimens of the current study, the progressive damage of the adhesive seems to have had a stronger effect on the decrease of the static shear strength than the intermetallic welding had on its increase.

Table 13. Results of static fracture tests after some of the run-out fatigue tests on grit-blasted specimens.

Grit-blasted bonded specimens

Specimen	τ_{II}^{res} [MPa]	τ_{II}^{res} / τ_{II}^{p}
g50_4	56	0.92
g100_3	52	0.72
g100_4	55	0.76
g150_1	96	0.98
g150_2	87	0.89
g150_3	83	0.85
g150_4	92	0.94

Grit-blasted, non-bonded specimens

Specimen	τ_{II}^{res} [MPa]	τ_{II}^{res} / τ_{II}^{p}
g50_1_nb	20	1.33
g100_3_nb	40	1.21
g150_1_nb	86	1.76
g150_2_nb	93	1.90
g150_4_nb	75	1.53

Table 14. Results of static fracture tests after some of the run-out fatigue tests on fine-ground specimens.

Fine-ground, non-bonded specimens		
Specimen	τ_{II}^{res} [MPa]	$\tau_{II}^{res} / \tau_{II}^{p}$
f100_1_nb	33	2.06
f100_2_nb	43	2.67
f100_3_nb	51	3.19

Table 15. Results of static fracture tests after some of the run-out fatigue tests on coarse-ground specimens.

Coarse-ground, bonded specimens		
Specimen	τ_{II}^{res} [MPa]	$\tau_{II}^{res} / \tau_{II}^{p}$
c100_1	49	0.73
c100_2	48	0.72
c100_3	48	0.72
c100_4	53	0.79
c100_6	54	0.81
c150_2	78	1.04
c150_3	88	1.17
Coarse-ground, non-bonded specimens		
Specimen	τ_{II}^{res} [MPa]	$\tau_{II}^{res} / \tau_{II}^{p}$
c100_1_nb	44	2.20
c100_3_nb	46	2.30
c150_1_nb	57	2.04
c150_2_nb	74	2.64

The intermetallic welding seems to be strongest in the fine-ground interfaces and weakest in the grit-blasted interfaces. The fine-ground interface with the smoothest surface finish enables more surface area to come into contact and for this reason, the intermetallic welding is more pronounced.

4.4.3 Threshold relative displacement

It was found that the interfaces had a threshold relative displacement, δ_a^{th}, corresponding to the measured relative displacement at $N = 2\text{x}10^5$ cycles below which the fatigue test always resulted in a run-out. The relative displacements measured at $N = 2\text{x}10^5$ and $N = 1\text{x}10^6$ are tabulated in Appendix A. The threshold relative displacement values for each clamping stress and surface treatment condition are shown in Table 16.

Table 16. Threshold relative displacement amplitudes, δ_a^{th}, observed from the constant amplitude fatigue test data.

q [MPa]	Surface type					
	Grit-blasted, bonded	Grit-blasted, non-bonded	Fine-ground, bonded	Fine-ground, non-bonded	Coarse-ground, bonded	Coarse-ground, non-bonded
4	14 μm					
50	9 μm	60 μm	43 μm	73 μm	10 μm	
100	35 μm	37 μm	58 μm	39 μm	33 μm	32 μm
150	51 μm	43 μm	43 μm	52 μm	41 μm	44 μm

For high clamping stresses (q = 100 MPa and q = 150 MPa), δ_a^{th} is almost identical for the bonded and non-bonded specimens with the same surface roughness. These specimens mainly failed by fretting fatigue. The δ_a^{th} for bonded specimens with low clamping stresses (q = 4 and q = 50 MPa) was, however, much lower than δ_a^{th} for non-bonded specimens. The bonded specimens under low clamping never failed by fretting fatigue, but by shear decohesion. For the high clamping stresses (q = 100 MPa and q = 150 MPa), both the fatigue strength and the δ_a^{th} are approximately the same for bonded and non-bonded interfaces. This seems to confirm that from a fatigue point of view, rough, clamped and bonded surfaces are essentially the same as rough, clamped, non-bonded surfaces. The fatigue behaviour of the mildly-clamped interfaces, on the other hand, seems to be governed by the fatigue failure of the adhesive. Considering the hybrid joint, where both low and high clamping stresses exist depending on the distance from the bolt, the overall slipping might be significantly reduced at the mildly-clamped areas, thanks to bonding. By constraining slip at a distance from the bolt, the adhesive might prevent excessive slip at the highly-clamped areas near the bolts, thus preventing fretting fatigue in the critical locations.

4.5 Fatigue strength of the double lap joint specimen

4.5.1 Preliminary quasi-static tests

Quasi-static tests were performed on the double lap joint specimens with bonded/bolted and plain bolted conditions. The load – displacement curves are shown in Fig. 27. The maximum load for the bonded/bolted joint was 163 kN and 31 kN for the plain bolted joint.

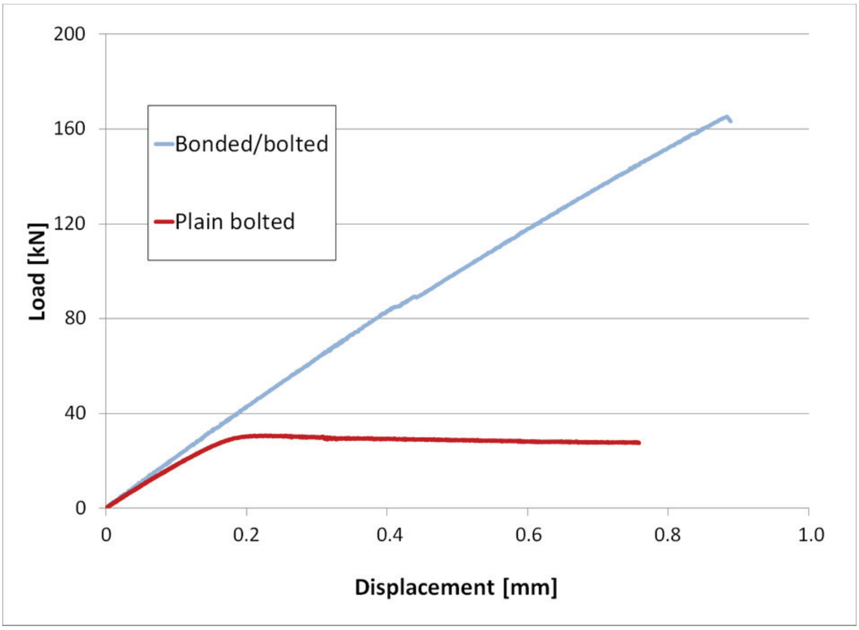

Figure 27. Quasi-static load-displacement response of the bonded/bolted and plain bolted double lap joints.

As can be seen in Fig. 27, both joints initially behave approximately linearly. This is due to elastic elongation of the steel specimen. The bonded/bolted joint fails abruptly after the critical loading has been reached. At this point all the bonded interfaces start slipping and fracture of the adhesive in one of the bonded interfaces leads to practically simultaneous fracture of the other adhesive interfaces so that it is difficult to recognise the original location of failure. In this case there is so much elastic energy stored in the specimen that gradual sliding is not observed. In the bolted joint without adhesive the load is carried by friction and steady sliding begins once the loading exceeds the static frictional strength.

4.5.2 Experimental estimation of fatigue strength

Based on the fatigue tests on the non-bonded napkin ring specimen (Hurme and Marquis, 2013), the fatigue strength of the bolted specimen without adhesive should be in the same range as the static strength. One fatigue test was performed on a bolted specimen without adhesive at the load amplitude of $F_a = 25$ kN. It was a run-out, which implies that the fatigue strength of the plain bolted specimen is indeed close to the static strength for the plain bolted specimen. However, the strength of the bolted joint without adhesive was so low, in comparison to the bonded/bolted joint, that it was decided to focus on the bonded/bolted joints only in the following fatigue strength study. The small sample staircase methodology was used for obtaining an estimate of the mean fatigue strength of the DLJ at $2x10^6$ cycles. The range of experiments using the staircase series is provided in Table 3.

From the results in Table 3, the sequence for the staircase analysis becomes OXXXO, with 80 kN as the starting load level, X_0. The loading interval is $d = 5$ kN and the parameter $k = -0.48$ (corresponding to the series OXXXO) is found from tables in Little (1974). The estimate for the mean of the fatigue strength is calculated from Eq. (1), and it is found to be: $F_{a,f}$ = 77.6 kN.

It is interesting to compare the fatigue strength of the bonded and bolted joint to the fatigue strength of a welded joint with a similar structural geometry. According to the International Institute of Welding recommendations, the FAT class of the transverse-loaded, fillet weld lap joint is 63 MPa, if the failure occurs in the parent metal at the weld toe (Hobbacher, 2009). The FAT class corresponds to the allowable range of stress on the structural detail at 2x10^6 cycles and 95% probability of survival. The fatigue strength would be much less if the weld is undersized so that failure occurs at the weld root. A simple estimate of the mean fatigue strength can be obtained by multiplying the FAT class by 1.5. Because the test specimens are relatively small and because the fatigue testing for completely-reversed loading (R = -1) is of interest, an additional stress ratio enhancement factor of 1.6 can be assumed (Hobbacher, 2009). Thus, without any post-weld improvement, the mean fatigue strength of the welded lap joint based on the nominal stress range in the main plate would be estimated as 151.2 MPa (= 63 MPa *1.5*1.6). This corresponds to the load amplitude of 43.5 kN for the dimensions of the current specimen. Thus, the hybrid joining technology is computed to provide 78.4% (= [77.6 kN/43.5kN] – 1) greater fatigue strength than the corresponding welded joint. This clearly provides potential for fatigue strength improvement as compared to welded joints.

4.5.3 Fatigue strength estimation using finite elements

The fracture of the DLJ is governed by interface shear strength. Consequently, the stresses at the cohesive interface were solved using the finite element method. At first, the analysis was run with a remote loading of P = ±139 MPa which corresponds to the loading amplitude of F_a = 80 kN in the DLJ specimen. The applied loading is slightly higher than the measured fatigue strength of the double lap joint. The purpose of the first simulation is to locate the maxima of the shear stresses and to obtain the approximate values of contact pressure in the locations of maximum shear stress. After that, the shear stress – contact pressure condition is compared to the fatigue strength results of the modified napkin ring specimens (Table 11). In subsequent simulations, the applied loading is changed so that the maximum shear stress corresponds to the interface fatigue strength measured from the modified napkin ring tests. As a result, an estimate of the fatigue strength of the double lap joint is obtained.

The surface output variables, CPRESS and CSHEAR, provided the contact pressure and contact shear traction components, respectively. The contact shear stress distribution, τ_1, along the local 1-direction at remote loading $P = P_{\max}$ = 139 MPa and $P = P_{\min}$ = -139 MPa in step 2 is provided in Figs. 28 a and b, respectively, and the contact pressure distribution, σ_2, at $P = P_{\max}$ and $P = P_{\min}$ can be seen in Figs. 28 c and d, respectively. Only the contact surface is plotted. The severity of the stresses is highest in the regions coloured with dark red and lowest in the light-coloured areas.

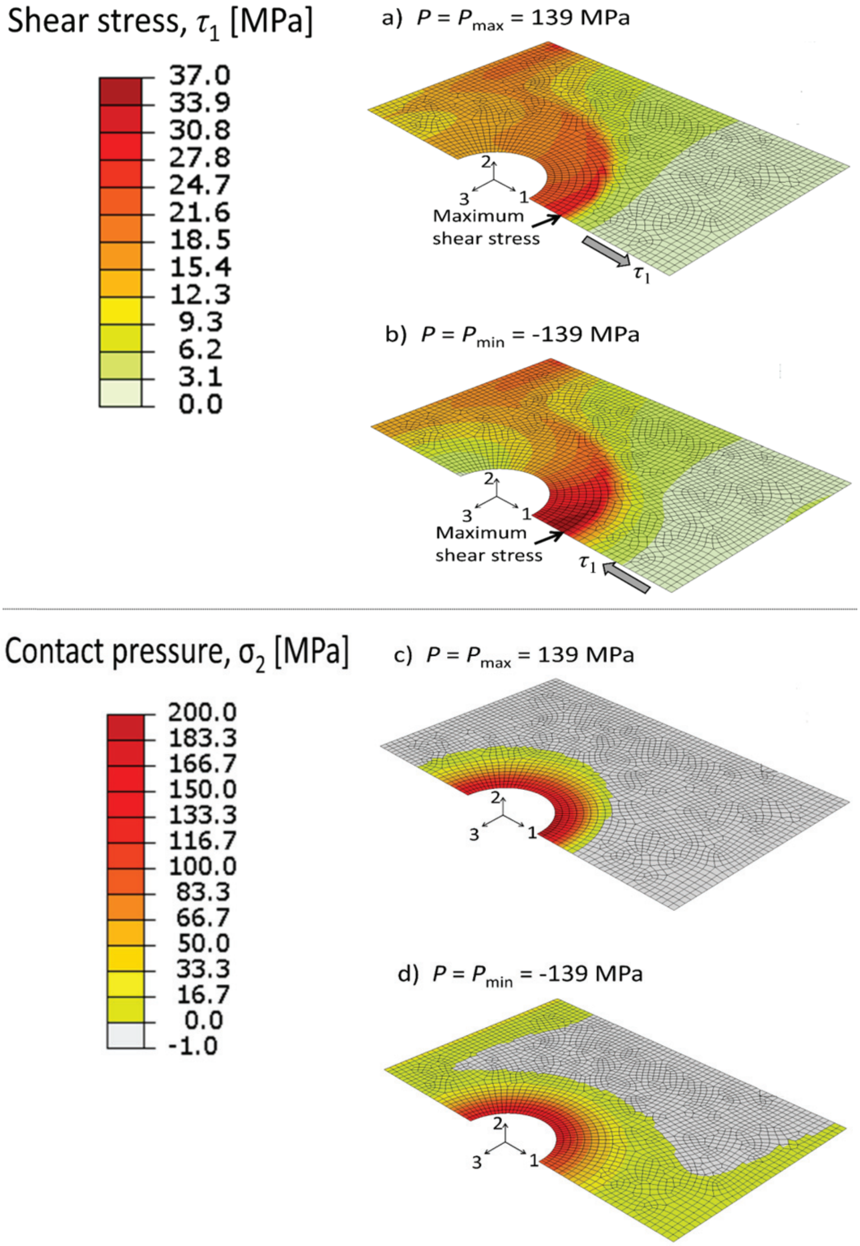

Figure 28. The interface stress distribution. a) Shear stress in the local 1-direction at $P = P_{\max}$, b) shear stress in the local 1-direction at $P = P_{\min}$, c) contact pressure at $P = P_{\max}$ and d) contact pressure at $P = P_{\min}$. Locations of the maximum shear stresses are indicated.

In the transversal direction, the shear stresses were much lower and thus, the failure was governed by the shear stress in the direction of the applied remote load. The maximum shear stresses occurred in the locations shown by the arrows in Figs. 28 a and b. The maximum shear stress occurred at a distance of approximately 6 mm from the edge of the bolt hole, next to the centre line. At $P = P_{\max}$, the contact pressure at the location of maximum shear stress is $\sigma_2 =$ 9 MPa. At $P = P_{\min}$, the contact pressure is $\sigma_2 =$ 55 MPa. The contact pressures were obtained using the bolt load of 21500 N.

The shear fatigue strength of the bonded and clamped interface, obtained experimentally using the modified napkin ring specimen, was found to be $\tau_f =$ 19 MPa under q = 50 MPa clamping, and under q = 4 MPa, the fatigue strength was $\tau_f =$ 21 MPa (Hurme and Marquis, 2013). As a next step, the model is used to find a remote loading that creates shear stresses which do not exceed the fatigue strength. The maximum traction of $\tau_1 =$ 19 MPa is found to occur with the remote loading of $P_{\max} = -P_{\min} =$ 107 MPa. This corresponds to the loading amplitude of $F_a =$ 61.6 kN in the full double lap joint. Experimentally, the fatigue strength of the DLJ was found to be $F_{a,f} =$ 77.6 kN. Thus, the simulation provides conservative results, as expected.

The simulations show that the contact pressure in the interface changes with loading. However, the interface fatigue strength results, obtained using the modified napkin ring specimen, correspond to constant contact pressure. As a result, the method presented in this thesis is not able to account for the effect of the fluctuating contact pressure on fatigue behaviour. In the above case, the contact pressure varied between 9 MPa and 55 MPa. The interface fatigue strength values in this range of contact pressure appear to be very similar, as can be seen in Table 11. Consequently, it can be deduced that the impact of the fluctuation of contact pressure is not very high in this case. However, it possibly becomes significant if fretting fatigue crack propagation has to be assessed. Clearly, this is a topic which requires further examination.

It should be recalled that the critical traction in the positive normal direction was set to $t_n^0 =1$ MPa, since the contribution of positive normal tractions to fatigue strength was assumed to be negligible. This assumption was clearly conservative. However, in the absence of better understanding, it was considered to be a prudent assumption. The tensile normal stress in the DLJ is caused by shear lag, i.e., the cover plates tend to bend away from the main plate as stress is applied to the main plate. The highly-exaggerated deformations of the DLJ model are shown in Fig. 29. Cohesive damage occurs in the integration points in the area under positive normal stress during the loading up to $P_{\max}$ because of the assumption $t_n^0 =1$ MPa.

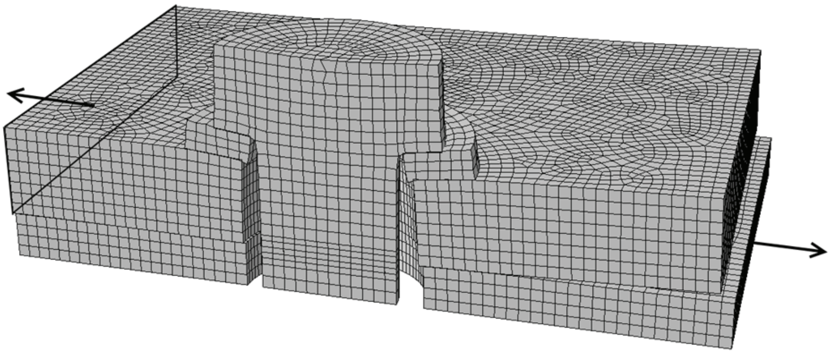

Figure 29. Exaggerated deformations of the DLJ model showing the shear lag effect.

The amount of interface damage at $P = P_{\max}$ when $P_{\max}$ =139 MPa can be observed in Fig. 30.

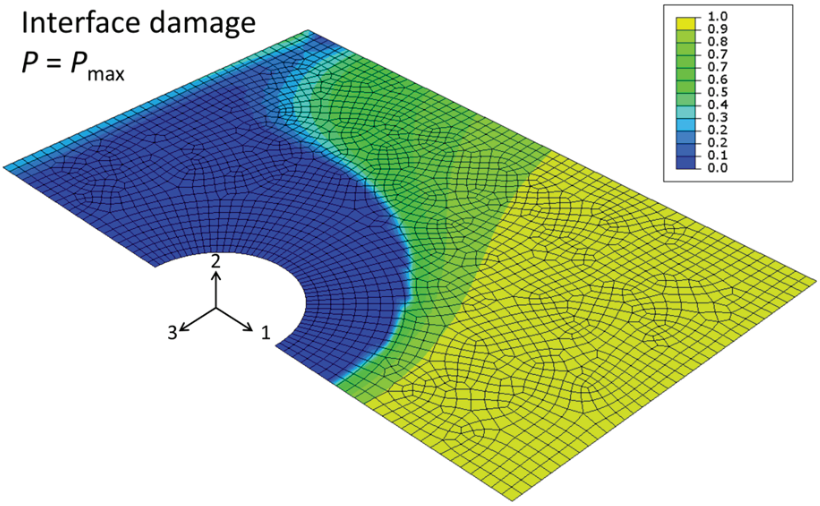

Figure 30. Value of the damage variable according to Eq. (6) at $P = P_{\max}$ when $P_{\max}$ =139 MPa. Yellow indicates almost total damage and blue indicates almost zero damage

Damage is nearly total in the yellow-coloured areas in Fig. 30, while the blue-coloured area is not damaged at all. The direct result of the assumption that critical normal traction is small is that load is carried mainly by the area under compressive normal stress around the bolt hole, and the area near the middle of the specimen where normal stress is low. When comparing Figs. 20, 21 and 30, it can be seen that the area with fretting damage is located approximately at the line between the areas of damaged adhesive and undamaged adhesive, according to the simulation. Fig. 28 reveals that the maximum traction occurs at the edge of the area under compression. This is the edge of sticking contact, where the contact status changes between slipping and sticking during cyclic loading and, consequently, where fretting fatigue cracks are initiated. However, the clamping stress at the location of maximum traction is only 9 to 55 MPa, which should result in shear decohesion failure according to Hurme and Marquis (2013). Under low clamping stress, fretting does not necessarily lead to crack initiation but can cause damage to the interface, as was observed in the DLJ specimens.

Discussion

The quasi-static tests with the bonded/bolted and plain bolted double lap joints reveal that the bonded/bolted joint is significantly stronger. In order to benefit from the design of a hybrid joint, the joint should not simply be designed as a plain bolted joint with adhesive added later for some extra strength. The combination of bolt and adhesive clearly provides considerable potential for strength increase, or weight-saving by the reduction of the number of bolts, as compared to the plain bolted joint. Most importantly, it was shown that a bonded/bolted hybrid joint had much better fatigue strength than a welded joint with the same structural geometry. The results also imply that the plain bonded joint was weaker than the combined bonded/bolted joint, but this would require further proof as there are also contradicting reports in the literature (Hart-Smith, 1985).

The fatigue strength estimate for the DLJ obtained by finite element method was conservative, as expected. In section 3.2.3 the observation was reported that the calculated interface shear stresses have a strong dependence on the cohesive stiffness, i.e., the choice of the stiffness will have an effect on the fatigue strength estimate. The stiffness was determined from on a number of quasi-static experiments on the modified napkin ring specimen using careful consideration. However, in reality, the interface stiffness has a statistical distribution, which was not accounted for in the presented analysis. The determination of this distribution would be necessary for reliable design in the future.

The analysis presented in this paper shows the critical locations in the interface where fatigue failure is concerned. It can also be used to estimate whether or not the interface will fail before $N = 2\text{x}10^6$ cycles under fatigue loading. However, no estimation of fatigue life can be carried out. A more detailed analysis of the interface fatigue failure would require a progressive fatigue damage model of the adhesive, combined with fretting fatigue analysis.

4.6 Fatigue damage assessment

For more detailed analysis of the fatigue behaviour of the hybrid joint, a progressive fatigue damage model of the adhesive is required. This is approached by deriving a fatigue damage model from the low-cycle fatigue experiments on the modified napkin ring specimen. The damage parameter will be related to the observed change in specimen compliance, and the physical nature of the crack distribution in the damaged material will be discussed. In addition to the fatigue damage model, the cohesive zone model described in Section 3.2.1 is re-formulated with fatigue damage, in order to assess the residual strength of the interface during fatigue loading.

Throughout this thesis, different observations have been reported concerning the failure mechanisms in the bonded and clamped interface. Based on these observations, the following assumptions and conclusions are made, on which the progressive fatigue damage model will be founded:

1. Based on the results and discussion on the SEM analysis of damaged adhesive, it was concluded that static and fatigue damage are controlled by two physically different processes. For this reason, they are given separate variables in the following formulation.
2. The fatigue damage was found to be composed of several small cracks with different lengths and orientations. Accordingly, the damage is understood as a set of cracks with a suitable distribution of crack lengths.
3. The fatigue damage observed by SEM was composed of small cracks, which did not extend through the interface. Thus, they do not enable contact between the asperities of the surface roughness of the metal adherends. As a result, the friction is not considered to have an effect before the initiation of static damage, which is assumed to cause cracks to propagate through the thickness of the adhesive layer.
4. As a result of the previous point, the fatigue damage is assumed to progress in the adhesive regardless of the clamping stress. Therefore, the friction will only play a role in the residual strength of the interface, which shall be determined through cohesive zone modelling.

The approach of separation of the static and fatigue damage variables has been adopted in most of the studies concerning cohesive zone modelling with fatigue damage (Roe and Siegmund, 2003; Khoramishad et al., 2010; Robinson et al., 2005; Turon et al., 2007; Harper and Hallett, 2010; Landry and LaPlante, 2012; Naghipour et al., 2011; May and Hallett, 2010, 2011; Muñoz et al., 2006). However, the physical motivation for this, as well as many other assumptions related to cohesive zone modelling, has been unclear throughout the development of the cohesive zone modelling technique (Pascoe et al., 2013). As discussed in section 4.1.2, the SEM study was not performed for the specimens during quasi-static loading. This examination would be important to fully justify the assumption that different damage parameters are adopted for fatigue and static loading and it should be a topic of future research.

The assumption that in a bonded interface with friction, the stresses are initially fully carried by the cohesive forces and frictional forces are added only after damage initiates, has been adopted earlier by other researchers (Alfano and Sacco, 2006; Parrinello et al., 2009; Sacco and Lebon, 2012). These studies were focused on static fracture: a literature review did not reveal any proposals concerning the incorporation of frictional effects during the fatigue damage process of cohesive interfaces. The assumption that friction is not effective during the evolution of fatigue damage, if static damage has not initiated, is considred to be an original proposal in this thesis.

The fourth listed point leads to the conclusion that the same progressive damage model and cohesive zone model formulated for fatigue damage can be used for modelling the adhesive in interfaces under any clamping stress. The difference in the residual strength of the interface comes simply from the effect of friction, which is added to the cohesive traction in proportion to quasi-static damage. If this holds, the same model could be used for describing the entire hybrid joint, including the interfaces under high clamping stress. However, this could not be explicitly confirmed with the current test set-up, as the cyclic load-carrying capacity of friction in the specimens with high clamping stress greatly exceeds the cyclic load-carrying capacity of the adhesive. Thus, it is difficult to distinguish the mechanism currently carrying the load in specimens with high clamping stress by simply measuring the relative displacement. The applicability of the proposed method on interfaces with very high clamping stress should be a subject of further study.

During a modified napkin ring fatigue test, the shear stress amplitude is held constant and the relative displacement of the specimen pairs is measured. A typical displacement amplitude history during a fatigue test is provided in Fig. 31.

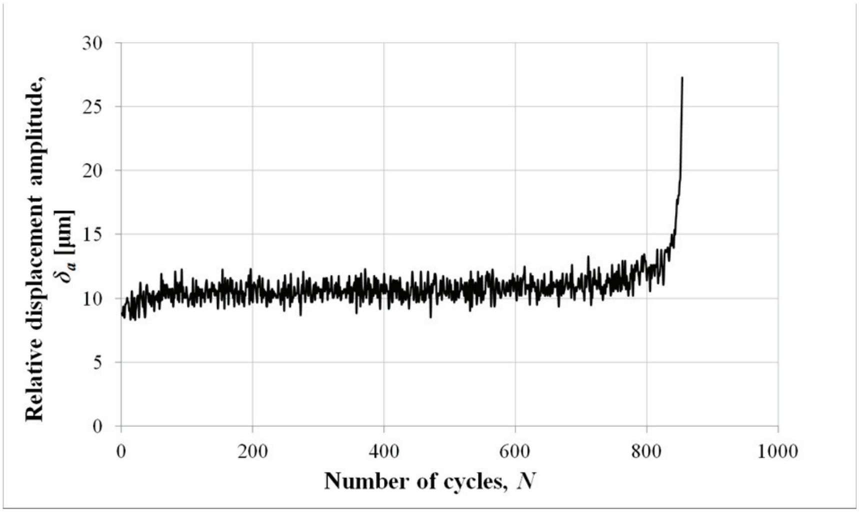

Figure 31. Relative displacement amplitude during fatigue test F1 (Table 1).

Due to fatigue damage, the compliance of the napkin ring specimen increases with the number of cycles, as can be seen from Fig. 31. Therefore, the evolution of the fatigue damage parameter can be related to the change in the compliance. The interface stiffness is related to the fatigue damage parameter, D_f, through

$$\kappa = (1 - D_f)\kappa_0 \qquad (9)$$

4.6.1 The damage evolution equation

As can be seen in Fig. 18, the damage in the adhesive consists of several microcracks with different lengths and orientations. Even though the damage consists of cracks with different lengths, all existing cracks are small and must be assessed based on methods for small fatigue crack growth, instead of linear-elastic fracture mechanics (LEFM). Suresh and Ritchie (1984) have suggested the following classification for small cracks:

1. Fatigue cracks of a size comparable to the characteristic microstructural dimension of the material, such as grain size or interparticular spacing for particulate-reinforced composites, are referred to as *microstructurally small* cracks.
2. Cracks, for which the near-tip plasticity is comparable to the crack size, or cracks that are engulfed by the plastic strain field of a notch, are called *mechanically small* cracks.
3. Fatigue cracks which are significantly larger than the characteristic microstructural dimension or the scale of local plasticity, but are small in size, typically less than a millimetre or two, are considered to be *physically small.*
4. Sometimes flaws which are otherwise applicable to LEFM, but exhibit anomalies in propagation rate below a certain crack size as a consequence of environmental stress corrosion are referred to as *chemically small* cracks.

The epoxy adhesive has an overall amorphous microstructure, i.e., the material is in the glassy state without grain structure. As a consequence, the characteristic microstructural dimension can be considered to be the interface thickness. As the crack lengths are comparable to the thickness, the cracks can be characterised as microstructurally small.

The studies of crack growth behaviour in adhesives are limited, as compared to the number of studies in metallic materials. Furthermore, no studies on small crack growth in adhesives were found. Usually, the fracture mechanics approaches in adhesives employ the same concepts as are used in metallic materials, namely the Paris equation (Paris et al., 1961) for fatigue crack growth. Consequently, it is acceptable to assume that small crack growth in adhesive materials follows similar laws as that in metallic materials.

The growth of small cracks differs from the growth of long cracks, in that the same stress intensity factor results in much faster crack growth, and the crack growth rate is not explicitly proportional to the stress intensity factor (Pearson, 1975). When small cracks propagate at a finite rate, the small- scale yielding condition at the crack tip is not satisfied. Instead of the Paris equation, the crack growth rate for small cracks has been determined by several researchers (Murakami and Miller, 2005; Nisitani et al., 1992; Goto et al., 2013) by the equation

$$\frac{da}{dN} = B_1 {\sigma_a}^{m_1} a \tag{10}$$

where da/dN is the crack growth rate, B_1 and m_1 are material constants, σ_a is the nominal stress amplitude and a is the crack length. The exponent, m_1, takes a value much larger than 2. Murakami and Miller (2005) discussed the essence of fatigue damage which in their work was identified as the crack length, whereas in this study it is some set of cracks in the adhesive material causing a change in compliance.

The cracks in the adhesive grow under nominal shear stress. However, based on a review of the literature, adequate data of small crack growth under shear stress are not available. Therefore, in the absence of sufficient information it is assumed that the same form of the small crack growth equation also applies under shear stress

$$\frac{da}{dN} = B_2 \tau_a^{m_2} a \tag{11}$$

where τ_a is the shear stress amplitude and B_2 and m_2 are material constants under shear stress conditions.

The damage consists of small cracks, which makes it logical to assume that the damage evolution equation is of a similar type as the small crack growth equation. However, the damage involves several small cracks with different lengths and orientations. The mechanism of interaction of these cracks is not fully understood in the theory of fracture mechanics. Therefore, the relation of the damage growth rate and the damage is not necessarily linear. The damage growth rate is assumed to be related to the fatigue damage as

$$\frac{dD_f}{dN} = B \tau_a^{m} D_f^{\gamma} \tag{12}$$

where B, m, and γ are fitting constants. The units of B depend on the exponent m so that $[B]$ = MPa^{-m}. The exponent, m, can be considered equivalent to the exponent of the small crack growth equation.

Fitting to experimental data

The ratio of the load amplitude and the measured relative displacement directly gives the reduced interfacial stiffness and thus, the fatigue damage parameter

$$(1 - D_f)\kappa_0 = \tau_a / \delta_a \tag{13}$$

It should be noted, that during fatigue tests, the threshold to quasi-static damage initiation is not exceeded and, consequently, the fatigue damage in the material is equivalent to the total damage. The initial stiffness, κ_0, is taken as the average of the first 10 loading cycles. During the tests, the data were collected at pre-defined intervals, ΔN. For analysis, the data should be given at pre-defined intervals, ΔD_f. The analysis of the $D_f - N$ data points can be performed following the data compression scheme published by Marquis (1992). Numerous measured $D_f - N$ data pairs are thereby compressed into one $\hat{D}_f - N$ estimate data pair, with a spacing of $\Delta\hat{D}_f = 10S$, where S is the measurement precision. Since the report (Marquis, 1992) is not widely available, a detailed description of the methodology is provided in Appendix D.

The damage growth curves for all specimens in Tables 1 and 2 are plotted in Fig. 32 with the normalised number of cycles on the horizontal axis. The specimens in Table 2 are interrupted fatigue tests for which the number of cycles to final failure, N_f, is not known. However, all of the interrupted fatigue tests were halted when a pre-defined amount of computed damage (change in compliance) was observed. From Fig. 31, it can be seen that the observable change in compliance occurs during the very last cycles that the specimen can sustain before full fracture. Therefore, taking the last cycle in the interrupted fatigue test as N_f, produces only minimal error in Fig. 32.

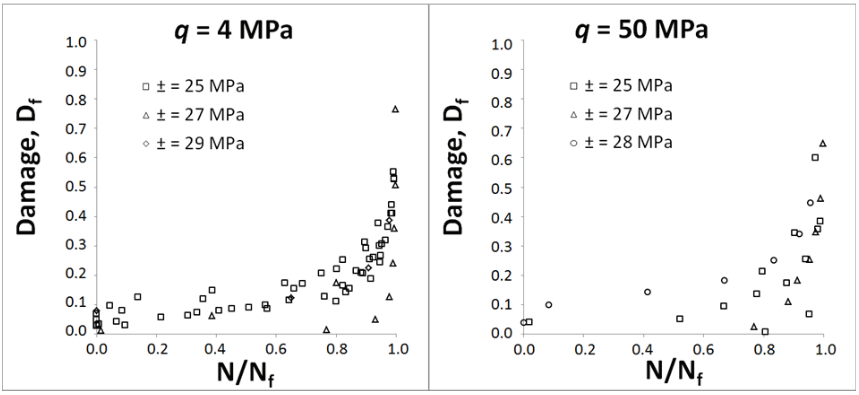

Figure 32. Damage growth curves for the specimens with the two clamping stresses.

The data pairs, $\hat{D}_f - N$, are used to calculate the rate of increase of the damage, dD_f / dN, using the secant method. The equation for damage growth rate, Eq. (12), has three parameters that must be found by fitting from the data. Firstly, an estimate of the stress amplitude exponent, m, is obtained by plotting the damage growth rate vs. the shear stress amplitude on a log-log graph for different values of damage (Fig. 33). The exponent, m, is obtained from the power-law fit into the data. A limited number of experiments were performed with shear stress amplitudes other than τ_a = 25 MPa and, consequently, only a crude estimation of the shear stress exponent can be made. In this assessment, the value for the exponent is chosen to be m = 8.6, however, further inverstigations are clearly needed to accurately estimate the exponent.

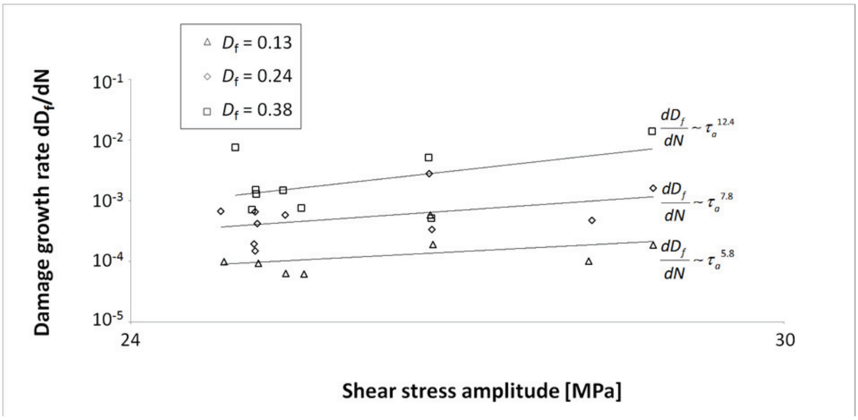

Figure 33. Damage growth rate vs. shear stress amplitude at three different values of damage for all specimens in Tables 1 and 2.

In order to estimate the remaining parameters, B and γ, of Eq. (12), the dD_f / dN is plotted on a log-log graph against the value of $\tau_a{}^m D_f{}^\gamma$, where D_f is the average fatigue damage in the interval, and Eq. (12) is fitted to the data points.

The data are shown in Fig. 34 for both clamping stresses, q = 4 MPa and q = 50 MPa. The constant, γ, is chosen so that the log-log plot of dD_f / dN vs. $\tau_a{}^m D_f{}^\gamma$ has the slope of 1. The values of the constant, γ, were found to be γ = 2.22 for the q = 4 MPa specimens and γ = 1.42 for the q = 50 MPa specimens. The constant B is obtained from the fit and has the value $B = 9 \times 10^{-15}$ for the q = 4 MPa specimens and $B = 2 \times 10^{-15}$ for the q = 50 MPa specimens.

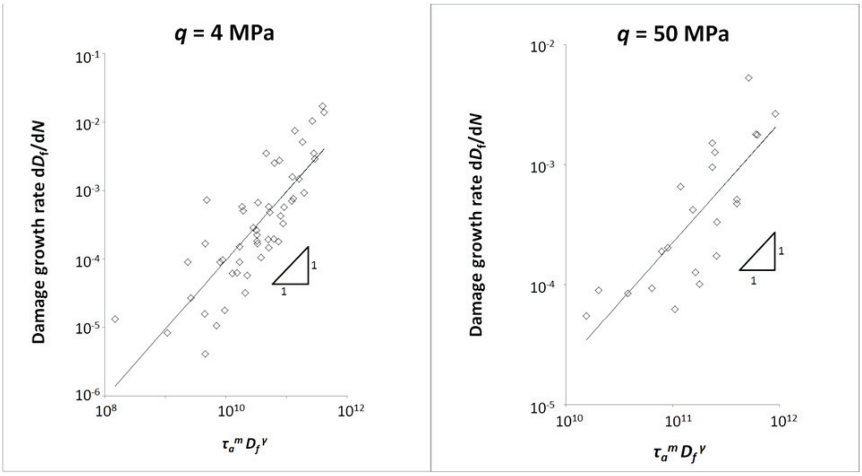

Figure 34. Fitting of the damage growth rate equation for the two clamping stresses, q = 4 MPa and q = 50 MPa.

The coefficients for the damage evolution equation of the two cases are different, although the initial assumption was that friction does not have a role in fatigue damage evolution. On the other hand, it is possible that the assumption that friction has no effect before quasi-static damage initiates could be erroneous. In order to confirm the assumption, further research is needed. However, the difference in the two cases is small and could also fall within the scatter of the experimental results. Therefore, the proposed analysis can be used at least for initial assessments.

4.6.2 Interrupted fatigue tests

A series of interrupted fatigue tests (see Table 2) was performed in which the fatigue test continued until a pre-defined damage state had been attained, then the fatigue test was followed by a quasi-static fracture test. The shear stress – relative displacement response of the specimens after the interrupted fatigue tests are shown in Figs. 35 a and b for the clamping stresses q = 4 MPa and q = 50 MPa, respectively. Static fracture measurements of undamaged specimens for both clamping stresses are also provided for reference. After attainment of the critical shear stress, the fracture was rapid, so sufficient data points could not be collected.

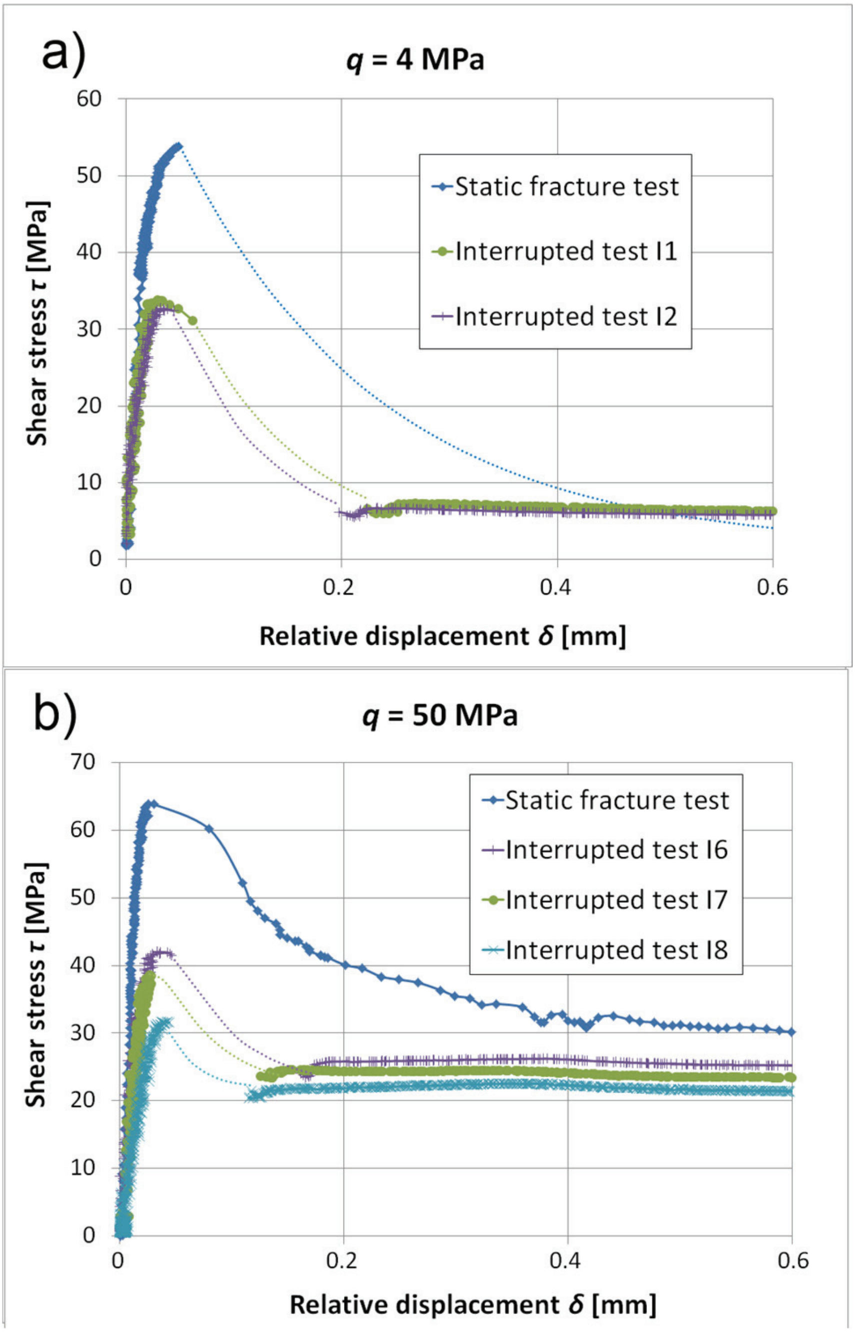

Figure 35. Quasi-static fracture response after the interrupted fatigue tests for specimens with the (a) q = 4 MPa clamping and (b) q = 50 MPa clamping.

4.6.3 Cohesive zone model formulated for fatigue damage

The cohesive zone modelling is used to assess the residual strength of the interface with accumulated fatigue damage. The CZM without fatigue damage was formulated for the idealised clamped and bonded interface in section 3.2.

The fatigue damage evolution model is based on experimental results from the modified napkin ring specimen. As the experimental data give information only about the mode II fatigue behaviour, mode I is neglected in the following formulation. Mode III is considered to be equivalent to mode II. In this framework, some of the parameters described in section 3.2.1 will be redefined to account for mode II only. Namely, the effective separation, Eq. (5); the traction vector, Eq. (2); and the quasi-static damage variable, Eq. (6); become

$$\begin{aligned} &\delta_m = \delta_s = \delta, \\ &\mathbf{t} = t_s = \kappa_{ss}\delta_s = \kappa\delta, \qquad , \\ &D_s = 1 - \left\{\frac{\delta^0}{\delta}\right\}\left\{1 - \frac{1-\exp(-\alpha(\frac{\delta-\delta^0}{\delta^f-\delta^0}))}{1-\exp(-\alpha)}\right\} \end{aligned} \tag{14}$$

respectively. The scalar damage parameter will be denoted as D_s, which describes mode II damage under quasi-static loading.

The total damage in the adhesive material is composed of both the quasi-static damage parameter, D_s, and the fatigue damage parameter, D_f, so that

$$(1-D_{tot}) = (1-D_f)(1-D_s) \tag{15}$$

The fatigue damage is observed as change in compliance during cyclic loading and quasi-static damage is observed as decrease in interface traction with increasing separation when the critical relative displacement, δ^0, has been exceeded. As long as the critical relative displacement is not exceeded, the damage is considered to be composed solely of fatigue damage, as explained earlier.

The effect of fatigue damage on the cohesive law is illustrated in Fig. 36. During a fatigue test, the loading remains in the elastic regime and the compliance increases continuously due to an increase in fatigue damage. Thus. the properties of the cohesive zone model must be changed according to the fatigue damage parameter.

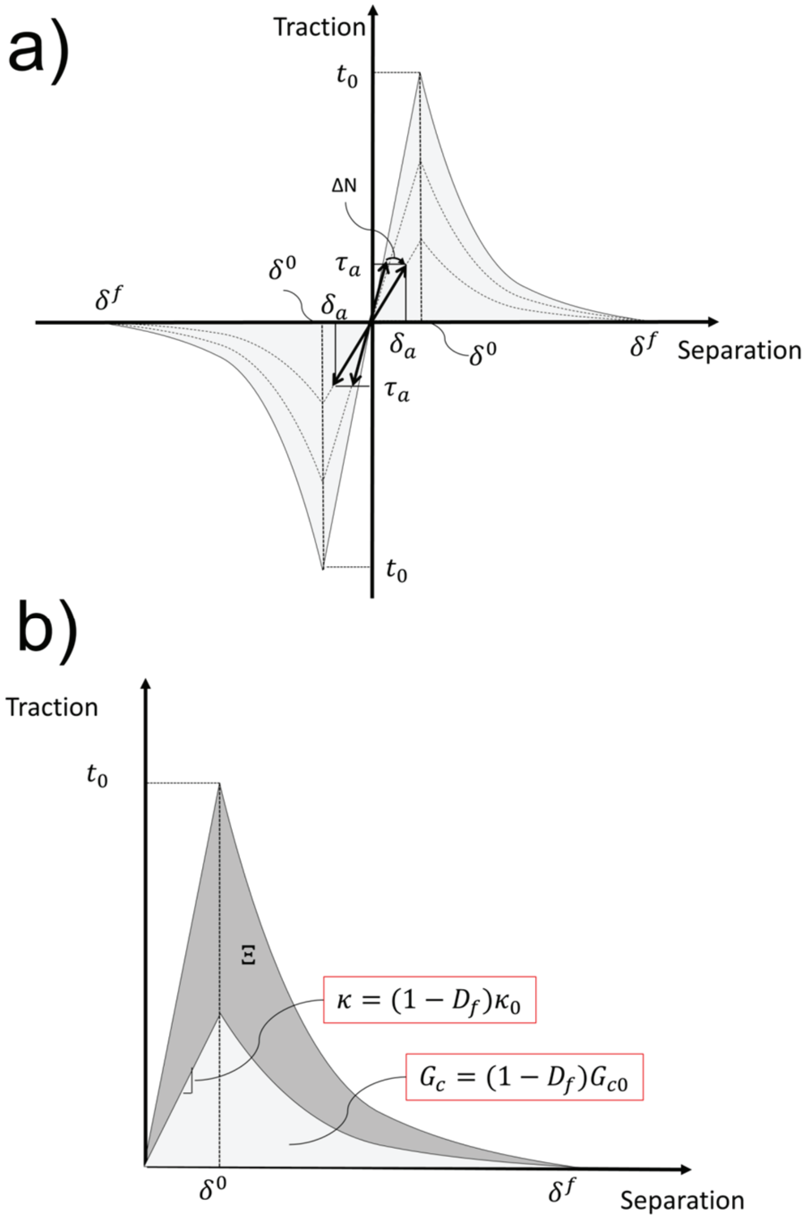

Figure 36. a) Degradation of the cohesive zone constitutive law due to fatigue loading. The applied shear stress amplitude, τ_a, is constant, and the relative displacement amplitude δ_a is measured for every cycle, *N*. b) The cohesive law with fatigue damage, D_f. The remaining fracture energy, G_c, is defined as the area under the cohesive law with fatigue damage. The energy dissipated due to fatigue damage is indicated by Ξ .

The remaining fracture energy, G_c, is defined as the area under the cohesive law. The energy dissipated due to fatigue damage is indicated by Ξ . The total damage is defined as the ratio of the energy dissipated during the damage process, Ξ, and the initial fracture energy (before fatigue damage), G_{c0} (Turon et al., 2007).

$$D_{tot} = \frac{\Xi}{G_{c0}} \tag{16}$$

The energy dissipated due to damage can be obtained from

$$\Xi = G_{c0} - G_c \tag{17}$$

where the fracture energy, G_c, is calculated from the area under the traction-separation curve of the cohesive zone constitutive model with damage

$$G_c = \int_0^{\delta^f} t(\delta) d\delta \tag{18}$$

During fatigue loading before the initiation of static damage, the total damage is equal to the fatigue damage and the fracture energy can be written as

$$G_c = \frac{1}{2}(1 - D_f)\kappa_0(\delta^0)^2 + \int_{\delta^0}^{\delta^f} (1 - D_f)(1 - D_s)\kappa_0 \delta d\delta \tag{19}$$

or in short:

$$G_c = (1 - D_f) G_{c0} \tag{20}$$

It is assumed that the remaining cohesive law parameters, namely, δ^0 and δ^f, remain unchanged during the fatigue damage evolution. As a result of Eq. (20), the critical shear traction due to fatigue damage becomes

$$t_c = (1 - D_f) t_0 \tag{21}$$

The calculated cohesive response with the corresponding fatigue damage for each interrupted fatigue test is illustrated in Fig. 37 (dashed lines), along with the static fracture test data after the interrupted fatigue tests.

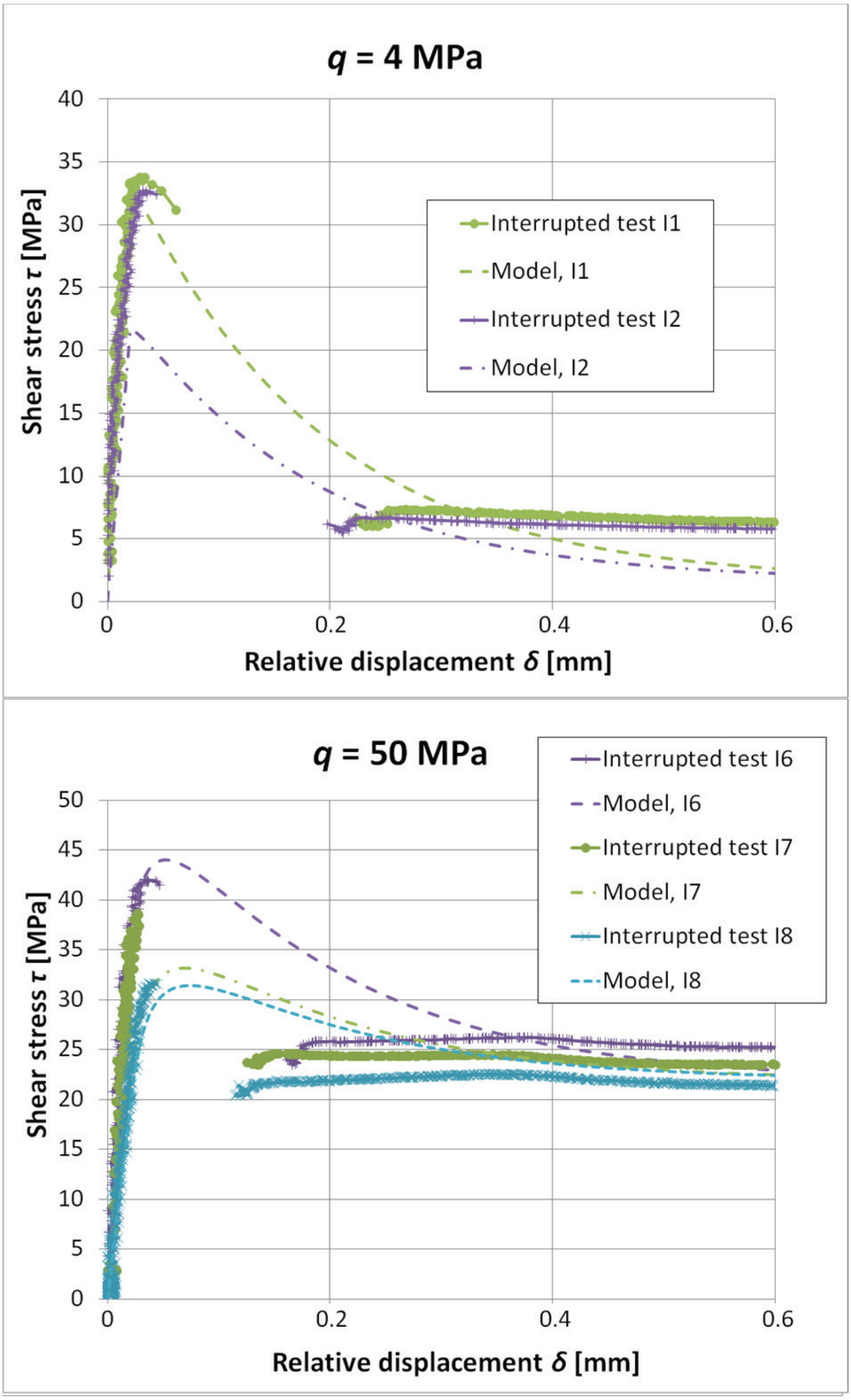

Figure 37. Static fracture data after the interrupted fatigue tests and the cohesive behavior with the corresponding fatigue damage.

The model fits to some of the data sets in Fig. 37 better than to others. This is due to scatter.

It should be noted that the friction is added into the model only after static damage initiates. Thus, the shear stress is not equal to the cohesive traction, but is the sum of cohesive traction and frictional traction, added in proportion to quasi-static damage, as in Eq. (7).

4.6.4 Comparison of modelled and experimental fatigue lives

The estimate of fatigue life for a given loading can be obtained by integrating Eq. (12)

$$\int_{D_0}^{D_c} \frac{1}{B\tau_a{}^m D_f{}^\gamma} dD_f = \int_0^{Nf} dN \tag{22}$$

After some manipulation the expression for fatigue life becomes

$$N_f = \frac{1}{(\gamma-1)B\tau_a{}^m}\left(\frac{1}{D_0{}^{\gamma-1}} - \frac{1}{D_c{}^{\gamma-1}}\right) \tag{23}$$

The critical damage, D_c, occurs when the critical shear traction, Eq. (21), has reduced due to damage so that its value equals the applied shear stress.

$$D_c = 1 - \frac{\tau_a}{t_0} \tag{24}$$

The critical traction, t_o, is given in Table 7. However, it is the value chosen for the initial damage, D_o, which has the most significant impact on the resulting estimate of the fatigue life.

The meaning of initial damage requires further clarification. Equations analogous to Eqs. (22) and (23) are used to estimate the fatigue life based on the growth of a macro-crack, where the crack growth equation is integrated from initial to critical crack length. Therefore, it is important not to confuse the initial and critical damage with the initial and critical crack length. With the growth of a macroscopic fatigue crack, damage, as evidenced by several microcracks, occurs ahead of the crack tip, as demonstrated by Chai (1993b). Consequently, the evolution of damage is a prerequisite for the propagation and initiation of a fatigue macro-crack. Since damage is the phenomenon preceding macro-crack initiation, the initiation of a fatigue crack could potentially be modelled with the proposed approach. In the napkin ring specimen with nominally uniform stress conditions the evolution of damage leads to final failure of the interface without leading to the initiation of one macroscopic fatigue crack, which provides for an interesting opportunity to assess the evolution of damage. However, the assessment does not provide a mechanism for the initiation of damage itself, but some initial damage has to be assumed. Ideally, this could be estimated from the SEM analysis. However, the estimation of the distribution of cracks is not clear from the SEM pictures, and the initial damage will be estimated based on experimental data under the clamping stress q = 4

MPa. There are plenty of fatigue results for specimens under the loading of τ_a = 25 MPa (Tables 1 and 2), and the fatigue lives measured range from approximately N_f = 1,000 to N_f = 10,000 cycles. If the most conservative estimate is chosen, the fatigue life, N_f, corresponding to τ_a = 25 MPa is chosen to be N_f = 1,000. By inserting the values for shear stress amplitude and N_f into Eq. (23), as well as the initial condition when N = 0, the initial damage is found to be D_o = 0.117. For reference, the least conservative estimate is obtained when the initial damage is computed from the measured fatigue life of N_f = 10,000 cycles. In this case the initial damage is D_0 = 0.02.

The low-cycle fatigue test results of specimens in Tables 1 and 2 are plotted on a stress-life graph in Fig. 38, and the fatigue life estimate lines based on the proposed model and the most conservative (Estimate 1) and least conservative (Estimate 2) initial damage are shown for both clamping stresses, q = 4 and q = 50 MPa.

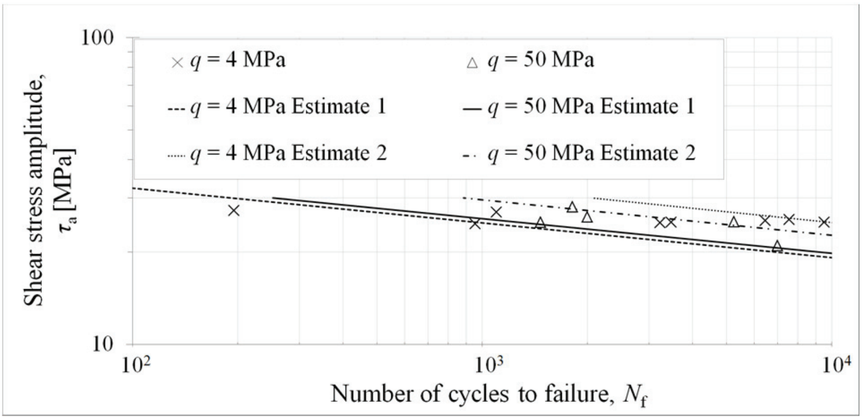

Figure 38. Calculated τ_a vs. N_f lines for both clamping stresses and the most conservative (Estimate 1) and least conservative (Estimate 2) initial damage values, and the constant amplitude fatigue data for the bonded, grit-blasted q = 4 and 50 MPa experiments reported in Tables 1 and 2.

Fig. 38 shows that the low-cycle fatigue stress-life data obtained from the modified napkin ring specimens produce a rather flat line in the stress-life graph. The proposed model is able to capture the fatigue behaviour with reasonable accuracy. It can be seen that the estimates 1 are conservative, i.e. the lines provide a lower boundary for the data points. This is due to the choice of initial damage, D_0, which was calculated from the most conservative measured fatigue life. The estimates 2, on the other hand, provide the upper boundary of the experimental data. The stress-life curve estimates of the two normal pre-stresses are almost overlapping at the conservative estimate, but for the least conservative estimates, the curve for the q = 50 MPa pre-stress yields slightly shorter fatigue lives. The estimates of the fatigue life are sensitive to the choice of the initial damage, and the sensitivity depends on the parameters of Eq. (12). Due to the parameters of Eq (12) derived for the two pre-stresses, the q = 4 MPa pre-stress case is more sensitive to the choice of the initial damage parameter. However, if conservative estimates are used, the sensitivity is not as high. Due to the sensitivity to initial damage, as well as high scatter in the experimental data, the use of conservative estimates of the initial damage are encouraged.

4.6.5 Physical nature of the fatigue damage

The amount of damage can be observed directly from the specimen compliance, but not the length or distribution of cracks which represent the physics of damage. This is shown by a simple reasoning: Let us suppose that the damage is reflected by the total length of cracks. Now, let us consider two cases with equal damage (equal total length of cracks); in the first case, the damage consists of several small cracks with equal length, while in the second case, the damage consists of fewer, but longer cracks with equal length. In both cases, the same compliance is measured but the damage evolution behaviour following subsequent loading cycles is different. According to Eq. (10), the long cracks grow much faster than the short cracks and, as a result, the damage evolution in the case of long cracks will be much faster than in the case of short cracks. Consequently, the entire description of damage cannot be obtained simply by measuring the compliance. Furthermore, it is not realistic to assume that all cracks have equal lengths. In order to understand the damage evolution in the material, the distribution of cracks must be defined. With a distribution of crack lengths, the measured compliance does not reflect the total length of cracks but the longest cracks have the highest influence. The exact length or distribution of the crack lengths is not known. However, it is reasonable to assume that the crack lengths have an exponential distribution, so that the number of shorter cracks is much higher than the number of relatively long cracks. The exponential distribution can be described by

$$F(a) = C_1 e^{-C_2 a} \tag{25}$$

where C_1 and C_2 are constants and a is the crack length.

As fatigue cycles are accumulated, the long cracks extend much faster than short cracks and the cracks coalesce. As a result, the number of short cracks decreases and the number of long cracks increases with growing number of cycles. Therefore, the distribution has to change with the number of cycles, N. In order to change the distribution with the number of cycles, the terms C_1 and C_2 must depend on N. It is assumed that no cracks are initiated during fatigue loading. This is a valid approximation because fatigue damage is represented by the entire set of cracks, where the largest cracks have the highest influence on compliance and residual strength.

The total set of cracks, which is considered as a measure of damage, can be obtained from $F(a)$ by integrating

$$\int_0^\infty F(a)da = \int_0^\infty C_1 e^{-C_2 a} da = \frac{C_1}{C_2} \tag{26}$$

Thus, the fatigue damage, calculated from the changes in compliance, is related to the total set of cracks by

$$D_f = \frac{C_1}{C_2} \tag{27}$$

The crack distribution can be partly deduced from experimental data using the damage evolution equation, Eq. (12). The expression for the damage, D_f, as a function of number of cycles and loading can be obtained by integrating Eq. (12) with respect to N

$$\begin{aligned}
&\int \frac{dD_f}{dN} dN = \int B\tau_a{}^m D_f{}^\gamma dN \\
&\int \frac{1}{D_f{}^\gamma} dD_f = \int B\tau_a{}^m dN \\
&\frac{D_f{}^{1-\gamma}}{1-\gamma} = B\tau_a{}^m N + C \\
&D_f = \left[(1-\gamma)B\tau_a{}^m N + C'\right]^{\frac{1}{1-\gamma}}
\end{aligned} \tag{28}$$

where C is the integration constant and $C' = (1\text{-}\gamma)C$. The integration constant can be solved from the condition at failure, $N = N_f$, by recalling Eq. (24). In this condition the fatigue damage obtains the critical value, D_c. As a result, the constant C' becomes

$$\begin{aligned}
&1 - \frac{\tau_a}{t_0} = \left[(1-\gamma)B\tau_a{}^m N_f + C'\right]^{\frac{1}{1-\gamma}} \\
&C' = (1 - \frac{\tau_a}{t_0})^{(1-\gamma)} - (1-\gamma)B\tau_a{}^m N_f
\end{aligned} \tag{29}$$

and the expression for damage can be re-written

$$D_f = \left[(1 - \frac{\tau_a}{t^0})^{(1-\gamma)} + (1-\gamma)B\tau_a{}^m (N - N_f)\right]^{\frac{1}{1-\gamma}} = \frac{C_1}{C_2} \tag{30}$$

With the ratio of the constants C_1 and C_2 known, the other one can be simply expressed, for example, as

$$\begin{aligned}
&C_1 = \left[(1 - \frac{\tau_a}{t^0})^{(1-\gamma)} + (1-\gamma)B\tau_a{}^m (N - N_f)\right]^{\frac{1}{1-\gamma}} \times C_2 \\
&C_2 = N_f - N
\end{aligned} \tag{31}$$

If one considers three different fatigue lives, designated N_1, N_2 and N_3, so that $N_1 < N_2 < N_3$ then the crack size distributions appear as shown in Fig. 39.

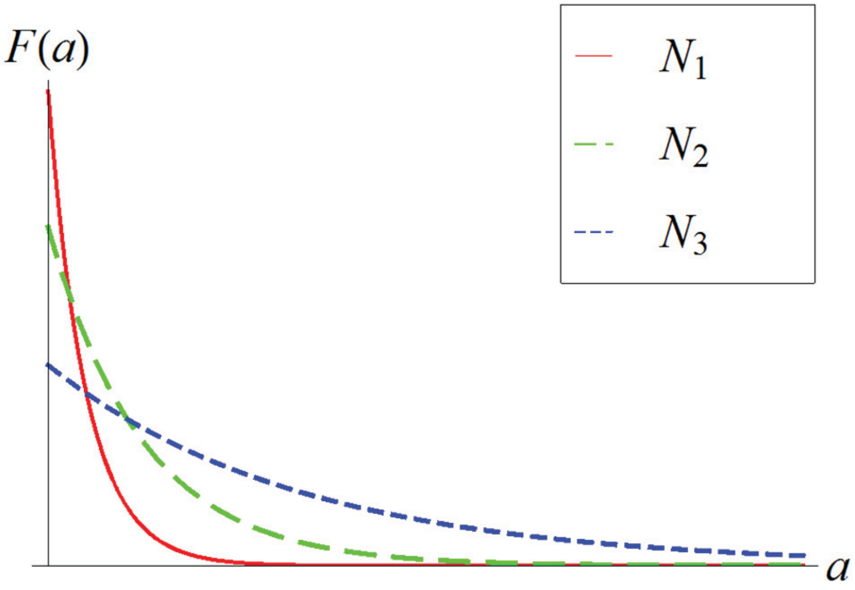

Figure 39. Evolution of the crack size distribution with number of cycles.

It should be underlined that the exponential crack distribution is merely an assumption, as there is not enough experimental evidence to obtain the accurate crack distribution. However, the SEM results confirm that the damage indeed consists of some distribution of small cracks, and the assumption of an exponential shape for their distribution is reasonable. In addition, the expression for C_2 is speculative.

4.6.6 Discussion

The proposed damage evolution law is a phenomenological model of irreversible processes in the adhesive material leading to failure during repeated loading. The total amount of damage was observed from the specimen compliance, but it does not fully describe the damage in the material. It was suggested that the true physical nature of damage is represented by a set of cracks with an exponential distribution. Some information about the distribution was derived from the measured values of compliance. However, the link between the distribution of cracks and the measured change in compliance remains partly unclear. It is known, that a single crack embedded in a material has an influence on the value of displacement at a remote point, and the influence depends not only on the crack length, but also on the distance between the crack and the remote point (see for example the case of a circular crack under mode I loading in Tada et al., 2000, p. 342). Thus, a single crack changes the compliance of a modified napkin ring specimen depending not only on the crack size but also on the distance between the crack and the boundary between adhesive and steel, i.e., the thickness of the adhesive layer. The problems with defining the thickness have been discussed earlier in this thesis. Furthermore, the influence of cracks on each other and the coalescence of cracks are topics that are still not very well established in the field of fracture mechanics. In summary, the damage variable defined from a simple change in the elastic property of the interface is not a full description of damage, but it is sufficient for practical purposes.

The results of the cyclic step tests (Section 4.3) show that the interface relative displacement has elastic and inelastic portions, especially at relatively high shear stresses. Nevertheless, the adopted progressive damage modelling approach assumes linear shear stress – relative displacement behaviour throughout the damage evolution. It is believed that the inelastic response only becomes significant at very high stresses and at the final stages of damage evolution. As a result, it is a reasonable simplification to assume the response to be linear. However, the model could be more accurate if the inelasticity was taken into account. In the literature, there are studies on CZM with inelastic constitutive behaviour defined for low-cycle fatigue assessment that can be used as reference for future research (Cao and Vormwald, 2013).

The small crack growth equation could not be determined using the specimen. Only the evolution of the overall damage given by the compliance of the specimen could be evaluated. A different experimental approach would be needed for small crack growth assessment. The small crack growth differs from long crack growth in that the small strain assumption is violated. The yielding around the crack tip encompasses a large area compared to the crack size and therefore, the small crack growth should be related to the plastic strain amplitude. As demonstrated by the cyclic step tests, the modified napkin ring specimens could theoretically provide a measure of elastic and plastic shear strain in the interface; however, the interface thickness should be extremely well controlled. In the presented experiments, there was a systematic deviation in the interface thickness due to manufacturing tolerances of the experimental setup and the specimen. In reality, it is very difficult to attain flatness within a few micrometers. In addition, the surfaces should be smooth as the contours of the surface roughness introduce high variations in the local interface thickness. Furthermore, the definition of shear strain becomes more and more ambiguous as the interface thickness approaches zero.

The progressive fatigue damage model was developed with the goal to assess the fatigue life of the engineering bonded/bolted joint. In these joints, the failure mode is a competition between progressive damage in the adhesive and fretting fatigue. It is not fully clear how the stresses in the interface of the bonded/bolted joint transfer from being carried by the adhesive to being carried by friction. A suggestion in this direction was made by introducing the progressive damage model for fatigue. The effect of the adhesive on fretting fatigue is, however, not fully understood. It should be a topic of further research to combine the progressive damage model of the adhesive with a fretting fatigue model.

Due to the shear lag effect there are tensile stresses on the adhesive interface of the bonded/bolted lapjoint. Eventually, the fatigue damage model should be formulated for mixed mode loading, in order to fully characterise the lap joint. The literature contains many studies that have assessed the mixed mode problem of the cohesive zone model with fatigue (de Moura et al, 2008; Moroni and Pirondi, 2011; Naghipour et al., 2011).

5. Conclusions

In this study, hybrid bonded/bolted joints in high-strength steel were studied under fatigue loading using experimental, analytical and numerical methods. The research provides valuable results for product development and for the design of structures involving the use of bonded/bolted joints, by increasing the understanding of failure phenomena and providing tools for fatigue analysis.

The modified napkin ring specimen was introduced for assessing the clamped and bonded interface under fatigue loading. The cohesive zone modelling technique was adopted for describing the interface de-bonding, and it was shown that the modified napkin ring specimen can be used to determine the parameters for the CZM directly, thus increasing the understanding of the physical nature of the various parameters.

A statistical method was used to study the fatigue strength of idealised bonded and clamped interfaces. The results were then used to estimate the fatigue strength of a full-scale, double lap joint by calculating the stress state at the bonded interface with FEM, and comparing the stresses to the interface fatigue strength values. The approach provided a conservative estimate of the fatigue strength of the double lap joint.

For a more detailed analysis involving an estimation of the joint fatigue life, a progressive fatigue damage model, based on the experimentally-measured change in compliance, was developed for the adhesive. The model parameters were fitted from low-cycle fatigue experimental data on the napkin ring specimen.The bonded interface subjected to fatigue damage was studied by scanning electron microscopy, and the nature of the fatigue damage was identified. It was suggested that the damage could be described by a set of microstructurally small cracks with an exponential length distribution which evolves with the number of cycles.

The most important results are summarised as in the following

1. Fatigue failure of the idealised bonded and clamped interface was studied using the modified napkin ring specimen. The failure mode was found to be shear decohesion under low clamping stress, evidenced by low relative displacement amplitudes and sudden slipping at failure. Fretting fatigue was found to be the dominant failure mode under high clamping stress. This was evidenced by high slipping amplitudes, and often a crack was found in the HSS specimen in the inspection following failure.

2. Similar failure modes were observed in the double lap joint as well. At high loading amplitudes, the specimen failed by shear decohesion as the frictional forces due to bolting could not sustain the applied load. With slightly lower loading amplitudes, severe fretting damage was found at the critical locations at the edge of the area clamped by the bolt. A notch was found at the critical location as a consequence of fretting, but no cracks had propagated in the steel specimen.
3. A more in-depth understanding of the fatigue damage process in the adhesive was obtained by an SEM study of the damaged adhesive. It was found that fatigue damage consisted of several microstructurally small cracks with different lengths and orientations. The cracks displayed a zig-zag shape and were branched due to cyclic stress. It was also observed that the fatigue cracks did not extend through the adhesive and, consequently, did not enable metal-to-metal contact between the asperities of the surface roughness.
4. Fatigue strength of the modified napkin ring specimens (under different clamping stresses, with three different surface roughnesses and in the bonded and non-bonded conditions) was estimated using the small sample staircase method. It was found that the fatigue strength of the interface under high clamping stress was the same for bonded and non-bonded interfaces. This could be explained by the failure modes under different clamping stresses.
5. The inelastic slipping response of the modified napkin ring specimens was studied by cyclic step tests. It was found that the hysteresis loop of the inelastic slipping could be described with a power-law relation. However, as the inelasticity was very small with other than extremely high loading amplitudes, further assessments were conducted assuming a linear response of the load-displacement behaviour.
6. Quasi-static results from the modified napkin ring specimens were used to determine parameters for a cohesive contact definition in the finite element method. The fundamental assumption was that the same cohesive law could describe the response of the adhesive under any clamping stress, and that the frictional tractions could be added in proportion to damage. This approach was found to reproduce the quasi-static response of the modified napkin ring specimen with good accuracy under different clamping stresses. The approach was also deemed to be convenient for use because it could employ a built-in feature of the finite element software, Abaqus.
7. The cohesive contact definition, as determined from the quasi-static response of the modified napkin ring specimens, was applied in a finite element model of the double lap joint. As a result, the stress state at the bonded interface of the joint could be solved. The stress state was compared to fatigue strength results from the modified napkin ring specimens, and a conservative estimate of the DLJ fa-

tigue strength was obtained. It was cautiously assumed that bonded areas under tensile stress do not contribute to fatigue strength.

8. For a more accurate fatigue assessment of the bonded interface, a progressive fatigue damage model was suggested. The damage was measured experimentally from the change in compliance during a low-cycle fatigue test on the modified napkin ring specimen. It was concluded, that the change in compliance does not provide a complete description of damage, but the proposed phenomenological fatigue damage model was deemed adequate for practical purposes. The proposed fatigue damage model described the experimental low-cycle fatigue lives of the modified napkin ring specimens with good accuracy.
9. The cohesive zone model, describing the fracture of the bonded interface under quasi-static loading, was re-formulated to include the effect of fatigue damage. This was accomplished by degrading the cohesive stiffness and fracture energy based on the amount of fatigue damage. The fatigue damage parameter and the quasi-static damage parameter were considered as separate, and a physical explanation for this was provided.
10. Based on the SEM results, it was suggested that the fatigue damage in the adhesive could be expressed by an exponential distribution of microstructurally small cracks. Due to fatigue loading, the distribution of cracks should evolve with the number of cycles, so that the number of small cracks decreases and the number of long cracks increases with a growing number of cycles.

References

Abaqus User Manual (2012), version 6.12.

Albrecht, P., Sahli, A.H. (1986) ‘Fatigue strength of bolted and adhesive bonded structural steel joints’. In: Potter J. M., (ed.) *Fatigue in mechanically fastened composite and metallic joints*. Philadelphia: ASTM STP 927, American Society for Testing and Materials. pp. 72-94.

Albrecht, P. (1987) ‘Fatigue strength of adhesively bonded cover plates’. *Journal of Structural Engineering*, 113:1236-1250.

Alfano, G., Sacco, E. (2006) ‘Combining interface damage and friction in a cohesive-zone model’. *International Journal for Numerical Methods in Engineering,* 68:542-582.

Allix, O., Ladevéze, P., Corigliano, A. (1995) ‘Damage analysis of interlaminar fracture specimens’. *Composite Structures,* 31:61-74.

Ashcroft, I., Mubashar, A. (2011) ‘Numerical Approach: Finite Element Analysis’. In: da Silva, L. F. M., Öchsner, A., Adams, R. D. (eds.) *Handbook of Adhesion Technology*. Berlin Heidelberg: Springer-Verlag. pp. 629-660.

ASTM Standard D 1002, 2010: *Standard Test Method for Apparent Shear Strength of Single-Lap-Joint Adhesively Bonded Metal Specimens by Tension Loading (Metal-to-Metal).* West Conshohocken, PA: ASTM International. DOI: 10.1520/D1002-10. www.astm.org.

ASTM Standard D 3166, 1999 (2005): *Standard test method for fatigue properties of adhesives in shear by tension loading (metal/metal)*. West Conshohocken, PA: ASTM International. DOI: 10.1520/D3166-99R12. www.astm.org.

ASTM Standard D 3528, 1996 (2008): *Standard Test Method for Strength Properties of Double Lap Shear Adhesive Joints by Tension Loading*. West Conshohocken, PA: ASTM International. DOI: 10.1520/D3528-96R08. www.astm.org.

ASTM Standard D 5656, 2010: *Standard Test Method for Thick-Adherend Metal Lap-Shear Joints for Determination of the Stress-Strain Behavior of Adhesives in Shear by Tension Loading*. West Conshohocken, PA: ASTM International. DOI: 10.1520/D5656-10. www.astm.org.

ASTM Standard E647, 2005: *Standard Test Method for Measurement of Fatigue Crack Growth Rates*. West Conshohocken, PA: ASTM International. DOI: 10.1520/E0647-05. www.astm.org.

Barenbaltt, G. I. (1962) 'The mathematical theory of equilibrium cracks in brittle fracture'. *Advances in Applied Mechanics,* 7:55-129.

Benhamena, A., Talha, A., Benseddiq, N., Amrouche, A., Mesmacque, G., Benguediab, M. (2010) 'Effect of clamping force on fretting fatigue behaviour of bolted assemblies: Case of couple steel–aluminium'. *Materials Science and Engineering A*, 527:6413-6421.

Bouvard, J. L., Chaboche, J. L., Feyel, F, Gallerneau, F. (2009) 'A cohesive zone model for fatigue and creep-fatigue crack growth in single crystal superalloys'. *International Journal of Fatigue,* 31:868-879.

Brownlee, K.A., Hodges, J.L., Murray Rosenblatt, Jr. (1953) 'The Up-and-down Method with Small Samples'. *Journal of the Americal Statistical Association,* 48: 262-277.

BS ISO 12107:2003 *Metallic materials. Fatigue testing. Statistical planning and analysis of data.* London, United Kingdom: British Standards Institution. ISBN: 0 580 42963 6.

Cao, X., Vormwald, M. (2013) 'Application of a new cohesive zone model in low cycle fatigue'. *Solids and Structures,* 2(3):31-40.

Castagnetti, D., Dragoni, E., Spaggiari, A. (2011) 'Failure analysis of complex bonded structures: Experimental tests and efficient finite element modeling by tied mesh method'. *International Journal of Adhesion and Adhesives,* 31:338-346.

Castagnetti, D., Dragoni, E. (2012) 'Predicting the macroscopic shear strength of adhesively-bonded friction interfaces by microscale finite element simulations'. *Computational Materials Science*, 64:146-150.

Castagnetti, D., Dragoni, E. (2013) 'Experimental assessment of a micro-mechanical model for the static strength of hybrid friction-bonded interfaces'. *The Journal of Adhesion*, 89:642-659.

Chai, H. (1993a) 'Deformation and failure of adhesive bonds under shear loading'. *Journal of Materials Science*, 28:4944-4956.

Chai, H. (1993b) 'Observation of deformation and damage at the tip of cracks in adhesive bonds loaded in shear and assessment of a criterion for fracture'. *International Journal of Fracture,* 60:311-326.

Chakherlou, T. N., Razavi, M. J., Abazadeh, B. (2013) 'Finite element investigations of bolt clamping force and friction coefficient effect on the fatigue behaviour of aluminium alloy 2024-T3 in double shear lap joint'. *Engineering Failure Analysis* 29:62-74.

Chan, W. S., Vedhagiri, S. (2001) 'Analysis of composite bonded/bolted joints used in repairing'. *Journal of Composite Materials,* 35:1045-1061.

Chandra, N., Li, H., Shet, C., Ghonem, H. (2002) ‘Some issues in the application of cohesive zone models for metal-ceramic interfaces’. *International Journal of Solids and Structures,* 39:2827-2855.

Ciavarella, M., Demelio, G. (2001) ‘A review of analytical aspects of fretting fatigue, with extension to damage parameters, and application to dovetail joints’. *International Journal of Solids and Structures* 38:1791-1811.

Collins, J.A. (1993) *Failure of Materials in Mechanical Design – Analysis, Prediction, and Prevention* (2nd edition). New York: Wiley.

Cornec, A., Scheider, I., Schwalbe, K.-H. (2003) ‘On the practical application of the cohesive model’. *Engineering Fracture Mechanics,* 70:1963-1987.

Croccolo, D., De Agostinis, M., Vincenzi, N. (2010) ‘Static and dynamic strength evaluation of interference fit and adhesively bonded cylindrical joints’. *International Journal of Adhesion & Adhesives,* 30:359-366.

da Silva, L. F. M., Öchsner, A., Adams, R.D. (eds.) (2011) *Hadbook of Adhesion Technology*. Heidelberg: Springer-Verlag. ISBN 978-3-642-01168-9.

de-Andrés, A., Pérez, J. L., Ortiz, M. (1999) ‘Elastoplastic finite element analysis of three-dimensional fatigue crack growth in aluminium shafts subjected to axial loading’. *International Journal of Solids and Structures,* 36:2231-2258.

De Bruyne, N. A. (1944) ‘The strength of glued joints’. *Aircraft Engineering,* 16:115-118.

De Bruyne, N.A. (1962) ‘The measurement of the strength of adhesive and cohesive joints’. In: *Adhesion and cohesion. Proceedings of the Symposium on Adhesion and Cohesion;* General Motors Research Laboratories, Warren, Michigan: 24-25 July 1961. Amsterdam/London/New York: Elsevier Publishing Company. pp. 47-64.

De Moura, M. F. S. F., Gonçalves, J. P. M., Chousal, J. A. G., Campilho, R. D. S. G. (2008) ‘Cohesive and continuum mixed-mode damage models applied to the simulation of the mechanical behavior of bonded joints’. *International Journal of Adhesion and Adhesives,* 28:419-426.

Del Piero, G., Raous, M. (2010) ‘A unified model for adhesive interfaces with damage, viscosity and friction’. *European Journal of Mechanics A/Solids,* 29:496-507.

Dessureault, M., Spelt, J. K. (1997) ‘Observations of fatigue crack initiation and propagation in an epoxy adhesive’. *International Journal of Adhesion and Adhesives,* 17:183-195.

Dixon, W.J., Mood, A.M. (1948) ‘A method for obtaining and analyzing sensitivity data’. *Journal of the Americal Statistical Association*, 43: 109-126.

Dixon, W.J. (1965) ‘The up-and-down method for small samples’. *Journal of the Americal Statistical Association,* 60: 967-978.

Dragoni, E. (1999) 'Effect of anaerobic threadlockers on the fatigue strength of threaded connections'. *International Journal of Materials and Product Technology,* 14;445-455.

Dragoni, E., Mauri, P. (2000) 'Intrinsic static strength of friction interfaces augmented with anaerobic adhesives'. *International Journal of Adhesion & Adhesives,* 20:315-321.

Dragoni, E., Mauri, P. (2002) 'Cumulative static strength of tightened joints bonded with anaerobic adhesives'. *Proceedings of the Institution of Mechanical Engineers,* 216:9-15.

Dragoni, E. (2003) 'Fatigue testing of taper press fits bonded with anaerobic adhesives'. *The Journal of Adhesion,* 79:729-747.

Dragoni, E., Mauri, P. (2011) 'Science of Friction-Adhesive Joints' In: da Silva, L. F. M, Pirondi, A., Öchsner, A. (eds.) *Hybrid Adhesive Joints.* Berlin-Heidelberg: Springer-Veralg. pp. 201-225.

Dugdale, D. S. (1960) 'Yielding in steel sheets containing slits'. *Journal of the Mechanics and Physics of Solids,* 8:100-104.

Fu, M., Mallick, P. K. (2001) 'Fatigue of hybrid (adhesive/bolted) joints in SRIM composites'. *International Journal of Adhesion & Adhesives,* 21:145-159.

Geubelle, P. H., Baylor, J. S. (1998). 'Impact-induced delamination of composites: a 2D simulation'. *Composites Part B,* 29:589-602.

Gonçalves, J. P. M., De Moura, M. F. S. F., de Castro, P. M. S. T. (2002) 'A three-dimensional finite element model for stress analysis of adhesive joints'. *International Journal of Adhesion and Adhesives,* 22:357-365.

Goto, M., Teshima, N., Han, S. Z., Euh, K., Yakushiji, T., Kim, S. S., Lee., J. (2013) 'High-cycle fatigue strength and small-crack growth behavior of ultrafine-grained copper with post-ECAP annealing'. *Engineering Fracture Mechanics,* 110:218-232.

Griffith, A. A. (1921) 'The phenomena of rupture and flow in solids'. *Philosophical transactions of the Royal Society*, A221:163-198.

Harper, P. W., Hallett, S. R. (2010) 'A fatigue degradation law for cohesive interface elements – Development and application to composite materials'. *International Journal of Fatigue,* 32:1774-1787.

Hart-Smith, L. J. (1985) 'Bolted-bonded composite joints'. *Journal of Aircraft,* 22:993-1000.

Hillerborg, A., Modéer, M, Petersson, P-E. (1976) 'Analysis of crack formation and crack growth in concrete by means of fracture mechanics and finite elements'. *Cement and Concrete Research,* 6:773-782.

Hobbacher, A. (2009). *IIW Recommendations for Fatigue Design of Welded Joints and Components*. New York: The Welding Research Council WRC Bulletin 520. ISBN 978-1-58145-527-4

Hurme, S., Oinonen, A., Marquis, G. (2011) 'Fatigue of bonded steel interfaces under cyclic shear loading and static normal stress'. *Engineering Fracture Mechanics,* 78: 1644-1656.

Hurme, S., Marquis, G. (2011) 'Microscopic examination of bonded and clamped high strength steel interfaces after cyclic shear loading'. *International Institute of Welding,* Paris, IIW Document XVI 913-11.

Hurme, S., Marquis, G. (2012) 'Fatigue behaviour of bonded high strength steel interfaces - The influence of clamping stress and surface roughness'. In: *Proceedings of the 11th Finnish Mechanics Days*; Finland, Oulu: 29-30 November 2012. Oulu, Finland: University of Oulu. pp. 155-160

Hurme, S., Marquis, G. (2013) 'The effect of clamping stress on the fatigue strength of bonded high-strength steel interfaces'. *Welding in the World,* 57: 285-292.

Hurme, S., Marquis, G. (2014) 'Fatigue experiments and finite element analysis of bolted/bonded double lap joints'. *Welding in the World,* DOI: 10.1007/s40194-014-0157-4 [Accepted for publication on 30th April 2014].

Hück, M. (1983) 'Ein verbessertes Verfahren für die Auswertung von Treppenstufenversuchen (An improved method for the evaluation of staircase tests)'. *Zeitschrift für Werkstofftechnik,* 14: 406-17.

Imanaka, M., Haraga, K., Nishikawa, T. (1995) 'Fatigue strength of adhesive/rivet combined lap joints', *Journal of Adhesion* 49:197–209.

ISO Standard 9664:1993. *Adhesives -- Test methods for fatigue properties of structural adhesives in tensile shear*. Geneva: Switzerland: International Organization for Standardization. www.iso.org

Kawamura, H., Sawa, T., Yoneno, M., Nakamura, T. (2003) 'Effect of fitted position on stress distribution and strength of a bonded shrink fitted joint subjected to torsion'. *International Journal of Adhesion & Adhesives,* 23:131-140.

Kelly, G. (2006) 'Quasi-static strength and fatigue life of hybrid (bonded/bolted) composite single lap joints'. *Composite Structures*, 72:119-129.

Kenane, M., Benzeggagh, M. L. (1997) 'Mixed-mode delamination fracture toughness of unidirectional glass/epoxy composites under fatigue loading'. *Composites Science and Technology,* 57:597-605.

Khoramishad, H., Crocombe, A. D., Katnam, K. B., Ashcroft, I. A. (2010) 'Predicting fatigue damage in adhesively bonded joints using a cohesive zone model'. *International Journal of Fatigue,* 32:1146-1158.

Kwakernaak, A., Hofstede, J., Poulis, J., Benedictus, R. (2010) ‘Improvements in bonding metals (steel, aluminium) ’. In: Dillard, D. A. (ed.). *Advances in structural adhesive bonding*. Cambridge: Woodhead Publishing Limited. pp. 185-236.

Landry, B., LaPlante, G. (2012) ‘Modeling delamination growth in composites under fatigue loadings of varying amplitudes’. *Composites: Part B,* 43:533-541.

Little, R.E. (1974) ‘The up-and-down method for small samples with extreme value response distributions’. *Journal of the American Statistical Association,* 69: 803-806.

Mann, J. Y., Pell, R. A., Jones, R., Heller, M. (1985) ‘Reducing the effects of rivet holes on fatigue life by adhesive bonding’. *Theoretical and Applied Fracture Mechanics,* 3:113-124.

Marquis, G. (1992) *Analysis of automated fatigue crack growth rate data*. Espoo, Finland: VTT Publications: 108. ISBN 951-38-4226-6.

MATLAB and Curve Fitting Toolbox Release 2012b, The MathWorks, Inc., Natick, Massachusetts, United States.

May, M., Hallett, S. R. (2010) ‘A combined model for initiation and propagation of damage under fatigue loading for cohesive interface elements’. *Composites: Part A,* 41:1787-1796.

May, M., Hallett, S. R. (2011) ‘An advanced model for initiation and propagation of damage under fatigue loading – part I: Model formulation’. *Composite Structures,* 93:2340-2349.

Moroni, F., Pirondi, A., Kleiner, F. (2010) ‘Experimental analysis and comparison of the strength of simple and hybrid structural joints’. *International Journal of Adhesion & Adhesives,* 30:367–379.

Moroni, F., Pirondi, A. (2011) ‘A procedure for the simulation of fatigue crack growth in adhesively bonded joints based on the cohesive zone model and different mixed-mode propagation criteria’. *Engineering Fracture Mechanics,* 78:1808-1816.

Muñoz, J. J., Galvanetto, U., Robinson, P. (2006) ‘On the numerical simulation of fatigue driven delamination with interface elements’. *International Journal of Fatigue,* 28:1136-1146.

Murakami, Y., Miller, K. J. (2005) ‘What is fatigue damage? A view point from the observation of low cycle fatigue process’. *International Journal of Fatigue,* 27:991-1005.

Naghipour, P., Bartsch, M., Voggenreiter, H. (2011) ‘Simulation and experimental validation of mixed mode delamination in multidirectional CF/PEEK laminates under fatigue loading’. *International Journal of Solids and Structures,* 48:1070-1081.

Needleman, A. (1987) 'A continuum model for void nucleation by inclusion debonding'. *Journal of Applied Mechanics,* 54:525-531.

Nesládek, M., Španiel, M., Jurenka, J., Růžička, J., Kuželka, J. (2012) 'Fretting fatigue – Experimental and numerical approaches'. *International Journal of Fatigue,* 44:61-73

Nicholas, T. (2006) *High cycle fatigue: A mechanics of materials perspective*. Oxford: Elsevier Ltd.

Nisitani, H., Goto, M., Kawagoishi, N. (1992) 'A small-crack growth law and its related phenomena'. *Engineering Fracture Mechanics,* 41:499-513.

Nowell, D., Dini, D., Hills, D. A. (2006) 'Recent developments in the understanding of fretting fatigue'. *Engineering Fracture Mechanics,* 73:207-222

Oinonen, A., Marquis, G. (2011a) 'A parametric shear damage evolution model for combined clamped and adhesively bonded interfaces'. *Engineering Fracture Mechanics,* 78: 163-174.

Oinonen, A., Marquis, G. (2011b) 'Shear decohesion of clamped abraded steel interfaces reinforced with epoxy adhesive'. *International Journal of Adhesion and Adhesives,* 31: 550-558.

Oinonen, A., Marquis, G. (2013) 'Shear damage simulation of adhesive reinforced bolted lap-connection interfaces'. *Engineering Fracture Mechanics,* 109: 341-352.

Osnes, H., McGeorge, D. (2009) 'Experimental and analytical strength analysis of double lap joints for marine applications'. *Composites: Part B* 40:29-40.

Paris, P. C., Gomez, M. P., Anderson, W. E. (1961) 'A rational analytic theory of fatigue'. *The Trend in Engineering,* 13:9-14.

Parrinello, F., Failla, B., Borino, G. (2009) 'Cohesive-frictional interface constitutive model'. *International Journal of Solids and Structures,* 46:2680-2692.

Pascoe, J. A., Alderliesten, R. C., Benedictus, R. (2013) 'Methods for the prediction of fatigue delamination growth in composites and adhesive bonds – A critical review'. *Engineering Fracture Mechanics,* 112-113:72-96.

Pearson, S. (1975) 'Initiation of fatigue cracks in commercial aluminium alloys and the subsequent propagation of very short cracks'. *Engineering Fracture Mechanics,* 7:235-247.

Pirondi, A., Moroni, F. (2010) 'A progressive damage model for the prediction of fatigue crack growth in bonded joints'. *Journal of Adhesion,* 86:501-521.

Robinson, P., Galvanetto, U., Tumino, D., Bellucci, G., Violeau, D. (2005) ‘Numerical simulation of fatigue-driven delamination using interface elements’. *International Journal for Numerical Methods in Engineering,* 63:1824-1848.

Roe, K. L., Siegmund, T. (2003) ‘An irreversible cohesive zone model for interface fatigue crack growth simulation’. *Engineering Fracture Mechanics,* 70:209-232.

Sacco, E., Lebon, F. (2012) ‘A damage-friction interface model derived from micromechanical approach’. *International Journal of Solids and Structures,* 49:3666-3680.

Sawa, T., Yoneno, M., Motegi, Y. (2001) ‘Stress analysis and strength evaluation of bonded shrink fitted joints subjected to torsional loads’. *Journal of Adhesion Science and Technology,* 15:23-42.

Sehra, I. S. (2013) *Damage evolution model for bonded and clamped interfaces under cyclic shear loading*. M.Sc. Dissertation. Espoo, Finland: Aalto University [unpublished].

Sekercioglu, T., Gulsoz, A., Rende, H. (2005) ‘The effects of bonding clearance and interference fit on the strength of adhesively bonded cylindrical components’. *Materials and Design*, 26:377-381.

Sekercioglu, T., Kovan, V. (2008) ‘Torque strength of bolted connections with locked anaerobic adhesive’. *Proceedings of the Institution of Mechanical Engineers Part L. Journal of materials: design and applications,* 222:83-89.

SFS-EN 14869-1:2011 *Structural adhesives - Determination of shear behaviour of structural bonds - Part 2: Thick adherends shear test (ISO 11003-2:2001, modified).* Helsinki, Finland: Finnish Standards Association. www.sfs.fi

Suresh, S., Ritchie, R. O. (1984) ‘Propagation of short fatigue cracks’. *International Metals Reviews,* 29:445-476.

Tada, H., Paris, P. C., Irwin, G. R. (2000) *The stress analysis of cracks handbook 3rd Edition*. Bury St. Edmunds: Professional Engineering Publishing. The American Society of Mechanical Engineers, New York. ISBN 1-86058-304-0

Tong, L., Luo, Q. (2011) ‘Analytical Approach to Joint Design’. In: da Silva, L. F. M., Öchsner, A., Adams, R. D. (eds.) *Handbook of Adhesion Technology.* Berlin Heidelberg: Springer-Verlag. pp. 597-628.

Turon, A., Camanho, P. P., Costa, J., Dávila, C. G. (2006) ‘A damage model for the simulation of delamination in advanced composites under variable-mode loading’. *Mechanics of Materials,* 38:1072-1089.

Turon, A., Costa, J., Camanho, P. P., Dávila, C. G. (2007) ‘Simulation of delamination in composites under high-cycle fatigue’. *Composites: Part A,* 38: 2270-2282.

Tsai, M. Y., Oplinger, D. W., Morton, J. (1998) 'Improved theoretical solutions for adhesive lap joints'. *International Journal of Solids and Structures,* 35:1163-1185.

Tvergaard, V., Hutchinson, J. W. (1992) 'The relation between crack growth resistance and fracture process parameters in elastic-plastic solids'. *Journal of the Mechanics and Physics of Solids,* 40:1377-1397.

Ural, A., Krishnan, V. R., Papoulia, K. (2009) 'A cohesive zone model for fatigue crack growth allowing for crack retardation'. *International Journal of Solids and Structures,* 46:2453-2462.

Volkersen, O. (1938) 'The rivet load distribution in tensile loaded riveted joints with constant lap cross sections (Die Nietkraftverteilung in zugbeanspruchten Nietverbindungen mit konstanten Laschenquerschnitten) '. *Luftfahrtforschung*, 15:41-47.

Wagle, S., Kato, H. (2009) 'Ultrasonic detection of fretting fatigue damage at bolt joints of aluminium alloy plates', *International Journal of Fatigue* 31:1378-85.

Weitzenböck, J. R., McGeorge, D. (2011) 'Science and Technology in Bolt-Adhesive Joints' In: da Silva, L. F. M, Pirondi, A., Öchsner, A. (eds.) *Hybrid Adhesive Joints*. Berlin-Heidelberg: Springer-Veralg. pp. 177-199.

Xu, X. P., Needleman, A. (1993) 'Void nucleation by inclusion debonding in a crystal matrix'. *Modelling and Simulation in Materials Science and Engineering,* 1:111-132.

Xu, Y., Yuan, H. (2009) 'On damage accumulations in the cyclic cohesive zone model for XFEM analysis of mixed-mode fatigue crack growth'. *Computational Materials Science,* 46:579-585.

Yamaguchi, Y., Amano, S. (1985) 'Mechanical behavior of a combined joint composed of mechanical fastening and adhesive joining'. *International Journal of Adhesion & Adhesives*, 5:193-199.

Yang, B., Mall, S., Ravi-Chandar, K. (2001) 'A cohesive zone model for fatigue crack growth in quasibrittle materials'. *International Journal of Solids and Structures,* 38:3927-3944.

Yoneno, M., Sawa, T., Shimotakahara, K., Motegi, Y. (1997) 'Axisymmetric stress analysis and strength of bonded shrink-fitted joints of solid shaft subjected to push-off forces'. *JSME International Journal Series A Solid Mechanics and Material Engineering,* 40:362-374.

Yoneno, M., Sawa, T., Motegi, Y. (1998) 'Axisymmetric stress analysis and strength of bonded shrink-fitted joints of solid shaft subjected to torsional loads'. *JSME International Journal Series A Solid Mechanics and Material Engineering,* 41:517-524.

3M United Kingdom PLC (2009) *Scotch-Weld™ EPX™ Epoxy Adhesive DP760 product data sheet*.

Appendix A – High cycle fatigue test results

Table A1. Results of the constant amplitude fatigue tests for grit-blasted, bonded and non-bonded specimens. The static normal pre-stress, q; shear stress amplitude, τ_a; failure type (SD: Shear decohesion; FF: Fretting fatigue; FW: Progressive slipping due to fretting wear); cycles to failure, N_f; and relative displacement amplitude, δ_a; at $N = 2\text{x}10^5$ and $N = 1\text{x}10^6$ cycles, are listed for each specimen.

Grit-blasted, bonded specimens

Spec. no.	q [MPa]	τ_a [MPa]	Failure type, N_f	δ_a [µm] at N=2x10^5	δ_a [µm] at N=1x10^6
g4_1	4	27	SD, N_f = 1000	-	-
g4_4	4	24	SD, N_f = 70,000	-	-
g4_5	4	23	SD, N_f = 250,000	11	-
g4_6	4	21	Run-out	14	12
g50_1	50	26	SD, N_f = 2000	-	-
g50_2	50	21	SD, N_f = 7000	-	-
g50_4	50	18	Run-out	9	14
g50_7	50	13	Run-out	5	7
g50_8	50	17	Run-out	7	10
g100_1	100	32	SD, N_f = 2000	-	-
g100_2	100	39	FF, N_f = 600,000	76	-
g100_3	100	30	Run-out	35	32
g100_4	100	33	FF, N_f = 1,450,000	56	107
g100_5	100	20	Run-out	7	7
g100_6	100	33	Run-out	14	19
g100_7	100	40	SD, N_f = 1690	-	-
g150_1	150	50	Run-out	20	21
g150_2	150	56	Run-out	27	30
g150_3	150	60	Run-out	51	45
g150_4	150	67	Run-out	44	54
g150_5	150	69	FF, N_f = 1,600,000	53	53
g150_6	150	74	FF, N_f = 1,100,000	52	75
g150_7	150	58	Run-out	23	21

Grit-blasted. non-bonded specimens

Spec. no.	q [MPa]	τ_a [MPa]	Failure type, N_f	δ_a [µm] at N=2x10^5	δ_a [µm] at N=1x10^6
g50_1_nb	50	11	Run-out	60	61
g50_3_nb	50	12	Run-out	58	61
g50_4_nb	50	16	FW, N_f = 440,000	178	-
g50_5_nb	50	12	Run-out	33	38
g100_1_nb	100	31	Run-out	23	19
g100_2_nb	100	37	FF, N_f = 1,300,000	51	104
g100_3_nb	100	36	Run-out	37	30
g100_4_nb	100	38	FW, N_f = 70,000	-	-
g100_5_nb	100	33	Run-out	30	30

g150_1_nb	150	54	Run-out	26	31
g150_2_nb	150	63	Run-out	39	33
g150_3_nb	150	65	FF, N_f = 830,000	68	-
g150_4_nb	150	65	Run-out	43	49
g150_5_nb	150	51	Run-out	25	26
g150_6_nb	150	58	Run-out	31	29

Table A2. Results of the constant amplitude fatigue tests for fine-ground, bonded and non-bonded specimens. The static normal pre-stress, q; shear stress amplitude, τ_a; failure type (SD: Shear decohesion; FF: Fretting fatigue; FW: Progressive slipping due to fretting wear); cycles to failure, N_f; and relative displacement amplitude, δ_a; at 2x10^5 and 1x10^6 cycles, are listed for each specimen.

Fine-ground, bonded specimens					
Spec. no.	q [MPa]	τ_a [MPa]	Failure type, N_f	δ_a [μm] at N=2x10^5	δ_a [μm] at N=1x10^6
f50_1	50	16	Run-out	43	50
f50_2	50	20	SD, N_f = 6,000	-	-
f50_3	50	15	SD, N_f = 15,000	-	-
f100_6	100	39	SD, N_f = 620	-	-
f100_7	100	51	Run-out	49	44
f100_8	100	55	Run-out	42	39
f100_9	100	58	FF, N_f = 543,000	113	-
f100_11	100	46	SD, N_f = 7600	-	-
f100_12	100	51	Run-out	58	49
f100_13	100	56	FF, N_f = 630,000	112	-
f150_1	150	55	SD, N_f = 4000	-	-
f150_2	150	56	Run-out	43	40
f150_3	150	51	SD, N_f = 2780	-	-
Fine-ground, non-bonded specimens					
Spec. no.	q [MPa]	τ_a [MPa]	Failure type, N_f	δ_a [μm] at N=2x10^5	δ_a [μm] at N=1x10^6
f50_1_nb	50	14	Run-out	73	67
f50_2_nb	50	19	FW, N_f = 160,000	-	-
f50_3_nb	50	14	FW, N_f = 100,000	-	-
f100_1_nb	100	25	Run-out	18	19
f100_2_nb	100	35	Run-out	39	58
f100_3_nb	100	40	Run-out	35	33
f100_4_nb	100	43	FF, N_f = 618,000	94	-
f150_1_nb	150	33	Run-out	20	19
f150_2_nb	150	39	Run-out	20	22
f150_3_nb	150	60	Run-out	51	49
f150_4_nb	150	64	Run-out	52	67
f150_5_nb	150	68	FF, N_f = 1,200,000	65	118
f150_6_nb	150	65	Run-out	40	39

Table A3. Results of the constant amplitude fatigue tests for coarse-ground, bonded and non-bonded specimens. The static normal pre-stress, q; shear stress amplitude, τ_a, failure type (SD: Shear decohesion; FF: Fretting fatigue; FW: Progressive slipping due to fretting wear); cycles to failure, N_f; and relative displacement amplitude, δ_a; at 2x10^5 and 1x10^6 cycles, are listed for each specimen.

Coarse-ground, bonded specimens

Spec. no.	q [MPa]	τ_a [MPa]	Failure type, N_f	δ_a [μm] at N=2x10^5	δ_a [μm] at N=1x10^6
c50_1	50	15	Run-out	10	23
c50_2	50	20	FW, N_f = 211,100	144	-
c100_1	100	22	Run-out	10	12
c100_2	100	25	Run-out	14	14
c100_3	100	30	Run-out	24	21
c100_4	100	35	Run-out	28	36
c100_5	100	40	FF, N_f = 610,000	97	-
c100_6	100	35	Run-out	33	29
c100_7	100	40	FF, N_f = 1,930,000	47	80
c150_1	150	58	SD, N_f = 1,420	-	-
c150_2	150	55	Run-out	27	31
c150_3	150	61	Run-out	36	32
c150_4	150	61	Run-out	41	43

Coarse-ground, non-bonded specimens

Spec. no.	q [MPa]	τ_a [MPa]	Failure type, N_f	δ_a [μm] at N=2x10^5	δ_a [μm] at N=1x10^6
f100_1_nb	100	30	Run-out	32	32
f100_2_nb	100	35	FF, N_f = 1,691,000	65	92
f100_3_nb	100	30	Run-out	24	21
f100_4_nb	100	35	FF, N_f = 1,110,000	72	149
f150_1_nb	150	38	Run-out	25	17
f150_2_nb	150	57	Run-out	44	46
f150_3_nb	150	62	FF, N_f = 880,000	53	-
f150_4_nb	150	57	Run-out	41	42

Appendix B – SEM photographs

Specimen in the initial state (before cyclic loading)

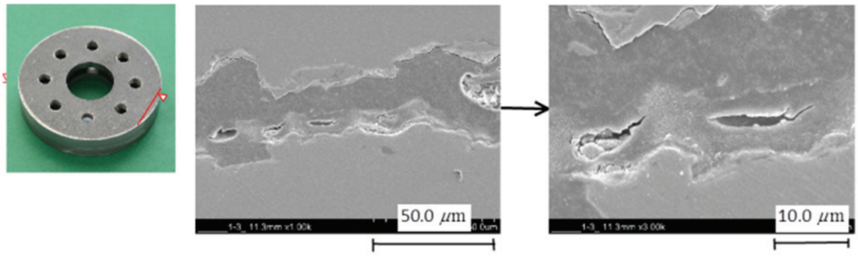

Figure B.1. Specimen in the initial state, tangential cut 1.

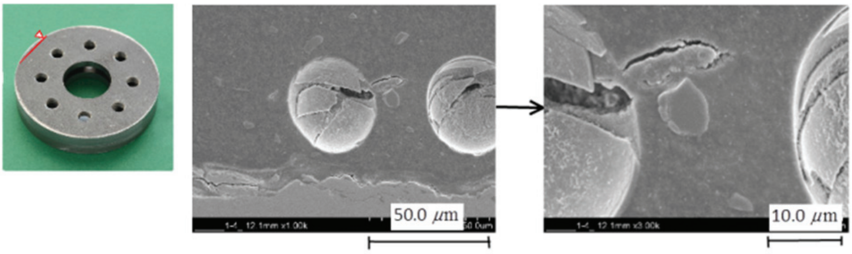

Figure B.2. Specimen in the initial state, tangential cut 2.

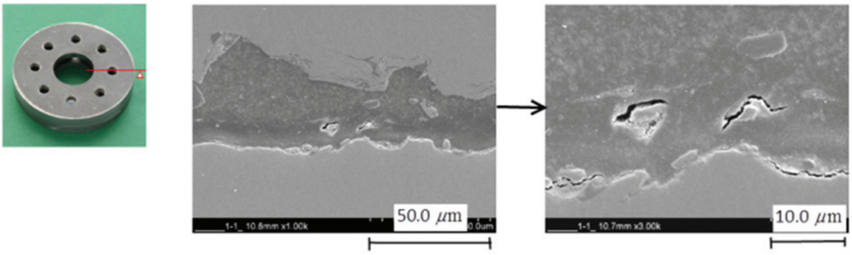

Figure B.3. Specimen in the initial state, radial cut 1.

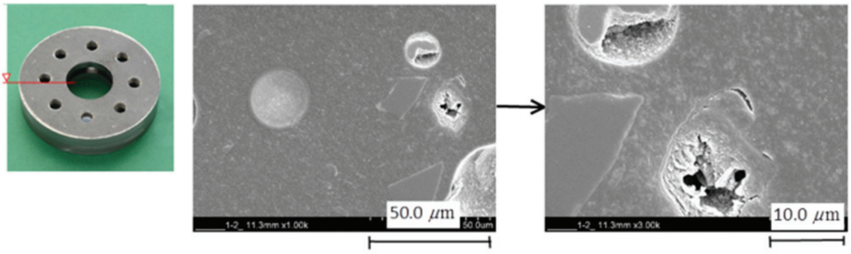

Figure B.4. Specimen in the initial state, radial cut 2.

Specimen I4

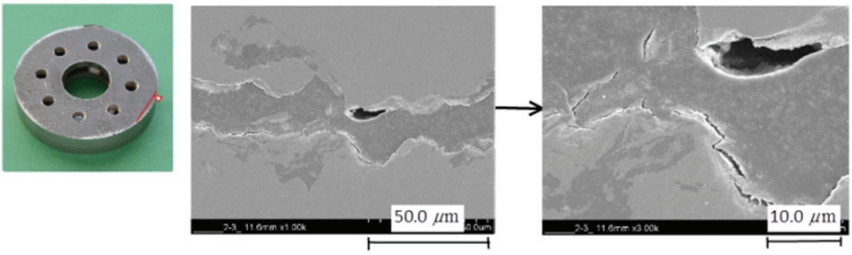

Figure B.5. Specimen I4, tangential cut 1.

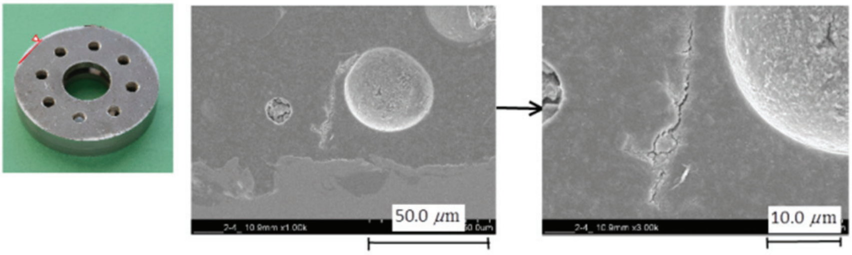

Figure B.6. Specimen I4, tangential cut 2.

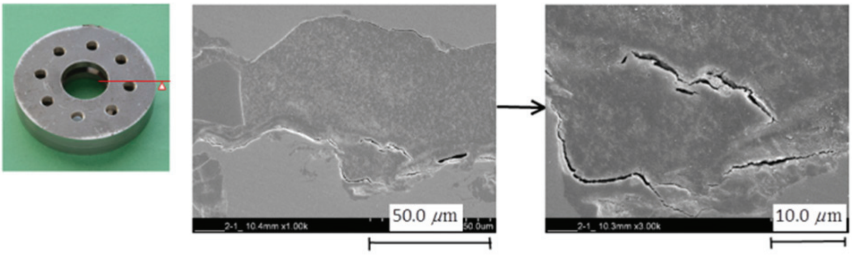

Figure B.7. Specimen I4, radial cut 1.

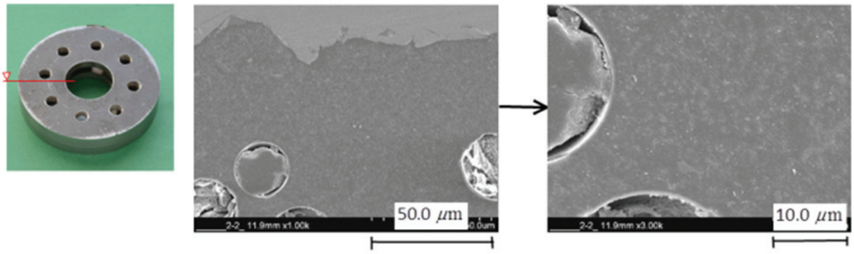

Figure B.8. Specimen I4, radial cut 2.

Specimen I5

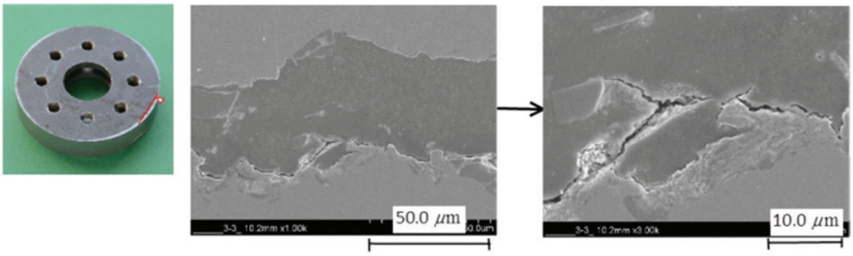

Figure B.9. Specimen I5, tangential cut 1.

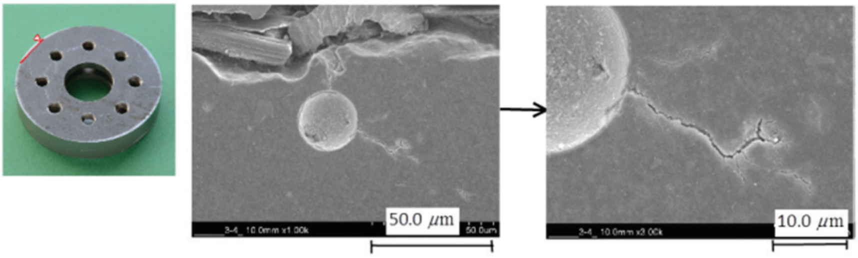

Figure B.10. Specimen I5, tangential cut 2.

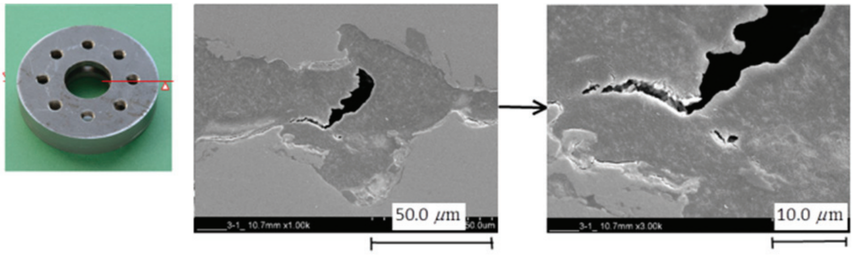

Figure B.11. Specimen I5, radial cut 1.

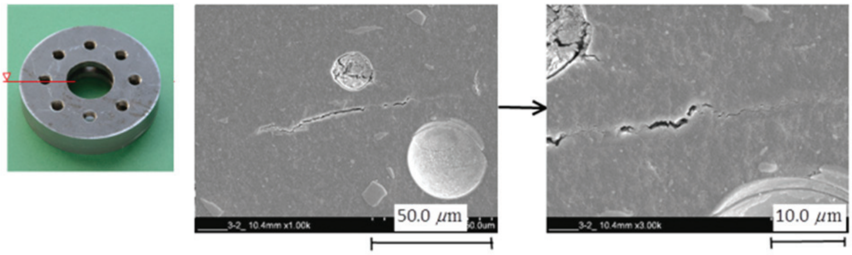

Figure B.12. Specimen I5, radial cut 2.

Appendix C – Cyclic step test data fitting and measurement precision

The fitting of the cyclic step test data with Eq. (8)

$$\frac{\Delta\delta}{\delta^0}=\frac{\Delta\tau}{A_1}+\left(\frac{\Delta\tau}{A_2}\right)^{A_3}$$

is explained. The measurement device records the applied force [kN] and the displacement at the eddy current sensor [mm]. The shear stress, τ, and relative displacement, δ, at the specimen interface are calculated from the force-displacement data. The applied force data have some scatter. The force is applied with a sinusoidal signal and, as such, an estimate of the true value can be obtained by fitting the force data with a Fourier series. The MATLAB Curve Fitting Toolbox (MATLAB and Curve Fitting Toolbox Release 2012b) is used for the fitting. The force signal and the fit are presented in Fig. C.1.

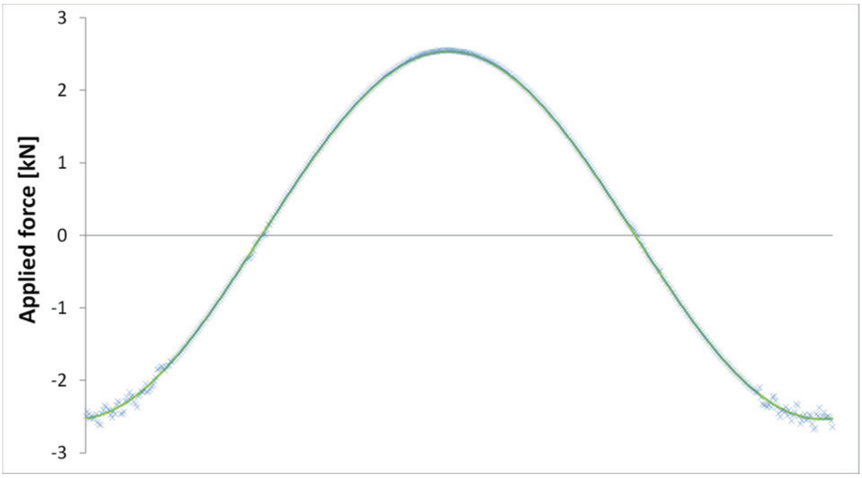

Figure C.1. Applied force and Fourier series fit.

The cyclic step tests contain four loading cycles per loading amplitude. The relative displacement data from three cycles are used for the fitting of the displacement. Half-cycle relative displacement data, normalised with the critical relative displacement, δ^0, from three loading cycles is shown in Fig. C.2. The relative displacement clearly demonstrates an elastic and an inelastic part. The unloading part can be assumed to be fully elastic, so the elastic fit is performed at that section. The elastic fit provides the constant, A_1, in Eq. (8). The elastic fit is shown in Fig. C.2 with the normalised relative displacement data.

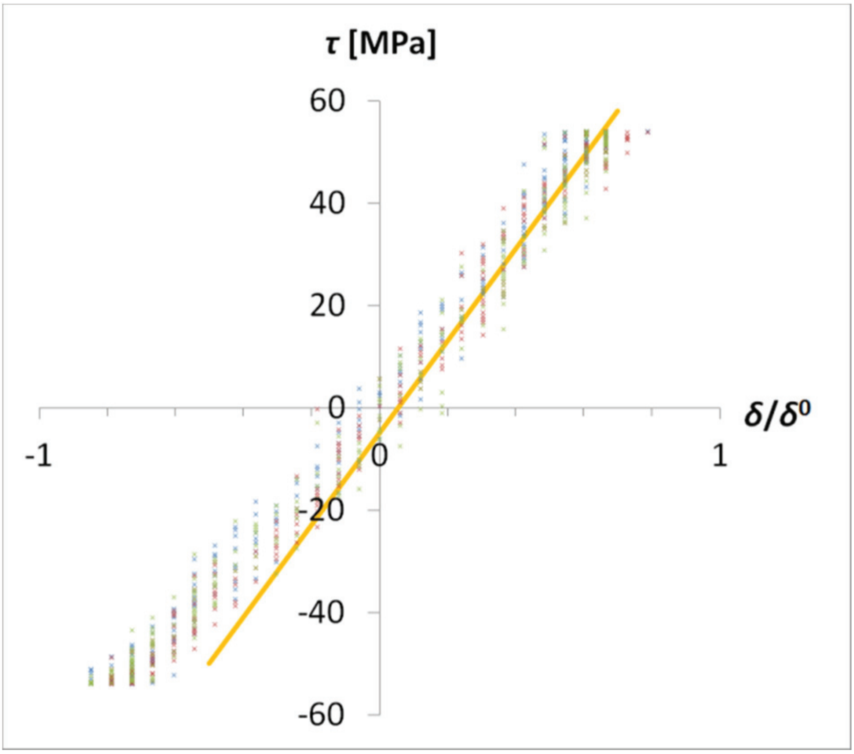

Figure C.2. Normalised relative displacement data from three load cycles. The data from only half of the cycle are shown. The elastic relative displacement is fitted to the data in the unloading part.

The inelastic portion of the relative displacement is obtained for each data point by subtracting the elastic displacement. The inelastic relative displacement data are presented in Fig. C.3. The data are fitted with the second portion of Eq. (8), giving the constants, A_2 and A_3. The inelastic fit is shown in Fig. C.3.

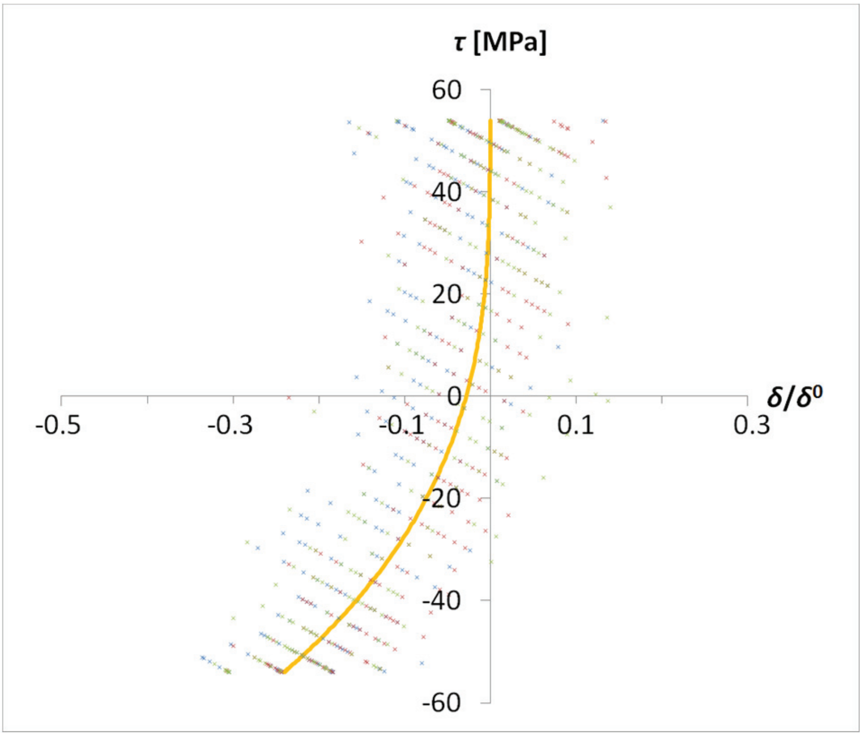

Figure C.3. Relative displacement data with the elastic portion reduced. The inelastic part of Eq. (8) is fitted to the data.

The relative displacement is calculated for each shear stress point (from the Fourier fit), which gives the hysteresis loops of Figs. 24-26. The relative displacement, δ, can be obtained by multiplying with the critical relative displacement. The fitted hysteresis loop and original hysteresis data are shown in Fig. C.4.

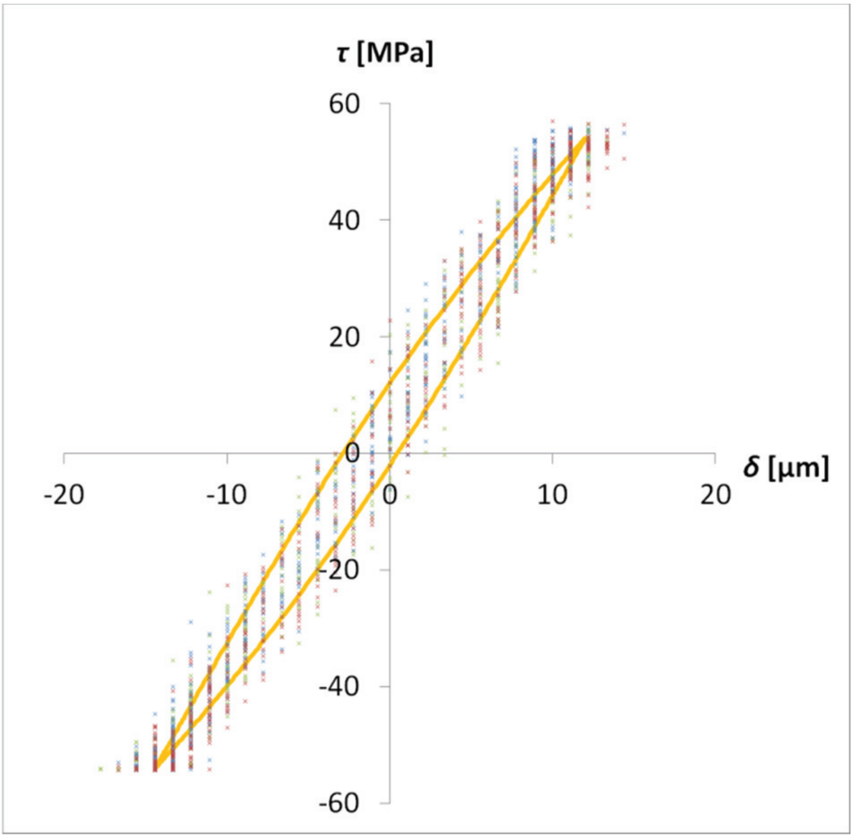

Figure C.4. Original hysteresis data and fitted model.

As can be seen in Fig. C.4, the scatter in the relative displacement data is large, compared to the measured displacements. An estimate of the measurement precision can be obtained by calculating the standard deviation

$$S = \sqrt{\frac{\sum_{i=1}^{n} \left(x_i - \bar{x} \right)^2}{n}} \qquad \text{(C.1)}$$

where the mean $\bar{x}$ is considered to be the fitted value, x_i are the measured values and n is the number of observations. The average standard deviation is found to be S = 2.4 µm.

Appendix D – Data compression

The analysis of experimental $D_f - N$ data in this paper is based on an automated data analysis methodology for crack growth rate data (Marquis, 1992). The report is not widely available and, for this reason, the methodology is explained in detail here. The report also contains a verification example which will not be discussed here.

Measurement precision

When measurement precision is not known, it can be estimated from the experimental data of one test using the equation

$$\hat{s} = \sqrt{\frac{\sum_{i=1}^{n-1} \left(x_{i+1} - x_i \right)^2}{2(n-2)}} \tag{D.1}$$

where x_i are measured data points and *n* is the total number of data points. If the measured value, x_i, is considered to be the sum of the true crack length, a_i, and measurement error, ε_i, the equation can be rewritten as

$$\hat{s} = \sqrt{\frac{\sum_{i=1}^{n-1} \left[(a + da + \varepsilon_{i+1}) - (a + \varepsilon_i) \right]^2}{2(n-2)}} \tag{D.2}$$

where da is the increment of crack extension between the measurements, *i* and *i*+1. If the crack extension is much smaller than the measurement error, $da << \varepsilon_i$, the equation becomes

$$\hat{s} \approx \sqrt{\frac{\sum_{i=1}^{n-1} \left(\varepsilon_{i+1} - \varepsilon_i \right)^2}{2(n-2)}} \tag{D.3}$$

which can be expanded

$$\hat{s} \approx \sqrt{\frac{\sum_{i=1}^{n-1} {\varepsilon_{i+1}}^2 + \sum_{i=1}^{n-1} \varepsilon_i^2 + \sum_{i=1}^{n-1} 2\varepsilon_{i+1}\varepsilon_i}{2(n-2)}} \tag{D.4}$$

If the errors are random and equally distributed around zero, the product, $\varepsilon_{i+1}\varepsilon_i$, has an equal probability of being either positive or negative. When compared to the other two summations, the summation of the terms, $\varepsilon_{i+1}\varepsilon_i$, will be small and the equation can be written as

$$\hat{s} \approx \sqrt{\frac{\sum_{i=1}^{n-1} {\varepsilon_{i+1}}^2 + \sum_{i=1}^{n-1} \varepsilon_i^2}{2(n-2)}} \qquad \text{(D.5)}$$

If the number of measurement points is large, $\sum_{i=1}^{n-1} {\varepsilon_{i+1}}^2 \approx \sum_{i=1}^{n-1} \varepsilon_i^2$, then the equation can be written as

$$\hat{s} \approx \sqrt{\frac{2\sum_{i=1}^{n} \varepsilon_i^2}{2(n-2)}} \qquad \text{(D.6)}$$

or

$$\hat{s} \approx \sqrt{\frac{\sum_{i=1}^{n} \varepsilon_i^2}{(n-2)}} \qquad \text{(D.7)}$$

The measurement precision, given as the standard deviation of the mean determined from a set of replicate measurements, is expressed by

$$s = \sqrt{\frac{\sum_{i=1}^{n} \varepsilon_i^2}{(n-1)}} \qquad \text{(D.8)}$$

where ε_i is the difference between the measured crack length, x_i, and the mean, determined from a large number of measurements. Thus, Eq. (D.1) is a good approximation of the measurement precision, as long as the following assumptions hold: 1) the errors are evenly distributed around zero, 2) the measurement precision is much greater than the crack growth between two successive measurements, and 3) the total number of measurements is large.

Data compression

Data compression is the operation whereby a large number of crack length measurements, x_i, are compressed into a single estimate, $\hat{x}_i$, of the true crack length, a_i. A first-order polynomial is fit to a set of $x_i - N$ data pairs, and $\hat{x}_i$ is obtained by evaluating the polynomial at mean cycle count.

The number of observations to be combined, n_x, depends on the measurement precision and the mean crack growth between crack length measurements, $\overline{dx}$. The spacing, $\Delta\hat{a} = 10S$, required by the ASTM E647-05 (ASTM E647, 2005) will be obtained when

$$n_x = \frac{10\hat{S}}{\overline{dx}} \tag{D.9}$$

According to the principle of the sampling distribution of means, the measurement precision is improved because of data compression by

$$S_{\bar{x}} = \frac{S^2}{n_x} \tag{D.10}$$

Using the improved precision, the number of observations to be combined becomes

$$n_x = \frac{10S_{\bar{x}}}{\overline{dx}} \tag{D.11}$$

The average crack growth between x_i measurements, $\overline{dx}$, varies easily by a few decades during a test. Accordingly, the number of crack length measurements, n_x, is not necessarily constant for analysis of the data from a test, but varies according to $\overline{dx}$. The above condition is always checked when data are compressed.

The use of novel high-performance ultra-high-strength steels enables weight savings and increased performance of structures. The design of structures with the highest potential for weight savings and performance improvements is frequently limited by the risk of fatigue failure. Hybrid joints, wherein the good properties of adhesives and mechanical fasteners or spot welds are combined, provide potential joining alternatives for improved fatigue resistance in high-strength steel structures but, thus far, adequate research data has not been available. A procedure, linking the interface characterisation and the stress analysis of the full-scale joint, is presented in this thesis. The procedure can be readily adopted for product development involving the bonded/bolted hybrid joint. Further understanding of the physical processes of failure in the bonded and clamped interface is obtained by a scanning electron microscopy study of the adhesive layer at different stages of fatigue life.

Aalto-DD 136/2014

ISBN 978-952-60-5850-4
ISBN 978-952-60-5851-1 (pdf)
ISSN-L 1799-4934
ISSN 1799-4934
ISSN 1799-4942 (pdf)

Aalto University

Department of Applied Mechanics
www.aalto.fi

BUSINESS +
ECONOMY

ART +
DESIGN +
ARCHITECTURE

SCIENCE +
TECHNOLOGY

CROSSOVER

DOCTORAL
DISSERTATIONS